POLITECNICO DI MILANO
School of Industrial and Information Engineering
Department of Aerospace Science and Technology (DAER)
Master of Science in Aeronautical Engineering

An investigation on the secondary stability of the Blasius boundary-layer

MSc Thesis of:
Giampaolo Calamia
Registration number 918430

Supervisor: Prof. Franco Auteri

Academic Year 2021-2022

A mio padre...

Abstract

The physical mechanism which drives a laminar flow to the turbulent regime is extremely complex and not yet completely understood. Considering the aeronautical field, the transition of the boundary-layer has a remarkable influence on the aerodynamic performance of airfoils and lifting surfaces in general. The present work deals with the secondary stability analysis of the Blasius boundary-layer flow, introducing, with respect to the original secondary stability theory proposed by Herbert, the non-parallel and non-linear effects. Mathematically, the problem consists in studying the stability of the Blasius flow forced by a time-periodic Tollmien–Schlichting wave by means of the Floquet theory. An incremental pressure-correction scheme based on the direction-splitting technique is used to integrate the Navier-Stokes equations whereas, for the computation of the three-dimensional secondary modes and the correspondent Floquet multipliers, the implicitly restarted Arnoldi method (IRAM), implemented in the software package ARPACK, is employed. The eigenvalue spectrum is evaluated for three reduced frequencies of the T-S wave, giving particular attention to the influence that the maximum amplitude reached by the primary wave has on the instability behaviour. It is found that the synchronous modes are associated to the largest growth rates among the whole range of spanwise wavenumbers. The subharmonic mode is the most unstable for low and medium amplitudes of the T-S wave while, as the amplitude increases, the fundamental mode, with the same period of the primary wave, becomes the most unstable. For high amplitudes the instability affects a wide range of spanwise wavenumbers and the whole frequency range from the subharmonic to the fundamental one. The results show high qualitative agreement with those provided by Herbert's formulation and it is found that, due to the inclusion of the non-linear and non-parallel effects in the base flow, the threshold amplitude for the instability is close to that observed in the experiments. A series of DNS simulations is performed to investigate if the computed three-dimensional perturbations lead the Blasius flow to the turbulent regime. The transition simulations show that, after an initial linear stage in which the disturbance evolution is close to what predicted by the stability calculations, the nonlinearity leads to the formation of Λ vortices that drive the boundary-layer flow to transition. The arrangement of these Λ structures is either aligned in rows of staggered, depending on which secondary mode is introduced in the boundary-layer flow. The two observed arrangements of the flow structures correspond to the well known H-type and K-type regimes dominated by the subharmonic or the fundamental mode, respectively. Therefore, the eigenfunctions of the secondary stability eigenvalue problem provide the near-wall vorticity perturbations responsible for the commonly observed natural transition scenarios.

Sommario

Il meccanismo fisico che provoca il passaggio dal regime laminare a quello turbolento è molto complesso e non ancora compreso appieno. In ambito aeronautico, la transizione dello strato limite ha un'influenza considerevole sulle prestazioni aerodinamiche dei profili alari e delle superfici portanti in generale. Il presente lavoro si occupa della stabilità secondaria del flusso di strato limite di Blasius, introducendo, rispetto alla formulazione originaria della stabilità secondaria introdotta da Herbert, gli effetti di non parallelismo e quelli non lineari. Matematicamente, il problema consiste nello studio della stabilità del flusso di Blasius forzato da un'onda di Tollmien–Schlichting periodica nel tempo che può essere eseguito tramite la teoria di Floquet. Le equazioni di Navier-Stokes sono integrate tramite uno schema di correzione della pressione basato sulla tecnica del direction-splitting mentre per il calcolo dei modi secondari tridimensionali e dei corrispondenti moltiplicatori di Floquet, viene utilizzato il metodo IRAM implementato nel software ARPACK. Lo spettro degli autovalori è valutato per tre valori di frequenza ridotta dell'onda T-S, con particolare riguardo all'influenza che ha l'ampiezza dell'onda primaria sulle caratteristiche dell'instabilità. Si trova che i modi sincroni sono associati ai maggiori tassi di crescita considerando tutto l'intervallo di numeri d'onda nella direzione trasversale. Il modo subarmonico è il più instabile per valori bassi o medi dell'ampiezza dell'onda T-S. Invece, quando si considera un'ampiezza elevata, è il modo fondamentale, con lo stesso periodo temporale dell'onda, ad essere il più instabile. Per alti valori di ampiezza, l'instabilità coinvolge un vasto intervallo di numeri d'onda trasversali e l'intervallo di frequenze che va da quella subarmonica a quella fondamentale. I risultati mostrano un ottimo accordo qualitativo con quelli ottenuti tramite la teoria originale di Herbert anche se l'aggiunta degli effetti di non parallelismo e di non linearità nel flusso base, porta la soglia di ampiezza al quale l'instabilità si sviluppa molto vicino ai dati sperimentali. Viene eseguita una serie di simulazioni DNS per valutare se le perturbazioni tridimensionali calcolate portano il flusso di Blasius al regime turbolento. Le simulazioni numeriche mostrano che, dopo una iniziale fase lineare in cui l'evoluzione dei disturbi è prossima a quanto previsto dai calcoli di stabilità, la non linearità porta alla formazione di vortici Λ che provocano il passaggio al regime turbolento del flusso di strato limite. La disposizione di queste strutture Λ è allineata in file o sfalsata, a seconda di quale modo secondario viene introdotto nel flusso dello strato limite di Blasius. Le due disposizioni di queste strutture corrispondono ai ben noti regimi di tipo H e di tipo K dominati rispettivamente dal modo subarmonico o dal modo fondamentale. Pertanto, le autofunzioni del problema agli autovalori della stabilità secondaria forniscono le perturbazioni

di vorticità vicino alla parete responsabili degli scenari di transizione naturale comunemente osservati nelle applicazioni pratiche.

Ringraziamenti

Vorrei dedicare qualche riga a tutti coloro che mi hanno sostenuto ed accompagnato durante il mio percorso universitario.
I primi ringraziamenti vanno al Prof. Auteri che non solo ha reso possibile la realizzazione di questo lavoro, ma mi ha trasmesso la passione e l'entusiasmo necessari affinchè la tesi prendesse forma giorno dopo giorno. La ringrazio per avermi fornito il materiale necessario e per avermi aiutato nei momenti di difficoltà.
Un ringraziamento speciale a mia mamma, che mi ha sempre sostenuto in tutte le mie scelte e non mi ha mai fatto mancare nulla in tutti questi anni.
Grazie a tutta la mia famiglia che ha sempre creduto in me e a mio nonno, a cui dedico questo traguardo raggiunto.
Grazie a te Sonja, che mi sei stata sempre accanto e mi hai compreso nei momenti di difficoltà.
Grazie a tutti quelli che mi hanno tenuto compagnia nelle giornate passate in università. Luca, Ale e Caccia, da voi ho imparato tanto.
Grazie ai tutti i miei amici che mi hanno reso la persona che sono.
Grazie a tutti i membri del gruppo "Uncinné picco glicemico", Cudia, Laudicina, Fausto, Guido, Giulio, Gaspare e tutti gli altri, per il tempo trascorso insieme e per tutto quello che verrà.
Grazie alle mie amiche storiche: Giorgia, Eugenia e Adriana.

Contents

List of Figures

List of Tables

Chapter 1

Introduction

The transition from a laminar to a turbulent regime has been a fundamental topic of scientific investigation for the past two centuries. The capability to predict the conditions under which a particular flow becomes turbulent or even to control the transition process has always been strongly desired for a wide variety of technological applications. The boundary layer laminar-turbulent transition influences the aerodynamic performances of immersed bodies and the transition behaviour also determines the wall shear stress and the heat transfer. The laminar boundary-layer thickness grows slowly with respect to the turbulent one and leads to a lower skin-friction coefficient but on the other hand the mixing properties of the turbulent regime are required to counter aerodynamic stall and separation phenomena. Maintaining the laminar regime as much as possible can reduce drag but flow separation should be avoided due to a lost of lift and an increase of pressure drag, these considerations made the transition location a central topic in airfoil analysis and more in general aerodynamic surfaces projects. The techniques to control the boundary-layer regime require a deep knowledge of the physics involved. For this reason, over the past two centuries, plenty of data have been collected from experiments on flat plates and mathematical models have been developed to understand and predict the transition process and its different stages of development. Usually, the route to turbulence is divided in three different stages: receptivity, linear stage and nonlinear breakdown (see [34]). The term receptivity coined by Morkovin([48]) concerns the physical mechanism through which external disturbances such as acoustic waves, turbulent oscillations and surface roughness are ingested by the boundary layer and projected into the correspondent eigenmodes. In recent years, many discoveries concerned this field ([46]) and now the receptivity theory is used in practice to compute disturbance spectrum and initial amplitudes

to use in linear or nonlinear evolution models. The linear stage concerns the very first phase when disturbances have settled inside the boundary layer, their evolution can be predicted using linear models until their intensity is such that the linearity hypothesis falls and a more complex model which accounts for nonlinear effects has to be used in order to describe the final stage of breakdown. However, transition is an extremely complex phenomenon and its behaviour depends on the flow considered and on the intensity of external disturbances so this classification is not rigorous. When considering turbomachinery applications, in which the disturbance intensity is typically high the fist stages described by the linear theory are bypassed [48]. Transition at high free-stream turbulent-intensity levels, called bypass transition, exhibits features that are completely different from transition in a quiet environments, called natural transition. Engineering applications involving moving vehicles in air or water are characterized by low disturbance intensity, in these cases all the stages mentioned are present and the transition process can be seen as a series of reproducible events. This research focuses on the natural transition that received particular attention from the scientific community due to implications it can have in the aeronautical field and, in particular, on the model problem of natural transition of an incompressible boundary layer over a flat plate that provides the best experimental setup to investigate transition mechanisms in detail.

1.1 Historical review

The first notable experiment regarding laminar-turbulent transition belongs to Osborne Reynolds who investigated the transition of a pipe flow using colored filaments added to the flow and observed that the character of the flow depends on a non-dimensional coefficient nowadays known as Reynolds number. All subsequent studies started from Reynolds idea that the laminar flow, which always represent a possible solution of the Navier-Stokes equations can became unstable above a certain Reynolds number ([57]). This threshold, the critical Reynolds number, represented a target for many mathematicians including Reynolds itself and led to the birth of linear stability theory which is used nowadays for transition prediction in engineering calculations. The basic idea of the theory was to consider the evolution of infinitesimal disturbances (in the linear framework) superimposed to the laminar flow, if for a certain Reynolds number the intensity of the disturbances increases in time the flow is unstable otherwise the flow is stable. With this idea in mind, Orr and Sommerfeld derived a differential equation which describes an eigenvalue problem whose solution can provide the critical Reynolds number, the shape of the eigenmodes and the corresponding amplification factors (see [51] and [70]). Orr-Sommerfeld equation is general and in principle can provide the solution of the linear stability problem for any parallel base flow, however due to its mathematical complexity the solution for the Blasius boundary layer ([8]) appeared years after by means of the work of Tollmien and Schlichting ([75], [64], [65]). Their main achievement was to compute the neutral stability curve for the Blasius boundary layer using the parallel flow assumption, that is the curve in the Reynolds-number and disturbance-wavelength plane which divides the stable region from the unstable one. The neutral-stability curve shows that beyond a certain value for the Reynolds number, the Blasius boundary layer is unstable with respect to two-dimensional disturbances of large wavelength if compared with the boundary layer thickness, namely the Tollmien-Schlichting waves. For the particular case of the Blasius boundary layer, the Reynolds number can be defined locally taking as reference length the distance from the leading edge to the considered position along the plate. According to this point of view the stability curve mark for each frequency of the disturbances two positions along the plate (the first branch and the second branch) that define a region in which T-S wave are amplified while outside of this region T-S waves are damped and decay. The results obtained by Tollmien and Schlichting were strongly criticized due to the lack of experimental confirmations until the work of Schubauer and Skramstad in 1947 ([67]) where hot wire data were obtained for a laminar boundary layer forced in a controlled manner by small-amplitude periodic disturbances

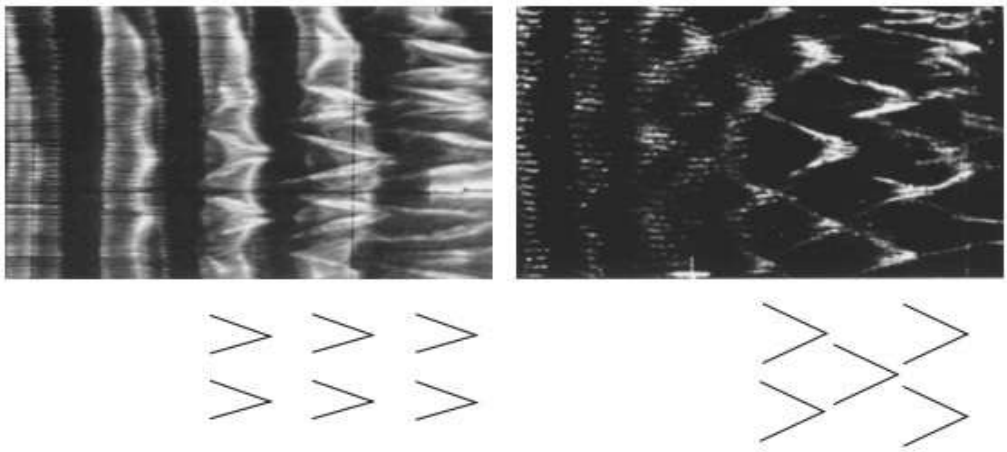

Figure 1.1 *K-type (left) and H-type (right) transition, picture taken from [31]. The reader should note the qualitatively different arrangement of the* Λ *structures in the two cases.*

created by a vibrating-ribbon. Reducing the turbulence intensity in the wind tunnel to a very low threshold they noticed quasi-harmonic oscillations inside the boundary layer right before the transition to the turbulent regime.
Schubauer and Skramstad also measured the T-S wave amplitude distribution in the wall normal direction and evaluated the position of the two branches of the neutral stability curve, all the experimental data showed substantial agreement with the calculations proposed by Schlichting in 1935 ([65]). Nowadays, the linear stage is the most understood phase in the route to transition and is used in conjunction with the receptivity theory for practical engineering calculations ([2]). The work of Klebanoff et al. in 1962 ([36]) represented a turning point in the study of natural transition and inspired new ideas and mathematical theories. The authors performed detailed hot-wire measures of the late stage of transition process using a vibrating ribbon to excite the boundary layer eigenmodes and found that for low amplitudes the T-S waves grow and then decay downstream as predicted by linear stability theory but for amplitude of about one per cent of the free-stream velocity, a three dimensional structure evolves. The flow experiences a transverse modulation characterized by a system of alternating peaks and valleys (regions of amplified and reduced wave amplitude) and at the same time a system of lon-

gitudinal vortices develops downstream. At the beginning of the breakdown, high-frequency flashes of the disturbances called "spikes" appear at each period of the T-S wave and multiply downstream until the flow is completely randomized. At that time their main observation was that boundary layer transition was essentially a three dimensional phenomenon and T-S waves represent only the first stage of a more complex process. Knapp and Roache in 1968 studied boundary-layer transition using smoke visualization and hot-wire measures [20], at the last stage of transition they observed Λ shape smoke accumulations called Λ-vortices that can be either in a staggered pattern or aligned in rows. It was recognized that the pattern of the Λ-vortices depends essentially on the amplitude of the primary wave. For low amplitudes of the primary wave the three dimensional structure that develops at late transition stages leads to a staggered pattern while for high amplitudes the aligned pattern prevails and even mixed cases are possible. Two main transition scenarios were distinguished : K-type transition characterized by an aligned pattern of the Λ structures and the appearance of spikes right before breakdown (K stands for Klebanoff who was the first author to observe this regime in 1962 [36]) and N-type transition characterized by a staggered pattern of Λ vortices and no presence of spikes. The challenge was to explain how the two dimensional plane T-S waves lead to the formation of the Λ structures and the onset of three dimensional stage, two main families of theories were developed in order to achieve this result. The first one consists on weakly non-linear resonance models of which Craik's triad ([15]) represent a milestone in literature. Craik's idea was that three dimensional Orr-Sommerfeld modes with spanwise wavenumbers $\pm\beta$ and twice the wavelength of the T-S wave (subharmonic modes) can be amplified through a resonance interaction with the T-S wave. Craik's model became popular after the experimental results of Kachanov et al. in 1977 ([32]) that measured subharmonic peaks in disturbance's spectrum during laminar boundary layer transition. The resonance mechanism described by Craik was verified by Thomas & Saric in 1981 ([73]) who also correlated the staggered arrangement of Λ structures observed by Knapp and Roache ([20]) to the presence of subharmonic signals in the disturbance spectrum during transition. The distinction between K-type and N-type transition was clear : K-type is due to non-linear excitation of harmonics of the primary wave witch leads to the aligned pattern of Λ-vortices while N-type is due to parametric resonance of the primary wave that amplify a wide band of disturbance's spectrum centered around the subharmonic of the primary wave. The second class of theories developed from the initial work of Maseev ([47]) and led with the subsequent work of Herbert ([31]) to what nowadays is known as secondary stability theory (or secondary Orr-Sommerfeld stability theory). The assumption of Herbert is that after T-S waves are established

in the boundary layer their amplitude grows until non linear effects become important, usually in this region T-S wave amplitude saturates and the flow reaches a quasi-steady state. The laminar boundary-layer modulated by T-S waves that now have reached a finite amplitude constitutes a new base flow which can be unstable with respect to three-dimensional disturbances. Under the assumption made by Herbert in his theory (see [78] and [31]), the stability of this new base flow corresponds to the stability of a linear dynamical system with periodic coefficients that can be analyzed using Floquet theory. The numerical results obtained by Herbert (see [30] , [78] , [31]) showed very good agreement with the hot-wire data of Klebanoff ([36]) both for the grow rates and the amplitude distribution of the three dimensional modes and confirmed the experimental result of the presence of subharmonic instability for quite low amplitude of the primary wave. The secondary instability mechanism described by Herbert usually precedes the final stage of transition to the turbulent regime, for this reason secondary instability calculations are sometimes used to predict transition. The "momentum theory" by Brevdo ([11]) showed that the T-S instability is of convective nature so that T-S waves cannot lead directly to transition and a different process has to take place. Although Herbert's theory explains the onset of the three-dimensional stage in natural transition it suffers from several approximations. As a matter of fact, the direct numerical simulation of the complete Navier-Stokes equations represents the most complete tool in order to study the physics of transition. Recent direct numerical simulations have revealed new features about the late transition stage, Rist et al. ([59]) showed that, in K-regime of breakdown, Λ-vortices form transitional structures (ring-like vortex) as they move downstream. A comparison between result from secondary-stability theory and from integration of the complete Navier-Stokes equation has been reported by Spalart and Yang in 1987([71]). Grow rates of three dimensional modes calculated by Herbert were compared to those obtained integrating the equation of motion, the results showed high agreement for all the amplitudes of the T-S wave. Considering the high cost that typically a direct numerical simulation requires, the theory of Herbert can be an advantageous alternative at least concerning transition prediction and deserves further investigations.

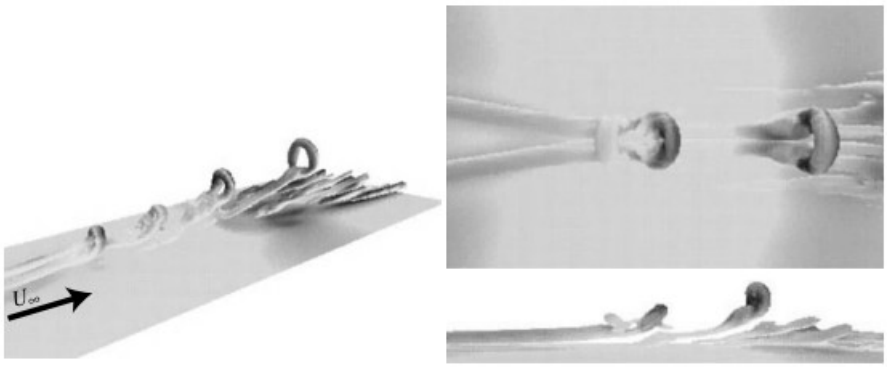

Figure 1.2 *DNS of laboratory experiments of Kachanov 1994 [34]. Picture taken from [59].*

1.2 Thesis outline

The purpose of this thesis is to perform a secondary stability analysis calculations removing the principal approximations on which the original theory by Herbert is based. As will be better clarified in the following, the assumptions by Herbert neglect some non-parallel and non-linear effects. Non-parallel effects have been studied intensely in the linear-stability-theory framework both using different formulations which account for growing effects of boundary layer (see [22]) and solving the full Navier-Stokes equations (see [21]). Better accordance between numerical and experimental data was found, however an investigation in the context of secondary stability still lacks. Concerning non-linear effects, it is known that the hydrodynamic stability problem is very sensitive to base flow structure, a more realistic evaluation of the base flow needs to be analyzed.
Chapter 1 presented an introduction to the problem and presented the main results obtained on the topic. Chapter 2 describes the mathematical formulation of the problem presenting the different approach with respect to that adopted by Herbert. Chapter 3 describes the numerical methods used and the numerical set-up. Chapter 4 illustrates the main results obtained while conclusions and future developments are presented in the final chapter.

Chapter 2

Mathematical model

This chapter illustrates the mathematical formulation of the problem in exam. In defining the problem of secondary instability, it is necessary to retrace the stages of transition briefly described in Chapter 1. Concepts from classical linear stability theory and from the original theory formulated by Herbert (see [31],[49]) will also be recalled. The receptivity theory is not the subject of this work but, before applying the theory that will be presented, calculations have to be performed to assess if the transition process is dominated by the grow of the T-S waves or by other phenomena ([55] underlines a wide range of possible scenarios that can occur in practical applications).

2.1 Base flow

In secondary stability theory, the base flow is essentially the periodic state that is reached after the primary instability mechanism leads to the growth of the T-S waves and they are established inside the boundary-layer. With the purpose of defining the base flow, a clarification regarding the basic concepts of the theory of primary stability is needed. The following treatment is far from exhaustive, only the concepts linked to the secondary stability problem formulation are mentioned. For more information regarding the derivation of the equations and the related formulas, the reader is referred to [66] or [77].

2.1.1 Linear stability theory for Blasius boundary-layer

An approximate solution of the Navier-Stokes equations for the incompressible laminar boundary layer on a flat plate, when the external velocity field is

constant, can be obtained solving the Blasius problem

$$\begin{cases} f'''(\eta) + \frac{1}{2} f(\eta) f''(\eta) = 0, \\ f(0) = 0, \ f'(0) = 0, \ f'(\infty) = 1, \end{cases} \tag{2.1}$$

where, considering a reference system centered on the leading edge with the x direction along the plate and the y direction normal to the plate, the similarity variable η is defined as

$$\eta(x, y) = y \sqrt{\frac{U_e}{\nu x}}, \tag{2.2}$$

with U_e and ν the external velocity and the kinematic viscosity of the fluid, respectively. Blasius equation (2.1) is a nonlinear ordinary differential equation of third order whose solution f is linked to the dimensionless boundary-layer velocity profile. In particular, it is possible to derive the velocity field components from the function f in the whole xy plane as

$$u_B(x, y) = U_e f'(\eta(x, y)), \tag{2.3}$$

$$v_B(x, y) = \frac{1}{2} \sqrt{\frac{U_e \nu}{x}} [\eta(x, y) f'(\eta(x, y)) - f(\eta(x, y))]. \tag{2.4}$$

The mathematical procedure that derives the Prandtl equations for the boundary-layer and the subsequent Blasius similar solution starting from the Navier-Stokes equations is not addressed here, however, extensive documentation can be found in the literature (see [66]).
The linear stability of the Blasius boundary layer with respect to two-dimensional disturbances, can be studied through the famous Orr-Sommerfeld equation

$$\begin{cases} \frac{1}{Re} (\hat{\phi}'''' - 2\hat{\alpha}^2 \hat{\phi}'' + \hat{\alpha}^4 \hat{\phi}) + i\hat{\alpha}[U(y) - \hat{c}](-\hat{\phi}'' + \hat{\alpha}^2 \hat{\phi}) + i\hat{\alpha} U(y)'' \hat{\phi} = 0, \\ \hat{\phi}(0) = 0, \ \hat{\phi}'(0) = 0, \ \hat{\phi}(\infty) = 0, \ \hat{\phi}'(\infty) = 0, \end{cases} \tag{2.5}$$

which has been made non-dimensional using the external velocity U_e as

reference velocity and the function

$$G(x) = \sqrt{\frac{\nu x}{U_e}} \tag{2.6}$$

proportional to the local boundary-layer thickness as reference length.
A slight digression is here necessary in order to define the various terms that appear in equation (2.5). Using the Orr-Sommerfeld equation, which is formulated for a parallel base flow, to study the linear stability of the boundary layer amounts to consider the stability of the local velocity profile in a certain x position along the flat plate. In the position $\bar{x}$ considered, a reference length can be defined through the function $G(x)$ that can be used in conjunction with the velocity scale U_e to define a local Reynolds number

$$Re = \frac{U_e G(\bar{x})}{\nu}. \tag{2.7}$$

The base flow of the primary instability problem, indicated as U in equation (2.5), is the local boundary-layer velocity profile non-dimensionalized, namely

$$U(y) = \frac{u_B(\bar{x}, y)}{U_e} = f'(\eta(\bar{x}, y)). \tag{2.8}$$

Instead, the quantities ϕ, α and c are related to the two-dimensional disturbance, since its stream function can be expressed as

$$\psi(x, y, t) = U_e G(\bar{x}) \hat{\phi}(y) e^{i\hat{\alpha}(\xi(x) - \hat{c}\tau(t))}, \tag{2.9}$$

where ξ and τ are the non-dimensional x coordinate and the adimensional time defined as

$$\xi = \frac{x}{G(\bar{x})}, \quad \tau = \frac{tU_e}{G(\bar{x})}. \tag{2.10}$$

In order to simplify the notation, for the subsequent developments, the dimensional quantities that characterize the disturbance are considered. For completeness, their relations with the non-dimensional ones are shown below

$$\phi = U_e G(\bar{x}) \hat{\phi}, \quad \alpha = \frac{\hat{\alpha}}{G(\bar{x})}, \quad c = U_e \hat{c}. \tag{2.11}$$

It is also worth mentioning that, in the literature, the displacement thickness $\delta(x)$ is also used as a reference length instead of the function $G(x)$, however, the mathematical formulation of the problem does not change and, for the Blasius boundary-layer, this results in a simple scaling of the relevant variables. The Orr-Sommerfeld equation is an ordinary differential equation of fourth order that together with its boundary conditions defines an eigenvalue problem. Once a Reynolds number and a real disturbance wave-number α are selected, the solution of the problem (2.5) provides the eigenfunction ϕ, which describes the disturbance, and the complex eigenvalue c that is related to the grow rate of the disturbance in time. The velocity components of the disturbance can be written, due to the stream-function definition, as

$$u_d = \Re(\frac{\partial \psi}{\partial y}) = e^{c_i}[\phi_r'(y)\cos\alpha(x - c_r t) - \phi_i'(y)\sin\alpha(x - c_r t)], \quad (2.12)$$

$$v_d = -\Re(\frac{\partial \psi}{\partial x}) = \alpha e^{c_i}[\phi_i(y)\cos\alpha(x - c_r t) - \phi_r(y)\sin\alpha(x - c_r t)], \quad (2.13)$$

where $c = c_r + ic_i$ and $\phi = \phi_r + i\phi_i$. From equations (2.12) and (2.13), it can be observed that, in the temporal linear stability theory briefly presented here, the flow is stable at a given Reynolds number if and only if all the eigenvalues have a negative imaginary part for all possible values of the disturbance wave-number α. The properties of the temporal eigenvalue spectrum for the Blasius boundary layer have been widely analyzed in the past (see [45]) but, concerning the secondary stability formulation, it is sufficient to remind that the T-S waves can be defined mathematically as the unstable eigenmodes of the Blasius boundary-layer. Moreover, it is convenient to define the quantities

$$u_{TS} = 2[\phi_r'(y)\cos\alpha(x - c_r t) - \phi_i'(y)\sin\alpha(x - c_r t)], \quad (2.14)$$

$$v_{TS} = 2\alpha[\phi_i(y)\cos\alpha(x - c_r t) - \phi_r(y)\sin\alpha(x - c_r t)], \quad (2.15)$$

which represent the velocity components of a T-S wave at a certain Reynolds number without considering the factor e^{c_i} that governs the amplification of the wave in time. In equations (2.14) and (2.15) the eigenfunction ϕ is normalized such that

$$\max_{y\in[0,\infty)} 2\|\phi'(y)\|^2 = 1 \quad (2.16)$$

for reasons that will be better clarified in the following section.

2.1.2 Base-flow definition

Before giving the definition of the base flow, it is interesting to analyse the base flow definition from classical secondary stability theory (see [30] or [31]). According to Herbert's formulation, the base flow is defined as

$$u_2 = u_B(y) + Au_{TS}(x, y, t), \qquad v_2 = Av_{TS}(x, y, t) \tag{2.17}$$

that corresponds to a superposition of the Blasius boundary layer flow, neglecting the wall normal component v_B, and the velocity field associated with the T-S wave. It should be observed that, by means of normalization (2.16), the value A has the physical meaning of measuring the maximum stream-wise r.m.s. fluctuation of the two-dimensional Blasius flow when the T-S wave has settled inside the boundary layer. Considering a reference frame moving with the T-S wave, corresponding to the change of variables $x' = x - c_r t$, the flow is periodic in x'. As anticipated, the secondary stability theory is formulated linearizing Navier-Stokes equations around this base flow, which is assumed as an exact solution of the equations of motion, and studying the stability of the resultant periodic system of differential equations.
Nevertheless, this definition of the base flow carries with it three main approximations. Firstly, the Blasius boundary-layer flow is treated as locally parallel. When writing the equations for the three-dimensional disturbances, mathematically, this inevitably leads to the loss of some contributions and also, since the growth of the boundary-layer thickness is not considered, the x direction is considered as homogeneous while in the real flow it is not. Secondly, it is assumed that the amplitude A of the T-S wave is locally constant. Practically, this assumption is satisfied if three dimensional disturbances grow significantly faster than the T-S waves. Finally, the so called "shape assumption" neglects the nonlinear distortion of the T-S $\mathbf{u_{TS}} = (u_{TS}, v_{TS})$ even when the wave has reached a finite amplitude A. Even though these last two hypotheses have been partially confirmed from experimental [36] and theoretical arguments [6], the non-linear effects become important beyond a certain value of A and classical secondary stability theory loses its reliability. The "shape-assumption" limits the applicability of this secondary stability theory only to those cases where it is understood that the wave intensity in low enough. In this work, all non-parallel and non-linear effects will be included. Therefore, it is natural to define the base flow as a solution of

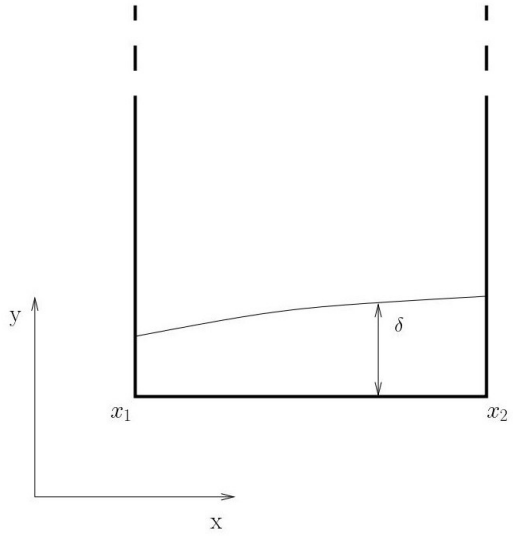

Figure 2.1 *Flow domain.*

the incompressible Navier-Stokes equations that directly includes all the contributions.
A schematization of the flow domain is shown in figure 2.1, it covers the semi-infinite space above the plate between two specified locations x_1 and x_2. In the laminar-turbulent transition, T-S waves grow, their amplitude saturates and they eventually decay downstream, therefore, the values for x_1 and x_2 have to be chosen accordingly to simulate this process. The left boundary location x_1 must correspond to a Reynolds number Re_1 at which the flow is unstable with respect to T-S waves, namely is must be beyond the first branch of the neutral stability curve. The T-S waves will grow inside the domain until they reach the position that matches the second branch, then they decay until the right boundary x_2. It is worth pointing out that in real transition, usually a group of eigenmodes is amplified inside the boundary-layer. However, as a starting point to study natural transition, numerous theories in the literature contemplate only the presence of a single wave and this is the path followed in this context. At the left boundary x_1, only the most unstable eigenmode is considered but, in principle, the effect of wave packets could also be included.
The undisturbed boundary layer flow is defined as the steady solution of the

following partial differential problem

$$\begin{cases} \frac{\partial \boldsymbol{u}}{\partial t} + (\boldsymbol{u}\cdot\nabla)\boldsymbol{u} - \frac{1}{Re}\nabla^2\boldsymbol{u} + \nabla p = 0, \\ \nabla\cdot\boldsymbol{u} = 0, \\ \boldsymbol{u}(x,y,0) = \frac{\boldsymbol{u_B}(x,y)}{U_e}, \\ \boldsymbol{u}(x_1,y,t) = \frac{\boldsymbol{u_B}(x_1,y)}{U_e}, \\ \boldsymbol{u}(x,0,t) = (0,0), \\ u(x,\infty,t) = 1, \quad \frac{\partial v}{\partial y}\big|_{(x,\infty,t)} = 0, \\ \big(\frac{\partial \boldsymbol{u}}{\partial t} + \bar{\boldsymbol{C}}\cdot\nabla\boldsymbol{u}\big)\big|_{(x_2,y,t)} = 0 \end{cases} \tag{2.18}$$

where $\boldsymbol{u}(x,y,t)$ is the velocity vector with components $\boldsymbol{u} = (u,v)$ and $p(x,y,t)$ is the dimensionless pressure. The equations are made dimensionless by choosing U_e as the velocity scale and $G(x_1)$ as reference length. Boundary conditions must be specified on the faces of the domain to properly define the differential problem. At the wall, a no-slip condition is used which prescribes null velocity components, while the conditions infinitely far from the flat plate represent the inviscid-flow approximation. The Blasius velocity profile is prescribed at the inlet of the domain and, finally, an outflow boundary condition is specified at the right face of the domain. More informations regarding the outflow boundary conditions will be provided at the end of the section since it represents a critical point in numerical transition simulations. The initial condition for the problem (2.18) is the Blasius boundary-layer. The vector $\boldsymbol{u_B} = (u_B, v_B)$ contains the velocity components defined on the whole flow domain by equations (2.3) and (2.4). Even if the Blasius solution has been used by Herbert in his theory, the hypotheses on which the latter is based (see [66]) are not acceptable in the present formulation. For this reason, a more accurate solution for the undisturbed boundary-layer flow is obtained from the solution of the problem (2.18) integrating the full incompressible Navier-Stokes equations without any particular assumption. For the next developments, it is convenient to define $\boldsymbol{U_1}(x,y)$ as the solution of problem (2.18) when a steady state is reached. Before proceeding with the definition of the base flow, an important note on the choice of the reference quantities has to be made. Differently from the Orr-Sommerfeld equation (2.5), where only a local velocity profile is considered, the flow domain includes a finite portion of the boundary layer. This fact means that no particular reference length or reference velocity is prescribed. The choice of the quantities U_e and $G(x_1)$ corresponds to taking the profile at the inlet of the domain as

reference but, even if it is convenient, this choice is not the only one possible. Even a different velocity profile can be considered but it is important that the two-dimensional flow described by (2.18) represents the velocity profile used in the Orr-Sommerfeld equation. In practice, the reference quantities U^*, L^* and ν^* must define a Reynolds number Re such that $Re = Re_1$ to match with the primary stability problem from which T-S waves are computed. The base flow for the secondary stability formulation, is defined on the basis of the solution of the problem

$$\begin{cases} \frac{\partial \boldsymbol{u}}{\partial t} + (\boldsymbol{u}\cdot\nabla)\boldsymbol{u} - \frac{1}{Re}\nabla^2\boldsymbol{u} + \nabla p = 0, \\ \nabla\cdot\boldsymbol{u} = 0, \\ \boldsymbol{u}(x,y,0) = \boldsymbol{U_1}(x,y), \\ \boldsymbol{u}(x_1,y,t) = \boldsymbol{U_1}(x_1,y) + \bar{A}\boldsymbol{u_{TS}}(x_1,y,t), \\ \boldsymbol{u}(x,0,t) = (0,0), \\ u(x,\infty,t) = 1, \quad \frac{\partial v}{\partial y}\big|_{(x,\infty,t)} = 0, \\ \left(\frac{\partial \boldsymbol{u}}{\partial t} + \bar{\boldsymbol{C}}\cdot\nabla\boldsymbol{u}\right)\big|_{(x_2,y,t)} = 0, \end{cases} \tag{2.19}$$

where this time the steady undisturbed solution $\boldsymbol{U_1}(x,y)$ is used as initial condition and the T-S perturbation field is superimposed on the Blasius profile at the inflow boundary. In other words, $\boldsymbol{u_{TS}} = (u_{TS}, v_{TS})$ is the velocity field (given by equations (2.14) and (2.15)) of the most unstable eigenmode of the Orr-Sommerfeld problem (2.5) solved for $Re = Re_1$, that corresponds to the inlet position x_1. It should be noted that there is a strong similarity between the Herbert base flow (2.17) and the velocity field imposed at the inlet of the domain. Indeed, the constant $\bar{A}$ has the same meaning of measuring the maximum stream-wise r.m.s fluctuation of the flow, however, this is only valid at the inlet section not in the whole flow field. In general, inside the domain, the amplitude of the T-S wave will grow and then decay, particular attention must be given to compare results from original Herbert theory and that from the formulation presented in this work.
In order to apply the Floquet theory to study the secondary instability, the base flow is required to be periodic. In the original theory by Herbert, as already pointed out, by means of the "shape assumption" a periodic base flow is obtained by construction. In the present context, it should be noted that the problem (2.19) consists in solving the Navier-Stokes equations forced by the T-S perturbation field $\boldsymbol{u_{TS}}$, which is a periodic function of time.

Therefore, after an initial transient occurs, the solution of the problem (2.19) (unless it is unstable) is expected to be periodic with the same frequency of the T-S wave. This periodic solution, named $\boldsymbol{U_2}(x, y, t)$ from this point on, represent the modulated boundary-layer as a result of T-S waves excitation and is in fact the base flow around which secondary stability theory can be developed. Mathematically, the properties of $\boldsymbol{U_2}(x, y, t)$ can be written as

$$\boldsymbol{U_2}(x, y, t) = \boldsymbol{U_2}(x, y, t + T), \quad \text{with} \quad T = \frac{2\pi}{\alpha c_r}. \tag{2.20}$$

Various models have been used in the past to simulate laminar-turbulent transition. In the already mentioned work of Spalart [71], the incompressible Navier-Stokes equations are solved numerically in a three-dimensional flow domain above the flat plate. Imposing a two-dimensional T-S wave and a random three-dimensional disturbance at the inlet boundary, the authors were able to verify the results of Herbert theory and to compare them with laboratory experiments. In the work of Fasel [21] a very similar procedure to the one described in this work was pursued to estimate the importance of the non-parallel effects in the grow rate of T-S waves. All the different models used, including the one described here, have in common that they allow one to represent the disturbance amplification in the downstream direction, instead of in time, which is the correct way to match experimental results. In a certain sense the problem (2.19) represents the mathematical counterpart of a wide range of laboratory experiments where a vibrating ribbon is used to excite the boundary-layer eigenmodes (see [60], [67] and many others). Moreover, the proposed procedure can be easily generalized to include further effects. For instance, the more general Falkner-Skan boundary-layer profile (see [66]) can be considered instead of the Blasius one to account for non-uniform free-stream velocity and also multiple Orr-Sommerfeld modes can be imposed at the inflow boundary to analyze wave-packet effects. A fundamental topic is represented by the outflow boundary condition used in (2.18) and (2.19). The mathematical domain is a truncation of the real physical domain, this implies that an artificial condition has to be imposed to correctly define the differential problem. For transition simulations in particular, the role of the outflow boundary condition is to allow the propagation of disturbances outside of the domain without unphysical reflections on the boundary. In the mathematical problems defined in this section, the Orlanski boundary condition has been used. Even if a wide range of possible choices is available in the literature (see [10], [41], [42]) and specific conditions for transition simulation have been developed [37], the Orlanski condition has demonstrated comparatively good features (see [79]). As can be seen in the problems (2.18)

and (2.19), the outflow condition states that the velocity field must satisfy the advection equation $\frac{\partial \boldsymbol{u}}{\partial t} + \bar{\boldsymbol{C}} \cdot \nabla \boldsymbol{u}$. The quantity $\bar{\boldsymbol{C}}$ represents a mean outflow convection speed, many choices are possible for its definition. In [50] it is shown that with an accurate approximation of $\bar{\boldsymbol{C}}$, for problems involving a single wave propagation, no unphysical reflection is observed at the boundary of the domain. Although, in principle, any outflow condition can be imposed to correctly define the partial differential problems, this convective condition has been chosen looking at the numerical solution of the problem where the absence of reflections is important to verify the correctness of the results.
Before proceeding in the formulation of the secondary stability problem, it is necessary to clarify the choice of the parallel linear stability theory to evaluate the shape of the T-S wave since, for the purposes of this work, it seems a contradiction. Since the full Navier-Stokes equations are solved, the base flow accounts for non-parallel and non-linear effects. However, it can be questioned if the use of a more complex non-parallel stability theory to evaluate the T-S forcing at the inlet would lead to a more realistic two-dimensional base flow. In the work of Fasel [21], in which the same base flow has been obtained, it is shown that even using non-parallel theories the resultant two-dimensional flow experiences negligible variations. This is due to the fact that non-parallel theories mainly affect the grow rates of the eigenmodes (that are not considered for the present formulation) but have little influence on the eigenfunction shape. Considering the additional complexity from the implementation point of view and the little variation of the results, classical linear stability theory has been chosen.

2.2 Secondary stability problem

This section illustrates the secondary stability problem formulation, the mathematical procedure is analogous to that pursued by Herbert [31], although the different nature of the base flow leads to significant differences that will be pointed out.
As common practice also in linear stability theory, unsteady three-dimensional disturbances, $\boldsymbol{u_3}(x, y, z, t) = (u_3, v_3, w_3)$ and $p_3(x, y, z, t)$, are superimposed on the two-dimensional base flow formulated in the previous section and described by the quantities $\boldsymbol{U_2}(x, y, t) = (U_2, V_2)$ and $p_2(x, y, t)$.

$$u(x, y, z, t) = U_2(x, y, t) + u_3(x, y, z, t), \tag{2.21}$$
$$v(x, y, z, t) = V_2(x, y, t) + v_3(x, y, z, t), \tag{2.22}$$
$$w(x, y, z, t) = w_3(x, y, z, t), \tag{2.23}$$
$$p(x, y, z, t) = p_2(x, y, t) + p_3(x, y, z, t). \tag{2.24}$$

The equations governing the disturbances, neglecting the non-linear terms, are the Navier-Stokes equations linearized around the base flow

$$\begin{cases} \frac{\partial \boldsymbol{u_3}}{\partial t} + (\boldsymbol{U_2} \cdot \nabla)\boldsymbol{u_3} + (\boldsymbol{u_3} \cdot \nabla)\boldsymbol{U_2} - \frac{1}{Re}\nabla^2 \boldsymbol{u_3} + \nabla p_3 = 0, \\ \nabla \cdot \boldsymbol{u_3} = 0 \end{cases} \tag{2.25}$$

which requires boundary conditions for the perturbation quantities

$$\boldsymbol{u_3}(x_1, y, z, t) = (0, 0, 0), \tag{2.26}$$
$$\boldsymbol{u_3}(x, 0, z, t) = (0, 0, 0), \tag{2.27}$$
$$\boldsymbol{u_3}(x, \infty, z, t) = (0, 0, 0), \tag{2.28}$$
$$\Big(\frac{\partial \boldsymbol{u_3}}{\partial t} + \bar{\boldsymbol{C}} \cdot \nabla \boldsymbol{u_3}\Big)\Big|_{(x_2, y, z, t)} = 0. \tag{2.29}$$

The equations (2.27) and (2.28) represent the decay of the disturbance near the flat plate and infinitely far form it, while the equation (2.29) is the already mentioned convective outflow boundary condition. The equation (2.29) states that the base flow is undisturbed at the left boundary of the domain. Several characteristics of the three-dimensional disturbances are known from the laboratory experiments which simulate late transition stages

[36]. Typically, the three-dimensional structure that originates from secondary instability mechanism evolves after that the T-S waves have settled inside the boundary-layer and their amplitude has grown to the one per cent of the free-stream velocity. In addition, the three dimensional stage occupies about one wavelenght of the primary wave until the flow is completely randomized. Since the inlet boundary represents physically the location at which T-S waves are excited, it is reasonable to assume that the amplitude of the thee-dimensional disturbance is very low. On the other hand, further downstream where the amplitude of the T-S waves is high enough, the amplitude of the disturbances is expected to be considerable.
Equations (2.25) represents a system of partial differential equations whose coefficients are periodic in time with the same period of the T-S wave. Since the base flow is independent from the span-wise coordinate, the solution can be expanded in Fourier series in this direction. The disturbance velocity field can be written as

$$\left\{ \begin{array}{c} u_3 \\ v_3 \\ w_3 \end{array} \right\} = \left\{ \begin{array}{c} \hat{u}(x,y,t) \\ \hat{v}(x,y,t) \\ i\hat{w}(x,y,t) \end{array} \right\} e^{i\beta z} \tag{2.30}$$

and the same applies for the pressure field

$$p_3 = \hat{p}(x,y,t)e^{i\beta z}, \tag{2.31}$$

where β is a real number and represents the spanwise wavenumber of the three-dimensional disturbance.
Expanding the equations (2.25) term by term

$$\begin{cases} \frac{\partial u_3}{\partial t} + U_2\frac{\partial u_3}{\partial x} + v_3\frac{\partial U_2}{\partial y} + \frac{\partial p_3}{\partial x} - \frac{1}{Re}\nabla^2 u_3 + \left[u_3\frac{\partial U_2}{\partial x} + V_2\frac{\partial u_3}{\partial y}\right] = 0, \\ \frac{\partial v_3}{\partial t} + U_2\frac{\partial v_3}{\partial x} + \frac{\partial p_3}{\partial y} - \frac{1}{Re}\nabla^2 v_3 + \left[u_3\frac{\partial V_2}{\partial x} + V_2\frac{\partial v_3}{\partial y} + v_3\frac{\partial V_2}{\partial y}\right] = 0, \\ \frac{\partial w_3}{\partial t} + U_2\frac{\partial w_3}{\partial x} + \frac{\partial p_3}{\partial z} - \frac{1}{Re}\nabla^2 w_3 + \left[V_2\frac{\partial w_3}{\partial y}\right] = 0, \\ \frac{\partial u_3}{\partial x} + \frac{\partial v_3}{\partial y} + \frac{\partial w_3}{\partial z} = 0, \end{cases} \tag{2.32}$$

it is possible to highlight the non-parallel terms, placed in square brackets, that are neglected in the original secondary stability theory but are taken into account in the present formulation. In addition, it can be seen that, by means of the property (2.30), the equations have a two-dimensional nature. In fact, the equations (2.32) can be formulated also for the variables $\hat{u}$, $\hat{v}$, $\hat{w}$

and $\hat{p}$ simplifying the factor $e^{i\beta z}$ which appears in all the terms. The resulting equations are shown below

$$\begin{cases} \frac{\partial \hat{u}}{\partial t} + U_2 \frac{\partial \hat{u}}{\partial x} + \hat{v} \frac{\partial U_2}{\partial y} + \frac{\partial \hat{p}}{\partial x} - \frac{1}{Re}(\hat{\nabla}^2 \hat{u} - \beta^2 \hat{u}) + \left[\hat{u} \frac{\partial U_2}{\partial x} + V_2 \frac{\partial \hat{u}}{\partial y}\right] = 0, \\ \frac{\partial \hat{v}}{\partial t} + U_2 \frac{\partial \hat{v}}{\partial x} + \frac{\partial \hat{p}}{\partial y} - \frac{1}{Re}(\hat{\nabla}^2 \hat{v} - \beta^2 \hat{v}) + \left[\hat{u} \frac{\partial V_2}{\partial x} + V_2 \frac{\partial \hat{v}}{\partial y} + \hat{v} \frac{\partial V_2}{\partial y}\right] = 0, \\ \frac{\partial \hat{w}}{\partial t} + U_2 \frac{\partial \hat{w}}{\partial x} + \beta \hat{p} - \frac{1}{Re}(\hat{\nabla}^2 \hat{w} - \beta^2 \hat{w}) + \left[V_2 \frac{\partial \hat{w}}{\partial y}\right] = 0, \\ \frac{\partial \hat{u}}{\partial x} + \frac{\partial \hat{v}}{\partial y} - \beta \hat{w} = 0 \end{cases} \tag{2.33}$$

where $\hat{\nabla} = \frac{\partial^2}{\partial x^2} + \frac{\partial^2}{\partial y^2}$ is the two-dimensional Laplacian operator. It can be observed that in (2.33) only the derivatives with respect to the x and y directions appear. This is due to the fact that the derivatives with respect to the span-wise direction are replaced by algebraic operations by virtue of the Fourier transform. Therefore, the solutions of the problem (2.33) are functions of x, y and t only and are defined on the same two-dimensional domain of the base flow. The boundary conditions for the disturbances can also be easily extended for the quantities $\hat{u}$, $\hat{v}$ and $\hat{w}$ removing the dependence on the span-wise coordinate z. The system (2.33), in conjunction with the relations (2.30) and (2.31) and with the boundary conditions (2.26), (2.27), (2.28) and (2.29) defines the secondary stability eigenvalue problem. The Floquet theory can then be applied to the system (2.33) due to the time periodicity (2.20) and gives an insight into the shape of the eigenmodes. The theory states that the eigenfunctions $\hat{u}$, $\hat{v}$, $\hat{w}$ and $\hat{p}$ consist on a function of t that is periodic with period $\frac{2\pi}{\alpha c_r}$ multiplied by a characteristic factor, namely

$$\begin{Bmatrix} \hat{u}(x,y,t) \\ \hat{v}(x,y,t) \\ \hat{w}(x,y,t) \\ \hat{p}(x,y,t) \end{Bmatrix} = e^{\sigma t} \begin{Bmatrix} \bar{u}(x,y,t) \\ \bar{v}(x,y,t) \\ \bar{w}(x,y,t) \\ \bar{p}(x,y,t) \end{Bmatrix} = e^{\sigma t} \sum_{m=-\infty}^{\infty} \begin{Bmatrix} u_m(x,y) \\ v_m(x,y) \\ w_m(x,y) \\ p_m(x,y) \end{Bmatrix} e^{im\alpha c_r t} \tag{2.34}$$

where $\sigma = \sigma_r + i\sigma_i$ and is called characteristic exponent of the Floquet system. The Fourier series has been used to make explicit the periodic dependence of the bar quantities with respect to time. In expression (2.34) it is sufficient to consider $-\frac{\alpha c_r}{2} < \sigma_i \leq \frac{\alpha c_r}{2}$ since the values σ and $\sigma + ik\alpha c_r$ would give identical modes for any positive integer k, provided that the Fourier series is renumbered.

Three classes of modes can be identified:

Fundamental modes, $\sigma_i = 0$:

$$\left\{ \begin{array}{c} u_{3f} \\ v_{3f} \\ w_{3f} \\ p_{3f} \end{array} \right\} = e^{i\beta z} e^{\sigma_r t} \sum_{m \ even} \left\{ \begin{array}{c} u_m(x,y) \\ v_m(x,y) \\ iw_m(x,y) \\ p_m(x,y) \end{array} \right\} e^{im\frac{\alpha c_r}{2}t}. \tag{2.35}$$

Subharmonic modes, $\sigma_i = \frac{\alpha c_r}{2}$:

$$\left\{ \begin{array}{c} u_{3s} \\ v_{3s} \\ w_{3s} \\ p_{3s} \end{array} \right\} = e^{i\beta z} e^{\sigma_r t} \sum_{m \ odd} \left\{ \begin{array}{c} u_m(x,y) \\ v_m(x,y) \\ iw_m(x,y) \\ p_m(x,y) \end{array} \right\} e^{im\frac{\alpha c_r}{2}t}. \tag{2.36}$$

Detuned modes, $0 < |\frac{2\sigma_i}{\alpha c_r}| < 1$:

$$\left\{ \begin{array}{c} u_{3d} \\ v_{3d} \\ w_{3d} \\ p_{3d} \end{array} \right\} = e^{i\beta z} e^{\sigma_r t} \sum_{m \ even} \left\{ \begin{array}{c} u_m(x,y) \\ v_m(x,y) \\ iw_m(x,y) \\ p_m(x,y) \end{array} \right\} e^{i(m+\frac{2\sigma_i}{\alpha c_r})\frac{\alpha c_r}{2}t}. \tag{2.37}$$

The fundamental and subharmonic modes satisfy

$$\boldsymbol{u_f}(x,y,z,t) = \boldsymbol{u_f}(x,y,z,t+T), \quad \boldsymbol{u_s}(x,y,z,t) = \boldsymbol{u_s}(x,y,z,t+2T) \tag{2.38}$$

and are associated with primary resonance and principal parametric resonance in the Floquet system, respectively. The detuned modes are associated with combination resonance and, in order to construct a real physical solution, two complex-conjugate modes with opposite detuning $\pm\frac{2\sigma_i}{\alpha c_r}$ are required.
An important difference of the present formulation with respect to the original one proposed by Herbert [30], consists in having two-dimensional modes. This fact is a direct consequence of the inclusion of the non-parallel effects that do not allow to consider the x direction as homogeneous. In the theory of Herbert, the evolution of the disturbances can be analyzed either in the temporal or the spatial framework (see [31]). Instead, in the proposed formulation the temporal grow of the modes in considered while the spatial evolution is

represented by the shape of the eigenfunctions. The stability properties of the modes are related to the real part of the characteristic exponent σ, in particular an eigenmode is stable if

$$\sigma_r < 0, \tag{2.39}$$

which leads to an an asymptotically decaying amplitude in time. Similarly to the primary stability theory, the solution of the secondary stability eigenvalue problem provides, after fixing the span-wise wavenumber of the disturbance β, the eigenfunctions, that describe the shape of the three-dimensional disturbance, and the corresponding eigenvalue σ that indicates if the considered mode is stable or not. The secondary stability analysis can provide important information regarding the span-wise wavenumber of the most amplified disturbance, the class of the more unstable modes, how the amplitude of the primary wave influences the results and so on.

2.2.1 Basic Floquet theory concepts

Despite the secondary stability problem has been defined, a slightly different point of view is useful in view of the description of the numerical solution method that will be provided in the following chapter. Very few ideas of the Floquet theory and their relations with the problem in exam will be discussed following an intuitive approach. However a complete and mathematically rigorous descriptions of the theory can be found in [52] or [58]. Let us consider the linear periodic continuous system

$$\begin{cases} x' = A(t)x, \\ x(t_0) = x_0, \end{cases} \tag{2.40}$$

in which x represents the state of the system while $A(t)$ is a linear operator with periodic coefficients of period T. The state transition matrix is the solution of the following differential matrix equation:

$$\begin{cases} \Phi'(t,\tau) = A(t)\Phi(t,\tau), \\ \Phi(\tau,\tau) = I \end{cases} \tag{2.41}$$

The state transition matrix provides the relationship between the value of the state at a certain time τ and the value reached at a subsequent generic instant t, that is

$$x(t) = \Phi(t,\tau)x(\tau). \tag{2.42}$$

Of particular interest for the stability analysis of the periodic systems is the state transition matrix over one period, that is called the monodromy matrix and is defined as $\Psi(\tau) = \Phi(\tau + T, \tau)$. As can be derived from (2.42), the monodromy matrix allows one to evaluate the evolution of the state after a time period T, namely

$$x(\tau + T) = \Psi(\tau)x(\tau), \tag{2.43}$$

where τ can be a generic time instant. Considering the state $x(k) = x(\tau + kT)$,

with k positive integer, its value can be evaluated, knowing the monodromy matrix, by the discrete-time equation:

$$x(k) = \Psi(\tau)^k x(0). \tag{2.44}$$

The equation (2.44) shows the link between the stability of the periodic system and the eigenvalues of the monodromy matrix. The latter are called characteristic multipliers and it can be proved that are time-independent, therefore they represents a property of the system itself. A continuous periodic system is stable if and only if its characteristic multipliers have modulus lower than one.
The relationship between the secondary stability problem and these basic Floquet theory notions, can be clarified observing that formally, by means of the linearity property, the problem (2.33) can be reformulated as

$$\frac{\partial}{\partial t}\begin{Bmatrix} \hat{u} \\ \hat{v} \\ \hat{w} \\ \hat{p} \end{Bmatrix} = \begin{bmatrix} \quad SSO \quad \end{bmatrix} \begin{Bmatrix} \hat{u} \\ \hat{v} \\ \hat{w} \\ \hat{p} \end{Bmatrix}, \tag{2.45}$$

where "SSO" symbolizes the Secondary Stability differential Operator whose coefficients are periodic in time with period T. Considering equation (2.34), it can be noted that

$$\begin{Bmatrix} \hat{u}(x,y,t+T) \\ \hat{v}(x,y,t+T) \\ \hat{w}(x,y,t+T) \\ \hat{p}(x,y,t+T) \end{Bmatrix} = \begin{Bmatrix} \bar{u}(x,y,t+T) \\ \bar{v}(x,y,t+T) \\ \bar{w}(x,y,t+T) \\ \bar{p}(x,y,t+T) \end{Bmatrix} e^{\sigma t} e^{\sigma T} = \begin{Bmatrix} \hat{u}(x,y,t) \\ \hat{v}(x,y,t) \\ \hat{w}(x,y,t) \\ \hat{p}(x,y,t) \end{Bmatrix} e^{\sigma T}, \tag{2.46}$$

but, in analogy to what has been shown in this section, it can be written that

$$\begin{bmatrix} \quad MO \quad \end{bmatrix} \begin{Bmatrix} \hat{u}(x,y,t) \\ \hat{v}(x,y,t) \\ \hat{w}(x,y,t) \\ \hat{p}(x,y,t) \end{Bmatrix} = \begin{Bmatrix} \hat{u}(x,y,t) \\ \hat{v}(x,y,t) \\ \hat{w}(x,y,t) \\ \hat{p}(x,y,t) \end{Bmatrix} e^{\sigma T}, \tag{2.47}$$

where "MO" refers generically to the monodromy operator associated with the system (2.45). The functions $\hat{u}$, $\hat{v}$, $\hat{w}$ and $\hat{p}$ describe particular shapes of

the disturbances that are only scaled over a period. In other words, they are eigenfunctions of the monodromy operator associated with the eigenvalue $e^{\sigma T}$ that is the characteristic multiplier. It should be noted that the condition on the characteristic exponents (2.39) is equivalent to the condition for the characteristic multipliers given in this section. The fist ones are related to the asymptotic evolution of the disturbances in time, the latter are related to the discrete evolution as shown in (2.44).
In practice, the solution of the secondary stability problem can be obtained computing the spectrum of the monodromy operator and the corresponding eigenmodes. However, due to the complexity of the problem, the monodromy operator can be only formally defined. The mathematical problem of computing the spectrum of operators for which an explicit expression is not available has already been addressed in literature. For instance, the Arnoldi method proposed for the first time in [3], represents an efficient algorithm to compute the spectrum of large sparse matrices. The iterative procedure of the method will be described in the following chapter but, in this context, it is important to highlight that it only requires to compute the action of the operator on a vector. Looking specifically at the problem in exam this reduces to evaluate

$$\begin{Bmatrix} u(x,y,t+T) \\ v(x,y,t+T) \\ w(x,y,t+T) \\ p(x,y,t+T) \end{Bmatrix} = \begin{bmatrix} \\ MO \\ \\ \end{bmatrix} \begin{Bmatrix} u(x,y,t) \\ v(x,y,t) \\ w(x,y,t) \\ p(x,y,t) \end{Bmatrix}. \tag{2.48}$$

In other words, Arnoldi method requires the action of the monodromy matrix on a generic vector, as represented in the right-hand side of the previous expression. By means of (2.43), this corresponds to the evolution of the disturbance a period T forward in time. Even if the monodromy operator is unknown, the term at the left-hand-side in (2.48) can be obtained simply integrating the equations (2.33) for the three-dimensional disturbance over one time period T of the T-S wave.

Chapter 3

Numerical methods

This chapter deals with the numerical tools employed in the solution of the secondary stability problem. In particular, the basic features of a Petrov-Galerkin method used to solve the primary stability problem are presented in the first section. Afterwards, the methods to discretize the incompressible Navier-Stokes equations and to compute the eigenvalues of the monodromy matrix are also illustrated. A description of the computational setup and all the numerical parameters adopted, along with the definition of the different cases for which results are obtained, is provided at the end of the chapter.

3.1 Galerkin-Laguerre method for primary stability analysis

The primary instability analysis requires the numerical solution of both the Blasius equation (2.1) and the Orr-Sommerfeld eigenvalue problem (2.5). Both problems deal with the numerical difficulty of having a semi-infinite domain on which the solution is defined. In order to face this difficulty, several approaches have been adopted that mostly rely on a truncation or a mapping of the mathematical domain followed by a discretization by means of finite difference or finite elements. For the Blasius boundary-layer in particular, spectral collocation solvers have also been used (see [54] or [53]) that represents a valid and reliable alternative. Although the spectral formulation leads to methods simple to implement and does not require any truncation of the mathematical domain, the collocation approach can lead to poorly conditioned discrete operators especially in the case where high order derivatives are present. On the other hand, the Galerkin approach can result in sparse and well conditioned discrete operators as it is shown

in [68]. It is worth mentioning that the Galerkin approach is supported by convergence and error estimation theorems that also apply to spectral methods in semi-infinite domains (see [68]). In the next section, the basic theoretical concepts of a Galerkin method based on the Laguerre functions are exposed mainly following [4], in which the latter has been proposed for the solution of self-similar problems of the boundary-layer theory.

3.1.1 Weak variational formulation

Let us consider initially the Blasius problem (2.1) that, for reader's convenience, is again reported below

$$f'''(\eta) + \frac{1}{2} f(\eta) f''(\eta) = 0, \tag{3.1}$$

$$f(0) = 0,\ f'(0) = 0,\ f'(\infty) = 1. \tag{3.2}$$

The Blasius problem is homogeneous with the exception of the condition at infinity on the first derivative of f. The latter, namely $f'(\infty) = 1$, implies that the solution f behaves asymptotically as $f(\eta) = \eta + k$ when $\eta \to \infty$, where k is a constant that has to be found from the numerical solution of the problem. The purpose of the method is to approximate the solution of the problem through an expansion based on the Laguerre functions (see [69]). However, the Laguerre functions cannot be employed directly to approximate the variable $f(\eta)$ due to its behaviour at infinity and the problem has to be redefined for a new suitable variable. The new variable, named $\psi(\eta)$, is defined as

$$f(\eta) = \psi(\eta) + \eta(1 - e^{-\frac{\eta}{2}}). \tag{3.3}$$

At this point, the Blasius problem (2.1) can be reformulated for the function ψ considering the relations between the derivatives of f and those of ψ, these relations are shown below

$$\begin{aligned} f'(\eta) &= \psi'(\eta) + 1 - \left(1 - \frac{1}{2}\eta\right) e^{-\frac{\eta}{2}}, \\ f''(\eta) &= \psi''(\eta) + \left(1 - \frac{1}{4}\eta\right) e^{-\frac{\eta}{2}}, \\ f'''(\eta) &= \psi'''(\eta) - \frac{1}{8}(6 - \eta) e^{-\frac{\eta}{2}}. \end{aligned} \tag{3.4}$$

The equation for the new unknown $\psi(\eta)$ can be derived substituting the expressions (3.4) in the Blasius equation (3.1). The new equation for the variable $\psi(\eta)$ reads

$$\psi''' + \frac{1}{2}\psi\psi'' + \frac{1}{2}a(\eta)\psi'' + \frac{1}{2}b(\eta)\psi = r(\eta), \tag{3.5}$$

where $a(\eta)$, $b(\eta)$ and $r(\eta)$ denote the functions

$$\begin{aligned} a(\eta) &= \eta\left(1 - e^{-\frac{\eta}{2}}\right), \\ b(\eta) &= \left(1 - \frac{1}{4}\eta\right)e^{-\frac{\eta}{2}}, \\ r(\eta) &= \frac{1}{8}\left[\eta^2 - 5\eta + 6\right]e^{-\frac{\eta}{2}} + \frac{1}{8}(4-\eta)\eta e^{-\eta}. \end{aligned} \tag{3.6}$$

The boundary conditions for the unknown $\psi(\eta)$ can be derived directly from those of the Blasius problem (3.2) exploiting the definition (3.3). In particular, the function $\psi(\eta)$ must satisfy the conditions

$$\psi(0) = 0,\ \psi'(0) = 0,\ \psi'(\infty) = 0, \tag{3.7}$$

that are now fully homogeneous. By means of the change of variable (3.3), the solution ψ tends to a constant at infinity, namely $\psi(\eta) = k$ as $\eta \to \infty$. As will be better clarified in the following, the Laguerre functions are only suitable to approximate functions decaying at infinity. However, the function ψ can be seen as $\psi(\eta) = k + w(\eta)$, that is a constant k plus a function $w(\eta)$ decaying at infinity. In practise, the Laguerre functions can be used to represent ψ if they are slightly modified to take into account the constant part k. Before giving a definition of the basis functions, the Galerkin method requires to write the differential problem for ψ, composed by the equation (3.5) and the boundary conditions (3.7), in a weak variational form. The weak formulation can be derived multiplying equation (3.5) by a test function $v(\eta)$ and integrating in the whole domain, namely

$$\int_0^\infty v(\eta)\left[\psi''' + \frac{1}{2}\psi\psi'' + \frac{1}{2}a(\eta)\psi'' + \frac{1}{2}b(\eta)\psi\right]d\eta = \int_0^\infty v(\eta)r(\eta)d\eta, \tag{3.8}$$

where the test function $v(\eta)$ must be chosen asymptotically homogeneous to be integrable in the whole mathematical domain. As common in the derivation of the weak variational form, the high order derivatives of the solution ψ can be moved to the test function v integrating by part the terms in equation (3.8).

$$
\begin{aligned}
&-\int_0^\infty v'(\eta)\psi''d\eta + \left[v(\eta)\psi''\right]_0^\infty - \frac{1}{2}\int_0^\infty [v(\eta)\psi]'\psi' d\eta + \frac{1}{2}\left[v(\eta)\psi\psi'\right]_0^\infty \\
&-\frac{1}{2}\int_0^\infty [v(\eta)a(\eta)]'\psi' d\eta + \frac{1}{2}\left[v(\eta)a(\eta)\psi'\right]_0^\infty + \frac{1}{2}\int_0^\infty v(\eta)b(\eta)\psi d\eta \qquad (3.9)\\
&=\int_0^\infty v(\eta)r(\eta)d\eta.
\end{aligned}
$$

The test function $v(\eta)$, for the moment left unspecified, can be chosen to satisfy the conditions

$$
v(0) = 0 \quad \text{and} \quad v(\infty) = 0, \qquad (3.10)
$$

that nullify the boundary terms present in equation (3.9). It should be noted that, for the terms in (3.9) to be properly defined, a different level of regularity is required for the test function $v(\eta)$ and the solution $\psi(\eta)$. In fact, the weak form of the Blasius problem constitutes a Petrov-Galerkin formulation since $v(\eta)$ and $\psi(\eta)$ belong to two different functional spaces. Finally, the weak formulation can be written as:

$$
\begin{aligned}
&\textit{find } \psi \in \mathcal{K} = \left\{u(\eta) = k + w(\eta) | k \in \mathbb{R}, w \in H^2(0,\infty), u(0) = u'(0) = 0\right\}\\
&\textit{such that:}\\
&-\int_0^\infty v'(\eta)\psi''d\eta - \frac{1}{2}\int_0^\infty \left[v'(\eta)\psi\psi' + v(\eta)\left(\psi'\right)^2\right]d\eta\\
&+\frac{1}{2}\int_0^\infty \left\{-\left[v(\eta)a(\eta)\right]'\psi' + v(\eta)b(\eta)\psi\right\}d\eta = \int_0^\infty v(\eta)r(\eta)d\eta,\\
&\quad \forall v \in H_0^1(0,\infty)
\end{aligned}
\qquad (3.11)
$$

where $H_0^1(0,\infty) = \{v \in H^1(0,\infty), v(0) = 0\}$.

3.1.2 Laguerre functions

The Galerkin method allows one to convert the continuous operator problem (3.11) to a discrete problem by choosing a suitable set of basis functions that represent a subspace of the functional spaces $\mathcal{K}(0,\infty)$ and $H_0^1(0,\infty)$. In order to define the basis functions, some general concepts regarding Laguerre polynomials and Laguerre functions are recalled below. A complete discussion regarding the theoretical results of the Laguerre spectral approximations is beyond the scope of this work but, due to their importance, the main results will be briefly mentioned. For a complete and rigorous treatment of this subject, the reader is referred to [69] and [44].
The generalized Laguerre polynomials (GLPs), denoted by $\mathcal{L}_n^{(\alpha)}(x)$ with $\alpha > -1$, are the eigenfunctions of the Sturm-Liouville problem

$$x^{-\alpha}e^{x}\partial_x\left(x^{\alpha+1}e^{-x}\partial_x\mathcal{L}_n^{(\alpha)}(x)\right) + \lambda_n\mathcal{L}_n^{(\alpha)}(x) = 0, \quad x \in (0,\infty), \tag{3.12}$$

associated with the eigenvalues $\lambda_n = n$ and can be defined by the following formula

$$\mathcal{L}_n^{(\alpha)}(x) := \frac{x^{-\alpha}e^{x}}{n!}\frac{d^n}{dx^n}\left(e^{-x}x^{n+\alpha}\right), \quad \text{for} \quad n = 0,1,2,\ldots. \tag{3.13}$$

In the literature they are also called associated Laguerre polynomials and represent the general case of the classical Laguerre polynomials which are obtained for the case $\alpha = 0$. In other words

$$\mathcal{L}_n^{(0)}(x) = \mathcal{L}_n(x), \tag{3.14}$$

where $\mathcal{L}_n(x)$ are the simple Laguerre polynomials that are more frequently used in practical application. An important property of the GLP is that they are mutually orthogonal in the functional space $L_w^2(0,\infty) = \{v : \|v\|_{L_w^2} < \infty\}$ equipped with the following inner product and norm:

$$(u,v)_w = \int_0^\infty u(x)v(x)w_\alpha(x)dx, \quad \|u\|_w = (u,u)_w^{\frac{1}{2}}, \tag{3.15}$$

where the weight function $w_\alpha(x)$ is defined as

$$w_\alpha(x) = x^{\alpha}e^{-x}. \tag{3.16}$$

For the simpler case of the classical Laguerre polynomials this property can be written as

$$\int_0^\infty \mathcal{L}_i(x)\mathcal{L}_j(x)e^{-x}dx = \delta_{ij}, \quad \forall i,j \geq 0, \tag{3.17}$$

and means that they define an orthogonal basis in the Hilbert space $L^2_w(0,\infty)$. Due to the exponentially decaying weight in the norm (3.15), it can be shown that the direct application of the Galerkin approach based on the Laguerre polynomials leads, from a theoretical point of view, to meaningful results only inside small intervals. Moreover, the GLPs are not suitable for practical implementations due to their wild behaviour at infinity. A rigorous demonstration of this briefly mentioned result can be found in [68] or [69] together with more properties of the GLPs that are not reported here. The GLPs have received limited interest for solving problems in unbounded domains, nevertheless, the Galerkin-Laguerre approach has been applied successfully to some properly transformed non-linear PDEs in [29]. It can be shown that the proposed transformation of the equations corresponds to use the Laguerre functions, described below, instead of the GLPs. The generalized Laguerre functions (GLFs) are defined by

$$\hat{\mathcal{L}}^{(\alpha)}_n(x) = e^{-\frac{x}{2}}\mathcal{L}^{(\alpha)}_n(x), \quad x \in (0,\infty) \tag{3.18}$$

and, as can be deduced from (3.17), are orthogonal with respect to the weight function $\hat{w}_\alpha(x) = x^\alpha$. Considering the usual Laguerre functions obtained for $\alpha = 0$, which are used for the next developments, they form a sequence of orthogonal basis functions in $L^2(0,\infty)$ since

$$\int_0^\infty \hat{\mathcal{L}}_i(x)\hat{\mathcal{L}}_j(x)dx = \delta_{ij}, \quad \forall i,j \geq 0. \tag{3.19}$$

In contrast to the GLPs, the Laguerre functions are well behaved at infinity and, as already anticipated, they are suitable to represent decaying functions in semi-infinite domains due to the decay property

$$\|\hat{\mathcal{L}}_n(x)\| \to 0, \quad \text{as} \quad x \to \infty. \tag{3.20}$$

Moreover, the Galerkin approach based on the Laguerre functions leads to a stable discrete approximation of the weak problem (3.11) since the error remains limited in the usual $L^2(0,\infty)$ norm (see [68]).

3.1.3 Discrete problem formulation

To clarify the notation, in the following the test functions are named as $\mathcal{C}_i(\eta)$ while the trial functions with $\mathcal{C}_i^*(\eta)$. For the application described here, the Laguerre functions as defined in 3.1.2 will not be used directly as basis functions. Instead, the basis for the Galerkin-Laguerre approximation proposed in [68] will be considered that is more convenient from the implementation viewpoint. The test functions can be defined by the relations

$$\begin{aligned} &\mathcal{C}_1(\eta) = \eta e^{-\frac{\eta}{2}}, \\ &\mathcal{C}_i(\eta) = \hat{\mathcal{L}}_{i-2}(\eta) - 2\hat{\mathcal{L}}_{i-1}(\eta) + \hat{\mathcal{L}}_i(\eta), \quad i \geq 2. \end{aligned} \tag{3.21}$$

The functions $\mathcal{C}_i(\eta)$ defined above satisfy the boundary conditions (3.10) on the test function $v(\eta)$ and they span the finite-dimensional functional space

$$\mathcal{P}_{0,N} = \left\{ v : v = e^{-\frac{\eta}{2}} \eta p(\eta),\ p(\eta) \in \mathbb{P}_N(0,\infty) \right\}, \tag{3.22}$$

where $\mathbb{P}_N(0,\infty)$ is the space of polynomials of maximum degree N defined on the interval $[0,\infty)$. The functions $\mathcal{C}_i(\eta)$ are the same proposed in [68] for the Galerkin discretization of the biharmonic equation. It should be noted that, similarly to what has been shown for the Laguerre functions in 3.1.2, they have the property

$$\mathcal{C}_i(\eta) \to 0, \quad \text{as} \quad \eta \to \infty. \tag{3.23}$$

The trial functions must be chosen in order to represent the behaviour of the solution $\psi(\eta)$, their expression is shown below

$$\begin{aligned} &\mathcal{C}_1^*(\eta) = 1 - \left(1 + \frac{\eta}{2}\right) e^{-\frac{\eta}{2}}, \\ &\mathcal{C}_i^*(\eta) = \hat{\mathcal{L}}_{i-2}(\eta) - 2\hat{\mathcal{L}}_{i-1}(\eta) + \hat{\mathcal{L}}_i(\eta), \quad i \geq 2. \end{aligned} \tag{3.24}$$

They are equal to the test functions for $i \geq 2$ and span the finite dimensional space

$$\mathcal{K}_N = \left\{ v : v = \alpha \mathcal{C}_1^*(\eta) + e^{-\frac{\eta}{2}} \eta^2 p(\eta),\ \alpha \in \mathbb{R},\ p(\eta) \in \mathbb{P}_{N-1}(0,\infty) \right\}. \tag{3.25}$$

Therefore, the solution $\psi(\eta)$ can be written as a linear combination of the trial functions (3.24), namely

$$\psi(\eta) = \sum_{i=1}^{N} \psi_i \mathcal{C}_i^*(\eta). \tag{3.26}$$

The first trial function $\mathcal{C}_1^*(\eta)$ represents a modification of the Laguerre function basis. It should be noted that $\mathcal{C}_1^*(\eta)$ has the property

$$\mathcal{C}_1^*(\eta) \to 1, \quad \text{as} \quad \eta \to \infty, \tag{3.27}$$

which allows to properly represent the asymptotic behaviour of the solution $\psi(\eta)$. In fact, from the equation (3.26) can be written that

$$\lim_{\eta\to\infty} \psi(\eta) = \lim_{\eta\to\infty} \sum_{i=1}^{N} \psi_i \mathcal{C}_i^*(\eta) = \psi_1, \tag{3.28}$$

where the value ψ_1, associated with the modified function $\mathcal{C}_1^*(\eta)$, will be provided from the numerical solution of the problem. It should also be noted that by means of the expansion for the solution ψ (3.26), all the boundary conditions (3.7) are identically satisfied.
The discrete formulation of the problem can be obtained introducing the expression (3.26) in the weak variational form (3.11), since the weak formulation must be satisfied for all $v(\eta) = \mathcal{C}_i(\eta),\ i = 1, \dots N$, the discrete form of the problem corresponds to a non-linear system of equations that can be compactly written as

$$-T^* \boldsymbol{\psi} - \boldsymbol{nl}(\psi) + \left(-\frac{1}{2} A^* + \frac{1}{2} B^* \right) \boldsymbol{\psi} = \boldsymbol{r}. \tag{3.29}$$

In the equation above, the vector $\boldsymbol{\psi}$ has as components the unknown coefficients of the linear combination (3.26) ψ_i. The remaining terms are the discrete counterparts of the operators that appear in the weak formulation (3.11).

In particular, the elements of the matrices T^*, A^* and B^* are defined by

$$t^*_{ij} = \int_0^\infty \mathcal{C}'_i(\eta)\mathcal{C}^{*''}_j(\eta)d\eta, \quad i,j \geq 1, \tag{3.30}$$

$$a^*_{ij} = \int_0^\infty \left[\mathcal{C}_i(\eta)a(\eta)\right]'\mathcal{C}^{*'}_j(\eta)d\eta, \quad i,j \geq 1, \tag{3.31}$$

$$b^*_{ij} = \int_0^\infty \mathcal{C}_i(\eta)b(\eta)\mathcal{C}^{*}_j(\eta)d\eta, \quad i,j \geq 1, \tag{3.32}$$

while the vectors $\boldsymbol{nl}(\psi)$ and $\boldsymbol{r}$, which correspond to the non-linear terms and to the right-hand side of the weak form, respectively, are given by

$$nl_i(\psi) = \frac{1}{2}\int_0^\infty \left[\mathcal{C}'_i(\eta)\psi\psi' + \mathcal{C}_i(\eta)\left(\psi'\right)^2\right]d\eta, \tag{3.33}$$

$$r_i = \int_0^\infty \mathcal{C}_i(\eta)r(\eta)d\eta. \tag{3.34}$$

The non-linear system (3.29) is solved by means of the Newton-Raphson algorithm [35]. Defining the operator

$$\boldsymbol{N}(\psi) = \left(-T^* - \frac{1}{2}A^* + \frac{1}{2}B^*\right)\boldsymbol{\psi} - \boldsymbol{nl}(\psi) - \boldsymbol{r}, \tag{3.35}$$

the Newton algorithm requires the evaluation of the Jacobian matrix

$$\mathcal{J}(\psi) = \frac{\partial \boldsymbol{N}(\psi)}{\partial \boldsymbol{\psi}}, \tag{3.36}$$

whose elements are given by

$$\mathcal{J}_{ij}(\psi) = l^*_{ij} - \int_0^\infty \left\{\frac{1}{2}\mathcal{C}'_i(\eta)\left[\psi'(\eta)\mathcal{C}^*_j(\eta) + \psi(\eta)\mathcal{C}^{*'}_j(\eta)\right] + \mathcal{C}_i(\eta)\psi'(\eta)\mathcal{C}^{*'}_j(\eta)\right\}d\eta, \tag{3.37}$$

where $l^*_{ij} = -t^*_{ij} - \frac{1}{2}a^*_{ij} + \frac{1}{2}b^*_{ij}$.

Starting from an initial guess, the solution of the problem $\boldsymbol{\psi}$ is updated at each iteration of the algorithm as

$$\boldsymbol{\psi}_{k+1} = \boldsymbol{\psi}_k - [\mathcal{J}(\psi_k)]^{-1} \boldsymbol{N}(\psi_k), \tag{3.38}$$

until the norm of the iteration increment $\|\boldsymbol{\psi}_{k+1} - \boldsymbol{\psi}_k\|$ is below a certain tolerance value.
The explicit expressions for the matrix involved in the solver have not been reported here, the reader is referred to [4] where such matrices are computed in closed form. Moreover, it is important to mention that the accuracy of the solver can be improved by a scaling of the independent variable η. The resolution of the solver is basically given by the number of basis function that are considered for the linear combination (3.26). Nevertheless, as the number N is increased, the approximation accuracy mainly increases for large values of η which is useless since the solution ψ tends to a constant value. The main idea is to solve the equations for the new unknown $\hat{\psi}(\hat{\eta})$ where $\hat{\eta} = \frac{\eta}{\chi}$, that is the similarity variable scaled by a certain factor χ. Further details are not provided in this context for conciseness, but the general procedure described here is still valid (see [4]).

3.1.4 Orr-Sommerfeld equation numerical solution

The Galerkin-Laguerre approach can be used also for the numerical solution of the Orr-Sommerfeld equation (2.5), the same basic steps for the discretization of the Blasius problem are rapidly pursued also in this section. The Orr-Sommerfeld eigenvalue problem (2.5) can be written after some manipulations as

$$\begin{aligned} &\phi'''' - 2\alpha^2\phi'' + \alpha^4\phi + i\alpha Re\left\{-[U(\eta)\phi' - U'(\eta)\phi]' + \alpha^2 U(\eta)\phi\right\} \\ &= ic\alpha Re\left(-\phi'' + \alpha^2\phi\right). \end{aligned} \tag{3.39}$$

The hat symbol is omitted from all the variables to simplify the notation but they are non-dimensional as outlined in 2.1.1. In addition, η is used for the base functions and for the Blasius problem, but for the latter it should be interpreted as $\eta = \frac{y}{G(x_1)}$ since the equation is solved for the local boundary-layer profile at the inlet of the domain. The base flow $U(\eta)$ is provided by the numerical solution of the Blasius equation as

$$U(\eta) = f'(\eta) = \psi'(\eta) + 1 - e^{-\frac{\eta}{2}} + \frac{1}{2}\eta e^{-\frac{\eta}{2}}. \tag{3.40}$$

The boundary conditions for the eigenfunction ϕ are fully homogeneous, they are reported here for convenience,

$$\phi(0) = 0, \quad \phi'(0) = 0, \quad \phi(\infty) = 0, \quad \phi'(\infty) = 0. \tag{3.41}$$

Differently from the Blasius solution, the function ϕ decays at infinity, therefore the Laguerre spectral approximation can be applied directly without any change of variables. The weak formulation of the problem is obtained integrating by parts the inner product of the equation (3.39) with a test function $v(\eta)$ satisfying the boundary conditions

$$v(0) = 0, \quad v'(0) = 0. \tag{3.42}$$

Skipping the intermediate passages, the weak variational formulation of the problem reads:

$$\begin{aligned}
&\textit{find } \phi \in H_0^2(0,\infty) = \{u \in H^2(0,\infty), u(0) = u'(0) = 0\} \textit{ such that:} \\
&\int_0^\infty v''(\eta)\phi''d\eta + 2\alpha^2 \int_0^\infty v'(\eta)\phi' d\eta + \alpha^4 \int_0^\infty v(\eta)\phi d\eta \\
&+ i\alpha Re \int_0^\infty \left\{ v'(\eta) \left[U(\eta)\phi' - U'(\eta)\phi \right] + \alpha^2 v(\eta) U(\eta)\phi \right\} d\eta \\
&= ic\alpha Re \left(\int_0^\infty v'(\eta)\phi' d\eta + \alpha^2 \int_0^\infty v(\eta)\phi d\eta \right), \quad \forall v \in H_0^2(0,\infty).
\end{aligned} \tag{3.43}$$

The Laguerre basis functions, already used as test functions for the Blasius problem, are considered here to derive the discrete counterpart of the weak form (3.43). In particular, the test trial functions are identical and defined as

$$\mathcal{C}_i(\eta) = \mathcal{C}_i^*(\eta) = \hat{\mathcal{L}}_{i-2}(\eta) - 2\hat{\mathcal{L}}_{i-1}(\eta) + \hat{\mathcal{L}}_i(\eta), \quad i \geq 2. \tag{3.44}$$

With respect to the Blasius problem, the first test function $\mathcal{C}_1(\eta) = \eta e^{-\frac{\eta}{2}}$ has been discarded since it does not satisfy the homogeneous condition on the

first derivative at $\eta = 0$.
Therefore, the eigenfunction ϕ is expanded as

$$\phi(\eta) = \sum_{i=2}^{N} \phi_i \mathcal{C}_i(\eta), \tag{3.45}$$

and the weak form (3.43) must be satisfied for all $v(\eta) = \mathcal{C}_i(\eta), \quad i = 2, \dots N$.
The Galerkin-Laguerre method leads to the discrete eigenvalue problem

$$\left[D^4 + 2\alpha^2 D^2 + \alpha^4 M + i\alpha Re\left(N + \alpha^2 \mathcal{U}\right)\right] \boldsymbol{\phi} = ic\alpha Re\left(D^2 + \alpha^2 M\right) \boldsymbol{\phi}, \tag{3.46}$$

where the eigenvectors $\boldsymbol{\phi}$ have components ϕ_i. The matrices that appear in (3.46) correspond to the continuous operators in the weak form (3.43), their definition is reported below

$$m_{ij} = \int_0^\infty \mathcal{C}_i(\eta)\mathcal{C}_j(\eta)d\eta, \quad i, j \geq 2, \tag{3.47}$$

$$d^2_{ij} = \int_0^\infty \mathcal{C}'_i(\eta)\mathcal{C}'_j(\eta)d\eta, \quad i, j \geq 2, \tag{3.48}$$

$$d^4_{ij} = \int_0^\infty \mathcal{C}''_i(\eta)\mathcal{C}''_j(\eta)d\eta, \quad i, j \geq 2, \tag{3.49}$$

$$u_{ij} = \int_0^\infty \mathcal{C}_i(\eta)U(\eta)\mathcal{C}_j(\eta)d\eta, \quad i, j \geq 2, \tag{3.50}$$

$$n_{ij} = \int_0^\infty \mathcal{C}'_i(\eta)\left[U(\eta)\mathcal{C}'_j(\eta) - U'(\eta)\mathcal{C}_j(\eta)\right]d\eta, \quad i, j \geq 2. \tag{3.51}$$

The solution of the eigenvalue problem (3.46) is obtained by means of the routine ZGGEV implemented in the LAPACK. The routine computes the generalized eigenvalues and eigenvectors for a pair of complex nonsymmetric matrices (A, B), using the QZ algorithm. For the problem in exam the matrices A and B are given by

$$\begin{aligned} A(\alpha, Re) &= \left[D^4 + 2\alpha^2 D^2 + \alpha^4 M + i\alpha Re\left(N + \alpha^2 \mathcal{U}\right)\right], \\ B(\alpha, Re) &= i\alpha Re\left(D^2 + \alpha^2 M\right). \end{aligned} \tag{3.52}$$

Further details on LAPACK and on the QZ algorithm are not provided in this work, but an exhaustive documentation can be found in [1].

From the computational point of view, the primary stability analysis constitutes a low percentage of the total required computational time. However, the primary stability solution enters in the definition of the base flow as shown in Chapter 2, therefore, a certain accuracy must be guaranteed. The sufficient number of basis functions N can be chosen taking as reference the results provided in [4], where the same problems described here have been solved.

3.2 Navier-Stokes integration scheme

Several different numerical tools have been developed in the past for the solution of fluid mechanics problems. Concerning incompressible fluid flows, a classification of the possible methods, together with the theoretical background on which they are based, can be found in [17]. Among the alternatives, it is worth mentioning spectral elements methods, that have been widely used for large-scale 3D stability problems [14], but also finite elements methods and finite volume methods [63] which have received considerable attention from the scientific community. The choice of the numerical method is strongly influenced by the requirements of the particular application. For instance, spectral methods can retain high accuracy levels but they are limited to simple domains and their computational complexity is rather high. On the other end, finite volume methods are suitable for complex geometries but high-order schemes are expensive. For what concerns the secondary stability problem, a large amount of the total computational cost is due to the integration of the incompressible Navier-Stokes equation that is needed for both the definition of the base flow and the computation of the spectrum of the monodromy operator. As exposed in 1, this work aims at providing a convenient alternative tool for transition prediction with respect to the time-consuming direct numerical simulation (DNS), therefore, the main requirement on the solver is a low computational cost. The fastest solvers are those based on the finite difference discretization which can provide high-order schemes while maintaining a low computational complexity. This section illustrates the general ideas of a finite difference solver which relies on the direction splitting technique proposed by Douglas (see [18]). For more detailed informations on the solver and application examples, the reader is referred to [12] or [25].

3.2.1 Theoretical backgroung

The theoretical principles on which the solver is based will be described in this section. For convenience, a model Navier-Stokes problem is considered

as reported below, however, the numerical scheme is general and can be used for solving all the differential problems presented in Chapter 2, as will be briefly outlined in the following. Let us consider the unsteady, dimensionless incompressible Navier-Stokes equations solved in a domain $\Omega = (0,1)^3$:

$$\begin{cases} \frac{\partial \boldsymbol{u}}{\partial t} + (\boldsymbol{u} \cdot \nabla)\boldsymbol{u} - \frac{1}{Re}\nabla^2 \boldsymbol{u} + \nabla p = \boldsymbol{f}, \\ \nabla \cdot \boldsymbol{u} = 0, \\ \boldsymbol{u}|_{\partial\Omega} = \boldsymbol{a}, \\ \boldsymbol{u}|_{t=0} = \boldsymbol{u}_0, \end{cases} \tag{3.53}$$

where $\boldsymbol{f}$ represents a body force, $\boldsymbol{a}$ denotes the boundary data and $\boldsymbol{u}_0$ is the initial velocity field at $t = 0$.
The main difficulty that arises in numerically approximating the problem (3.53) is due to the elliptic character of the equations induced by the incompressibility constraint. In other words, after the problem (3.53) is discretized in time, the coupling between the velocity field and the pressure field makes the numerical computation highly expensive since, in practice, a full Navier-Stokes problem must be solved at each time step. For this reason, most time marching algorithms, the so called projection schemes, are based on decoupling the velocity and pressure equations. This techniques started with the seminal works of Chorin [13] and Teman [72], in which the velocity field is decomposed in a divergence-free part and a gradient. This procedure, known as the Helmholtz–Hodge decomposition, leads to a discretized version of the problem (3.53) that requires, at each time step, the solution of a vector-valued advection-diffusion equation for the velocity and the solution of a decoupled scalar Poisson equation for the pressure. Nowadays, most of the commonly used numerical methods represent an improvement of the original scheme proposed by Chorin and Temam but still rely on the fundamental idea of decomposing the velocity field. Among them, an important class of methods is constituted by the so called pressure-correction schemes [26]. These last are time-marching techniques where each time steps is divided in two sub-steps: in the first sub-step the pressure is treated as explicit or ignored while in the second sub-step a correction is applied to the pressure field based on the Helmholtz–Hodge decomposition of a provisional velocity field.
The great majority of the incremental pressure-correction schemes (see [26])

are discrete realizations of the following singular perturbation of (3.53):

$$\begin{cases} \frac{\partial \boldsymbol{u_\epsilon}}{\partial t} + (\boldsymbol{u_\epsilon} \cdot \nabla)\boldsymbol{u_\epsilon} - \frac{1}{Re}\nabla^2 \boldsymbol{u_\epsilon} + \nabla p_\epsilon = \boldsymbol{f}, \\ -\Delta t \nabla^2 \phi_\epsilon + \nabla \cdot \boldsymbol{u_\epsilon} = 0, \\ \Delta t \frac{\partial p_\epsilon}{\partial t} = \phi_\epsilon - \frac{\chi}{Re}\nabla \cdot \boldsymbol{u_\epsilon}, \\ \boldsymbol{u_\epsilon}|_{\partial\Omega} = \boldsymbol{a}, \\ \boldsymbol{u_\epsilon}|_{t=0} = \boldsymbol{u}_0, \\ \frac{\partial \phi_\epsilon}{\partial n}\big|_{\partial\Omega} = 0, \\ p_\epsilon|_{t=0} = p_0, \end{cases} \tag{3.54}$$

in which $\epsilon := \Delta t$ is the perturbation parameter while the parameter $\chi \in [0, 1]$ is user-dependent. The value $\chi = 0$ corresponds to the standard form of the incremental pressure-correction method while for $\chi = 1$ the method is written in the rotational form (see [74] for more details). More details regarding the pressure-correction schemes are provided in [26] where the discrete algorithms are also discussed. For what concerns this work, it is sufficient to remind an important property of (3.54), namely

$$\|\boldsymbol{u} - \boldsymbol{u_\epsilon}\|_{L^2} \leq c\Delta t^2, \quad \forall \chi \in [0, 1]. \tag{3.55}$$

In other words, the velocity field $\boldsymbol{u_\epsilon}$ is a second order approximation in the L^2-norm of the Navier-Stokes solution $\boldsymbol{u}$. The proof of this results is not addressed here, however it can be found in [28].
The singular perturbation problem (3.54) can be generalized in a convenient form that leads to the direction-splitting technique adopted in this work.

Let me consider the alternative perturbation of the problem (3.53):

$$\begin{cases} \frac{\partial \boldsymbol{u_\epsilon}}{\partial t} + (\boldsymbol{u_\epsilon} \cdot \nabla)\boldsymbol{u_\epsilon} - \frac{1}{Re}\nabla^2 \boldsymbol{u_\epsilon} + \nabla p_\epsilon = \boldsymbol{f}, \\ \Delta t A \phi_\epsilon + \nabla \cdot \boldsymbol{u_\epsilon} = 0, \\ \Delta t \frac{\partial p_\epsilon}{\partial t} = \phi_\epsilon - \frac{\chi}{Re}\nabla \cdot \boldsymbol{u_\epsilon}, \\ \boldsymbol{u_\epsilon}|_{\partial\Omega} = \boldsymbol{a}, \\ \boldsymbol{u_\epsilon}|_{t=0} = \boldsymbol{u}_0, \\ \frac{\partial \phi_\epsilon}{\partial n}\big|_{\partial\Omega} = 0, \\ p_\epsilon|_{t=0} = p_0, \end{cases} \tag{3.56}$$

that is equal to previous formulation apart from the substitution of the Laplacian operator with a different operator called A for approximating the pressure correction ϕ_ϵ. As shown in [27], the convergence properties of $\boldsymbol{u_\epsilon}$ and p_ϵ remain unaltered if the operator $A : D(A) \subset L^2_{\int=0}(\Omega) \to L^2_{\int=0}(\Omega)$, with $L^2_{\int=0} = \{q \in L^2(\Omega), \int_\Omega q = 0\}$, is such that:

$$\begin{aligned} &\text{the bilinear form} \quad a(p,q) := \int_\Omega pAq \quad \text{is symmetric,} \\ &\|\nabla q\|^2_{L^2} \leq a(q,q), \quad \forall q \in D(A). \end{aligned} \tag{3.57}$$

Obviously, the family of the projection methods is recovered if $A = -\nabla^2$ but, in general, the method belongs to a new different class and the idea of projecting the velocity onto the space of solenoidal vector fields is abandoned in this new formulation. The choice of the operator A and the domain $D(A)$ follows that proposed in [27] and [25], their expression is reported below

$$\begin{cases} A := \left(1 - \frac{\partial^2}{\partial x^2}\right)\left(1 - \frac{\partial^2}{\partial y^2}\right), \\ D(A) := \Big\{ p,\ (1 - \partial_{yy})p, Ap \in L^2(\Omega),\ p|_{y=0,1} = 0, \\ \qquad\qquad \partial_x \left((1 - \partial_{yy})p\right)\big|_{x=0,1} = 0 \Big\}, \end{cases} \tag{3.58}$$

for the two-dimensional case while

$$\begin{cases} A := \left(1 - \frac{\partial^2}{\partial x^2}\right)\left(1 - \frac{\partial^2}{\partial y^2}\right)\left(1 - \frac{\partial^2}{\partial z^2}\right), \\ D(A) := \big\{p,\ (1-\partial_{zz})p, (1-\partial_{yy})(1-\partial_{zz})p, Ap \in L^2(\Omega), p|_{z=0,1} = 0, \\ \qquad\qquad \partial_y\left((1-\partial_{zz})p\right)\big|_{y=0,1} = 0, \partial_x\left((1-\partial_{yy})((1-\partial_{zz})p\right)\big|_{x=0,1} = 0\big\}, \end{cases} \tag{3.59}$$

for the three-dimensional case.
The definition of the operator A given by the equations (3.58) or (3.59) satisfies the conditions (3.57) and ensures the stability and convergence of the method (see [25] for more information). Moreover, the operator A has the interesting property that finding the solution p of the problem $Ap = f$, with $f \in L^2(\Omega)$, reduces to the solution of a cascade of one-dimensional problems

$$\begin{aligned} &\psi - \partial_{xx}\psi = f, \quad \partial_x\psi|_{x=0,1} = 0, \\ &\phi - \partial_{yy}\phi = \psi, \quad \partial_y\phi|_{y=0,1} = 0, \\ &p - \partial_{zz}p = \phi, \quad \partial_z p|_{z=0,1} = 0. \end{aligned} \tag{3.60}$$

As a matter of fact, considering the family of projection methods, the computational cost for the solution of the Poisson equation, that provides the pressure correction ϕ_ϵ, becomes dominant at large Reynolds number or when the size of the problem is very large. The generalized pressure correction scheme (3.56) with the operator A defined above has the advantage of maintaining the same second order accuracy of the projection method (3.54), but significantly reducing the computational cost. Indeed, the property (3.60) can be applied to the second equation of (3.56) to calculate ϕ_ϵ in a very efficient way, as will be shown in the next section. Another important topic that has to be mentioned is the numerical instability issue. The majority of the numerical methods for the Navier-Stokes equations must satisfy the so called LBB condition (see [9]). In simple words, only certain discretizations of the velocity field and of the pressure field are compatible with each other and permit the method to converge to the exact numerical solution. If an incompatible discretization is adopted, the numerical solution will be disturbed by spurious pressure modes or velocity modes. For finite difference solvers this difficulty is often bypassed using staggered grids, so that the three velocity components and the pressure field are computed on four different grids. Obviously, the use of staggered

grids increases the algorithmic complexity of the method and typically it influences negatively the computational cost. The use of co-located grids does not satisfy the LBB condition, therefore it is quite inconvenient in practice since requires additional tools to eliminate the spurious pressure modes from the solution (see, e.g., [81]). Nevertheless, the numerical method described in this section, which consists of a discretized version of (3.56), uses a single grid for all the variables. This fact is due to the properties of the operator A, in particular to the fact that his kernel is void, which ensures that no spurious modes are generated during the penalty step (when the pressure correction is computed). For a numerical confirmation of this result, together with further informations, the reader is again referred to [12].

3.2.2 Numerical algorithm

As anticipated, the numerical algorithm is formulated from the discretization of problem (3.56) in space and time. For the present application, the Crank-Nicolson scheme is adopted and the leap frog strategy for the pressure in order to evolve the solution in time, however, this choice is not strictly required. Different alternative time schemes have been used for the present direction splitting method (see [12], [25]) that can also allow a larger time step with respect to the Courant-Friedrichs-Lewy stability condition.
Denoting two subsequent time steps for the velocity $\boldsymbol{u}$ with the apices n and $n+1$, the time-discretized version of the problem (3.56) can be written as

$$\begin{cases} \frac{\boldsymbol{u}^{n+1}-\boldsymbol{u}^{n}}{\Delta t} - \frac{1}{2Re}\nabla^2\left(\boldsymbol{u}^{n+1}+\boldsymbol{u}^{n}\right) = \boldsymbol{f}^{n+1/2} - \nabla p^{*,n+1/2} - \boldsymbol{nl}(\boldsymbol{u}^{*,n+1/2}), \\ A\phi^{n+1/2} = -\frac{1}{\Delta t}\nabla\cdot\boldsymbol{u}^{n+1}, \\ p^{n+1/2} = p^{n-1/2} + \phi^{n+1/2} - \frac{\chi}{2Re}\nabla\cdot\left(\boldsymbol{u}^{n+1}+\boldsymbol{u}^{n}\right), \end{cases} \tag{3.61}$$

where the subscript $n+1/2$ indicates the intermediate time step between n and $n+1$ at which the right-hand side of the first equation is computed. The term $p^{*,n+1/2}$ represents a pressure predictor evaluated from the previous iterations of the algorithm. Therefore, the idea of decoupling the velocity field and the pressure field is still present in this generalized pressure correction scheme. In fact, in the first equation of (3.61), which allows one to compute the evolution of the velocity field, the pressure enters only as a known term at the right-hand side. The non-linear contribution, named $\boldsymbol{nl}$ in equation (3.61), is dealt with in an explicit manner as it is commonly done for the numerical

solution of unsteady flows. The known quantity $\boldsymbol{u}^{*,n+1/2} = (3\boldsymbol{u}^n - \boldsymbol{u}^{n-1})/2$ is a second order extrapolation of the velocity and can be computed from the solution at the previous time steps. The complete expression for the non-linear term along with some additional considerations will be provided at the end of the section, for the moment it is left generically denoted $\boldsymbol{nl}$ for simplicity. As a matter of fact, the nonlinearity does not interfere with the incompressibility constraint, this basically means that all the theoretical concepts recalled in 3.2.1 remain valid even if the linearized Navier-Stokes equations (2.25) are considered. Therefore, if the term $\boldsymbol{nl}(\boldsymbol{u}^{*,n+1/2})$ is substituted with the time-discrete expression $(\boldsymbol{U_2}^{n+1/2} \cdot \nabla)\boldsymbol{u}^{*,n+1/2} + (\boldsymbol{u}^{*,n+1/2} \cdot \nabla)\boldsymbol{U_2}^{n+1/2}$, the numerical algorithm that is presented in this section can also be used for the equation of the secondary stability theory.
The algorithm is initialized by setting $p^{*,1/2} = p_0$ for the first time step. Then, for all $n > 0$, the pressure predictor is defined as

$$p^{*,n+1/2} = p^{*,n-1/2} + \phi^{n-1/2}. \tag{3.62}$$

The velocity field is updated by solving the momentum equation, this is done by exploiting the direction splitting technique proposed by Douglas [18]. The velocity update step of the algorithm reduces to solving the following series of one dimensional problems:

$$\begin{cases} \frac{\boldsymbol{\xi}^{n+1} - \boldsymbol{u}^n}{\Delta t} = \frac{1}{Re}\nabla^2 \boldsymbol{u}^n + \boldsymbol{f}^{n+1/2} - \nabla p^{*,n+1/2} - \boldsymbol{nl}(\boldsymbol{u}^{*,n+1/2}), \\ \frac{\boldsymbol{\eta}^{n+1} - \boldsymbol{\xi}^{n+1}}{\Delta t} - \frac{1}{2Re}\frac{\partial^2}{\partial x^2}\left(\boldsymbol{\eta}^{n+1} - \boldsymbol{u}^n\right) = 0, \\ \frac{\boldsymbol{\zeta}^{n+1} - \boldsymbol{\eta}^{n+1}}{\Delta t} - \frac{1}{2Re}\frac{\partial^2}{\partial y^2}\left(\boldsymbol{\zeta}^{n+1} - \boldsymbol{u}^n\right) = 0, \\ \frac{\boldsymbol{u}^{n+1} - \boldsymbol{\zeta}^{n+1}}{\Delta t} - \frac{1}{2Re}\frac{\partial^2}{\partial z^2}\left(\boldsymbol{u}^{n+1} - \boldsymbol{u}^n\right) = 0. \end{cases} \tag{3.63}$$

As already mentioned, the spatial discretization of the equations is based on the finite difference. In particular, the second-order central finite-difference scheme is used to approximate the derivatives of the unknowns and, for the second derivatives specifically, it provides the discrete approximation

$$f''(x_i) \approx \frac{f_{i+1} - 2f_i + f_{i-1}}{\Delta x^2}. \tag{3.64}$$

For the implementation of the algorithm, the problem (3.63) can be refor-

mulated in a different form to improve the efficiency of the computation, namely

$$\begin{cases} \big(\boldsymbol{\eta}^{n+1} - \boldsymbol{u}^n\big) - \frac{\Delta t}{2Re}\frac{\partial^2}{\partial x^2}\big(\boldsymbol{\eta}^{n+1} - \boldsymbol{u}^n\big) = \Delta t\big(\boldsymbol{f}^{n+1/2} - \nabla p^{*,n+1/2} - \boldsymbol{nl}(\boldsymbol{u}^{*,n+1/2})\big), \\ \big(\boldsymbol{\xi}^{n+1} - \boldsymbol{u}^n\big) - \frac{\Delta t}{2Re}\frac{\partial^2}{\partial y^2}\big(\boldsymbol{\xi}^{n+1} - \boldsymbol{u}^n\big) = \big(\boldsymbol{\eta}^{n+1} - \boldsymbol{u}^n\big), \\ \big(\boldsymbol{u}^{n+1} - \boldsymbol{u}^n\big) - \frac{\Delta t}{2Re}\frac{\partial^2}{\partial z^2}\big(\boldsymbol{u}^{n+1} - \boldsymbol{u}^n\big) = \big(\boldsymbol{\xi}^{n+1} - \boldsymbol{u}^n\big). \end{cases} \tag{3.65}$$

It can be easily seen that the expressions (3.65), after being discretized in space by means of the scheme (3.64), correspond to a set of tridiagonal linear systems which can be solved sequentially.
The third step of the algorithm consist in solving the equation

$$A\phi^{n+1/2} = -\frac{1}{\Delta t}\nabla \cdot \boldsymbol{u}^{n+1}, \tag{3.66}$$

which provides the pressure correction $\phi^{n+1/2}$. The term at the right-hand side is known from the previous step of the algorithm, therefore the property (3.60) can be exploited to split the equation (3.66) as follows

$$\begin{cases} \psi - \frac{\partial^2 \psi}{\partial x^2} = -\frac{1}{\Delta t}\nabla \cdot \boldsymbol{u}^{n+1}, & \frac{\partial \psi}{\partial x}\big|_{x=0,1} = 0, \\ \varphi - \frac{\partial^2 \varphi}{\partial y^2} = \psi, & \frac{\partial \varphi}{\partial y}\big|_{y=0,1} = 0, \\ \phi^{n+1/2} - \frac{\partial^2 \phi^{n+1/2}}{\partial z^2} = \varphi, & \frac{\partial \phi^{n+1}}{\partial z}\big|_{z=0,1} = 0. \end{cases} \tag{3.67}$$

Identically to what stated for the velocity update, the calculation of $\phi^{n+1/2}$ also requires the solution of tridiagonal linear systems only.
Finally, the pressure is updated through the last equation of (3.61) as

$$p^{n+1/2} = p^{n-1/2} + \phi^{n+1/2} - \frac{\chi}{Re}\nabla \cdot \left(\frac{1}{2}\big(\boldsymbol{u}^{n+1} + \boldsymbol{u}^n\big)\right). \tag{3.68}$$

The core of the algorithm consists in solving tridiagonal linear systems, this is achieved by means of the Thomas algorithm which basically represents a simplified form of the Gauss elimination for tridiagonal linear systems (see

[16]). In addition, the matrices of the system are constant in time and can be factored only once at the beginning of the computation.
Before proceeding with the description of the implicitly restarted Arnoldi method, some concepts need to be clarified. Firstly, it is necessary to provide an expression for the non-linear term that, until this point, has been left unspecified. In general, for the incompressible Navier-Stokes equations, the non-linear term can be written in several forms (see [24]) which basically differ by a term multiplied by the divergence of the velocity. The important point is that all of these forms are equivalent in the continuum due to the incompressibility constraint, but can have a different behaviour when integrated in discrete approximation of the equations. With respect to the method described here, it can be easily noted from the last two equations of (3.61) that when an unsteady flow is considered (that is the case for the problem in exam), the velocity is only approximately divergence-free. This fact means that the different formulations of the non-linear term, once discretized, are not equivalent. A comparison between the effects of different expressions for the non-linear term can be found in [80], the choice of which one to adopt can be led by the required accuracy on the solution, the resultant algorithmic complexity and so on. However, the chosen formulation has to guarantee the conservation of kinetic energy in order to obtain a stable behaviour of the algorithm. The expression for the chosen discrete non-linear term is shown below in the three-dimensional case:

$$
\begin{aligned}
&(\boldsymbol{u}\cdot\nabla)\,u_l\big|_{x_i,y_j,z_k} \approx \\
&\frac{1}{4\Delta x}\big[u_l(x_{i+1},y_j,z_k)\big(u(x_{i+1},y_j,z_k)+u(x_i,y_j,z_k)\big)- \\
&u_l(x_{i-1},y_j,z_k)\big(u(x_{i-1},y_j,z_k)+u(x_i,y_j,z_k)\big)\big]+ \\
&\frac{1}{4\Delta y}\big[u_l(x_i,y_{j+1},z_k)\big(v(x_i,y_{j+1},z_k)+v(x_i,y_j,z_k)\big)- \\
&u_l(x_i,y_{j-1},z_k)\big(v(x_i,y_{j-1},z_k)+v(x_i,y_j,z_k)\big)\big]+ \\
&\frac{1}{4\Delta z}\big[u_l(x_i,y_j,z_{k+1})\big(w(x_i,y_j,z_{k+1})+w(x_i,y_j,z_k)\big)- \\
&u_l(x_i,y_j,z_{k-1})\big(w(x_i,y_j,z_{k-1})+w(x_i,y_j,z_k)\big)\big].
\end{aligned}
\tag{3.69}
$$

The expression (3.69) derives directly from the conservative weak formulation of the Navier-Stokes equations and, as shown numerically in [12] where the present direction splitting algorithm has been proposed and tested on many

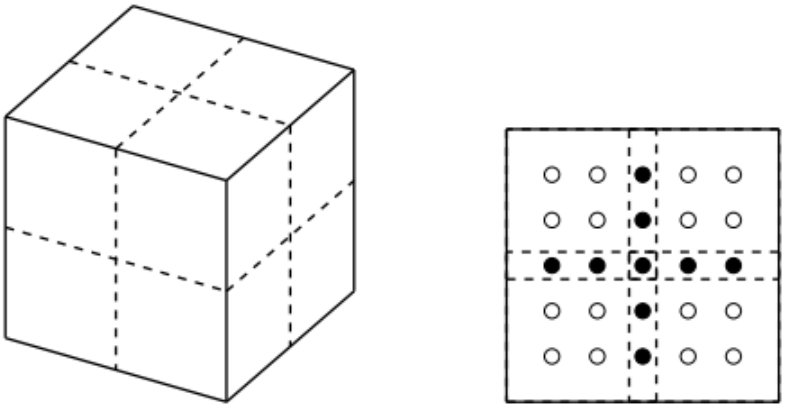

Figure 3.1 *Figure taken from [12]. Block decomposition of the computational domain.*

model problems, it leads to numerically stable solutions in time.
At last, it is important to outline that the problems (3.65) and (3.67), which basically determine the whole cost of the algorithm, can be efficiently parallelized. This is done trough the Schur complement method [82] which has been shown to provide a significant increase in the computational performance for the solution of large-scale systems [38]. It is based on a decomposition of the computational domain in non-overlapping blocks (see figure 3.1) so that each block is assigned to a different processor. The grid points can be classified in internal points, that corresponds to the white circles in figure 3.1, and the interface points shared between different processors. In order to explain the general ideas, let us consider a sample problem $Ax = b$ that could represents one tridiagonal system of (3.65) or (3.67) for a certain spatial direction. Without loss of generality, it is assumed that the solution is divided among two processors so that x_1 and x_2 are associated with the internal points while x_Γ is the solution at the interface. Due to the tridiagonality of the original system and the property of the finite-difference discretization, the model problem $Ax = b$ assumes the form

$$\begin{bmatrix} A_{11} & 0 & A_{1\Gamma} \\ 0 & A_{22} & A_{2\Gamma} \\ A_{\Gamma 1} & A_{\Gamma 2} & A_{\Gamma\Gamma} \end{bmatrix} \begin{bmatrix} x_1 \\ x_2 \\ x_\Gamma \end{bmatrix} = \begin{bmatrix} b_1 \\ b_2 \\ b_\Gamma \end{bmatrix}. \tag{3.70}$$

The basic idea of the Schur complement method is to eliminate the internal unknowns manipulating the original linear system as

$$(A_{\Gamma\Gamma} - A_{\Gamma 1}A_{11}^{-1}A_{1\Gamma} - A_{\Gamma 2}A_{22}^{-1}A_{2\Gamma})x_\Gamma = b_\Gamma - A_{\Gamma 1}A_{11}^{-1}b_1 - A_{\Gamma 2}A_{22}^{-1}b_2, \quad (3.71)$$

and to solve for the interface variable first. The matrix of the system (3.71), called Schur-complement matrix, has dimensions typically much lower than the original matrix of the system and, in addition, it is also tridiagonal when the linear system to be solved is tridiagonal. After the interface unknowns have been computed, the internal unknowns are recovered solving the systems

$$A_{11}x_1 = b_1 - A_{1\Gamma}x_\Gamma, \quad A_{22}x_2 = b_2 - A_{2\Gamma}x_\Gamma. \quad (3.72)$$

However, since the equations are decoupled, this can be done in parallel such that each processor computes its own internal unknowns. Basically the communication between different processors, implemented for the present case through the message passing interface MPI, is needed only when assembling the right-hand side of (3.71). Instead, the Schur complement matrix

$$\Sigma = A_{\Gamma\Gamma} - \sum_{n=1}^{N_p} A_{\Gamma n}A_{nn}^{-1}A_{n\Gamma}, \quad (3.73)$$

where N_p is the number of processors involved, can be factored and stored in each processor at the preprocessing stage so that the interface system (3.71), once assembled the right-hand side, can be solve without the need of communication between different processors. When considering the case of more than one spatial direction, the implementation of the Schur complements requires same additional technicalities that are not exposed here for conciseness. However, the main features of limiting at a minimum the required communication between different processors and solving independently on each processor for the internal unknowns still remain valid. The reader is referred to [12] for the detailed implementation.

3.3 Implicitly Restarted Arnoldi Method

In this section the main features of the Implicitly Restarted Arnoldi Method (IRAM) are illustrated, one of the most used, efficient algorithms to compute eigenvalues of large-size matrices. The IRAM belongs to the family of iterative methods which have been developed as an attempt to reduce the typical computational cost of $O(n^3)$ operations, where n is the dimension of the matrix, required by the so-called direct or non-iterative methods (e.g the QR algorithm [76], [16]). As a matter of fact, for modern applications involving huge matrices, direct methods are impractical. Considering specifically the secondary stability analysis, where the monodromy operator (defined in chapter 2.2.1) is not even known explicitly, the iterative methods are also mandatory. In fact, as already anticipated, in the Arnoldi method and in iterative algorithms, the matrix can be represented as a black box, such that:

$$\boldsymbol{x} \longrightarrow \boxed{\text{BLACK BOX}} \longrightarrow A\boldsymbol{x}.$$

More detailed information on this idea will be provided later on since it is fundamental for the solution of the problem in exam.
The Implicitly Restarted Arnoldi Method has been proposed by Sorensen and Lehoucq in [39] and then implemented in the software package ARPACK [40].
Before describing the actual IRAM algorithm, it is useful to outline the general idea of the method that is strictly related to the concept of Krylov subspace. Given a matrix $A \in \mathbb{C}^{n\times n}$ and a vector $v_0 \in \mathbb{C}^n$, the subspace

$$\mathcal{K}_k(A, v_0) = Span\left\{v_0, Av_0, A^2v_0, \ldots, A^{k-1}v_0\right\} \subseteq \mathbb{C}^n, \tag{3.74}$$

is called the k^{th} Krylov subspace corresponding by A and v_0. It should be noted that the vectors which form the base of $\mathcal{K}_k$ are those generated by successive iterations of the power method (see [16]). Without going into the details, the power method exploits the fact that the term A^kv_0 tends to the eigenvector corresponding to the dominant eigenvalue for increasing values of k, and under suitable hypothesis. However, the whole sequence of vectors of the power method, that in the typical implementation of the algorithm are not retained in memory, can provide informations on the spectrum of the matrix A. The numerical methods for eigenvalue computation which take advantage of the power method sequence are usually called Krylov-subspace

or projection methods. These methods construct approximate eigenpairs in the subspace $\mathcal{K}_k(A, v_0)$, imposing the Galerkin condition:

$$v^T (Ax - \lambda x) = 0, \quad \forall v \in \mathcal{K}_k(A, v_0). \tag{3.75}$$

The vector $x \in \mathcal{K}_k(A, v_0)$ and the corresponding value $\lambda \in \mathbb{C}$ which satisfy the condition (3.75) are called Ritz vector and Ritz value, respectively, and they basically fulfill the usual eigenvalue-eigenvector relation but projected onto the smaller space $\mathcal{K}_k(A, v_0)$.
At this point, it can be introduced the fundamental tool of the numerical method, that is the Arnoldi factorization. It is defined as the k-step Arnoldi factorization of $A \in \mathcal{C}^{n\times n}$ a relation of the form

$$AV_k = V_k H_k + f_k e_k^T, \tag{3.76}$$

where the matrix $V_k \in \mathcal{C}^{n\times k}$ has orthonormal columns, $H \in \mathcal{C}^{k\times k}$ is an upper Hessemberg matrix and the vector $f \in \mathcal{C}^n$ is such that $V_k^H f_k = 0$. The corresponding algorithm that defines the terms in (3.76) is shown below, the link between the Arnoldi factorization and the problem (3.75) will be clarified in the subsequent developments.

Algorithm 1 k-step Arnoldi factorization

$v_1 =$ arbitrary vector,
$v_1 \leftarrow v_1/\|v_1\|, \quad w = Av_1, \quad \alpha_1 = v_1^H w;$
$f_1 \leftarrow w - v_1\alpha_1, \quad V_1 \leftarrow (v_1), \quad H_1 \leftarrow (\alpha_1);$
for $j = 1, 2, 3, \ldots k-1$ **do**
  $\beta_j = \|f_j\|, \quad v_{j+1} \leftarrow f_j/\beta_j;$
  $V_{j+1} \leftarrow (V_j, v_{j+1}), \quad \hat{H}_j \leftarrow \begin{pmatrix} H_j \\ \beta_j e_j^T \end{pmatrix};$
  $w \leftarrow Av_{j+1};$
  $h \leftarrow V_{j+1}^H w, \quad f_{j+1} \leftarrow w - V_{j+1}h;$
  $H_{j+1} \leftarrow (\hat{H}_j, h);$
end for

The algorithm 1 presents a strong analogy with the Gram-Schmidt algorithm (see [76]). The latter creates an orthonormal basis for the space generated by the columns of a matrix A while the Arnoldi factorization creates an orthonormal basis for the Krylov subspace $\mathcal{K}_k(A, v_1)$. The vectors of this basis, called Arnoldi vectors, are generated from the power method sequence and constitute the columns of the matrix V_k. In mathematical form:

$$\mathcal{K}_k(A, v_1) = Span\left\{\mathrm{Col}_1(V_k), \mathrm{Col}_2(V_k), \ldots, \mathrm{Col}_k(V_k)\right\}. \tag{3.77}$$

The matrix H_k can be viewed as the orthogonal projection of A onto $\mathcal{K}_k(A, v_1)$ with the Arnoldi vectors as an orthogonal basis. It should be noted that the relation

$$H_k = V_k^H A V_k, \tag{3.78}$$

can be easily obtained from equation (3.76), therefore, the Hessemberg matrix H_k is expected to contain important informations also on the spectrum of the matrix A.
Before going into further details, it should be clarified how the Arnoldi factorization of the monodromy operator is practically computed in this work. As already anticipated, the action of the monodromy operator corresponds to the evolution of the three-dimensional disturbance, according with the equations (2.33), a period of the TS wave forward in time. However, the Navier-Stokes equations have been discretized in space by means of finite differences so that the perturbation field is computed in a finite number of points of the domain. If we call $n/4$ the total number of points, the disturbance can be represented by a vector of dimension n which collects the values assumed by the three velocity components and by the pressure field on those points. Looking at the Arnoldi factorization procedure, the first Arnoldi vector v_1 is typically generated randomly when computing eigenvalues and can be interpreted as

$$v_1 = \left\{\begin{array}{c} \boldsymbol{u}_0 \\ \hline \boldsymbol{v}_0 \\ \hline \boldsymbol{w}_0 \\ \hline \boldsymbol{p}_0 \end{array}\right\}, \tag{3.79}$$

namely, it corresponds to a three dimensional perturbation. When the Arnoldi

method requires the computation of $w = Av_1$, the vector v_1 is passed to the Navier-Stokes solver described in Section 3.2 that performs a number i of steps, such that $i\Delta t = T$, starting from the initial condition (3.79). After that, the evolution of the disturbance is computed, the latter is reordered in a vector in the same way of (3.79) and sent back to the Arnoldi algorithm which computes the second Arnoldi vector v_2. This procedure is then repeated until the k-step Arnoldi factorization is completed. It can be easily guessed that the large size of the problem makes the direct eigenvalue algorithms too expensive. Nevertheless, the spectrum of the matrix $H_k \in \mathcal{C}^{k\times k}$ can be computed by the standard QR algorithm instead, as long as the Krylov-subspace dimension is such that $k \ll n$.
Let us consider an eigenvector y and the associated eigenvalue θ of the matrix H_k. Then, directly from the equation (3.76), the vector $x = V_k y$ satisfies the following relation

$$\|AV_k y - V_k H_k y\| = \|Ax - x\theta\| = \|f_k\||e_k^T y|. \tag{3.80}$$

In addition, since the residual vector f_k satisfies $V_k^H f_k = 0$, it can be shown that the Ritz pairs which solve the projected eigenvalue problem (3.75) are those of the form (x, θ). The term at the right-hand side $\|f_k\||e_k^T y|$ is called Ritz estimate of the pair (x, θ) and describes the quality of the approximation for the eigenpair of the matrix A. In particular, if $\|f_k\| = 0$ the Krylov subspace $\mathcal{K}_k(A, v_1)$ is an invariant subspace of A and the eigenvalues of the matrix H_k represent exactly a subset of those of A.
The algorithm described up to this point is the classical Arnoldi method [3] that permits to estimate a subset of k eigenvalues of the matrix A. In practical implementations of the method, typically the norm of the residual vector $\|f_k\|$ does not become small but still, increasing the Krylov subspace dimension k, some of the eigenvalues of H_k tend to approximate the eigenvalues of A well even for $k \ll n$ (the reader is referred to [16] for more informations). In the secondary stability analysis context, particular attention is given to the eigenvalues of largest module since, as already explained in Chapter 2, they basically determine if the flow is stable or not. However, the theory does not provide an estimate for the required number of iterations k necessary to approximate the eigenvalues of interest. Moreover, it should be considered that as k increases also an increasing number of Arnoldi vectors must be retained in memory and in addition to this, the cost for the calculation of the eigenvalues of H_k can become considerable. For these reasons, the Implicitly Restarted Arnoldi method was developed with the idea of progressively filtering the unwanted informations from a fixed dimension Krylov subspace. The method

exploits the following result:

$$f_k = 0 \iff v_1 = \sum_{j=1}^{k} \boldsymbol{x}_j \gamma_j, \text{ where } A\boldsymbol{x}_j = \boldsymbol{x}_j \lambda_j. \tag{3.81}$$

In words, if the starting vector v_1 can be written as a linear combination of k independent eigenvectors of A, then, the k^{th} residual vector of the Arnoldi factorization will vanish and as a consequence $\sigma(H_k) = \{\lambda_1, \lambda_2, \ldots, \lambda_k\}$. It should be noted that the algorithm 1 produces a factorization totally dependent on the choice of the starting vector v_1, thought, the theorem (3.81) states that the best possible v_1 would be one that lies in the invariant subspace associated to the wanted eigenvalues. Consequently, the implicitly restarting strategy consists in updating the starting vector v_1 and the related terms for the factorization (3.76) but without recomputing the whole Arnoldi factorization explicitly. In the IRAM this is achieved by means of p shifted QR factorization steps performed on the Hessemberg matrix H_k.
The IRAM algorithm in shown below.

Algorithm 2 Implicitly Restarted Arnoldi Method

Input: m-step Arnoldi factorization $AV_m = V_m H_m + f_m e_m^T$;
for $l = 1, 2, \ldots$ until $\|Ax_i - \lambda_i x_i\| < \tau \ \forall i = 1, \ldots, k$
Compute $\sigma(H_m)$ and select p shifts $\mu_1, \mu_2, \ldots, \mu_p$;
$Q = I_m$;
for $j = 1, 2, \ldots, p$ **do**
    Factor $H_m - \mu_j I = Q_j R_j$;
    $H_m \leftarrow Q_j^H H_m Q_j$; $Q \leftarrow QQ_j$;
end for
$\hat{\beta}_k = H_m(k+1, k)$; $\sigma_k = Q(m, k)$ with $k = m - p$;
$f_k \leftarrow v_{k+1}\hat{\beta}_k + f_m \sigma_k$;
$V_k \leftarrow V_m Q(:, 1:k)$; $H_k \leftarrow H_m(1:k, 1:k)$;
Extend the k-step factorization $AV_k = V_k H_k + f_k e_k^T$ to a new m-step Arnoldi factorization $AV_m = V_m H_m + f_m e_m^T$;
end for

It can be shown that at each iteration of the algorithm 2 the starting vector for the m-step Arnoldi factorization is implicitly updated as follows

$$v_1 \leftarrow \prod_{j=1}^{p}(A - \mu_j)v_1. \tag{3.82}$$

The shift values μ_j represent the unwanted information from the spectrum of A. In other words, if one is interested in the eigenvalues of largest module, as in this case, a simple way to select the shifts is to take the p eigenvalues of H_m with lowest module. This method is known as the Exact Shifts Strategy although other methods are possible (see [39]). It can be proven (see [40]) that the cyclic update of v_1 given by the relation (3.82) has the effect of filtering the starting vector so that the components of v_1 in the directions of the unwanted eigenvectors become less and less significant. Consequently, as the iterations advance, the starting vector is forced to be a linear combination of the wanted eigenvectors. The convergence of the algorithm is evaluated considering the Ritz estimates of the eigenpairs of H_k, not by checking the usual eigenvalue-eigenvector relation which is expensive from the computational point of view.
The Implicitly Restarted Arnoldi method allows one to approximate a specific subset of k eigenvalues of A very efficiently using $2kn + O(k^2)$ storage. The procedure explained in this section is valid when an exact arithmetic is considered. However, the round-off error inevitably generated in finite precision arithmetics leads to further complications. For instance, a typical problem that has to be taken into account, is the loss of orthogonality between subsequently generated Arnoldi vectors that can produce spurious copies of the approximated eigenvalues. The implementation details of the method in the software ARPACK are not addressed here for conciseness. The reader is referred to [40] where an extensive documentation can be found.

3.4 Numerical setup

This section concerns the choice of the numerical parameters for the secondary stability simulations and the rational process behind it. The computational cases which have been investigated are exposed at the end of the section along with the introduction of physical quantities needed to compare the present study with the experimental data available in the literature.
As can be seen in (2.33), the equations for the three-dimensional disturbances depend on the Reynolds number, the TS wave amplitude A and the spanwise wavenumber β, i.e. the physical parameters of the problem in exam. However, when the equations are discretized numerically, the monodromy operator can be written as

$$MO = MO(Re, \beta, A, x_j, y_j, x_{MAX}, y_{MAX}, \Delta t), \tag{3.83}$$

which shows explicitly the dependency of the eigenvalue problem on the computational grid, the domain dimension and the timestep. A convergence analysis is performed on the numerical variables for a fixed set of Re, β and A in order to verify the reliability of the numerical approximation. Considering at first the computational domain for a certain grid size and time step, the domain size is progressively enlarged until the results become almost independent from the current domain dimension. The same procedure is then repeated for the grid size and finally for the time step varying always one variable at a time. The convergence criterium is chosen to be the variation of the most unstable eigenvalue between the different simulations.
For the stability analysis of open flows, the domain size is critical to obtain accurate results. Looking at the problem in exam, the TS waves are expected to decay downstream, beyond the second branch of the neutral stability curve as stated by the primary stability theory. Similarly, in the linear framework, the secondary modes may grow but are also expected to decay downstream where the vital vorticity concentration of the primary wave is absent (see [31] for more informations).

Re_1	β	A
460	0.218	0.01

Table 3.1 *Fixed physical parameters adopted for the choice of the numerical setup.*

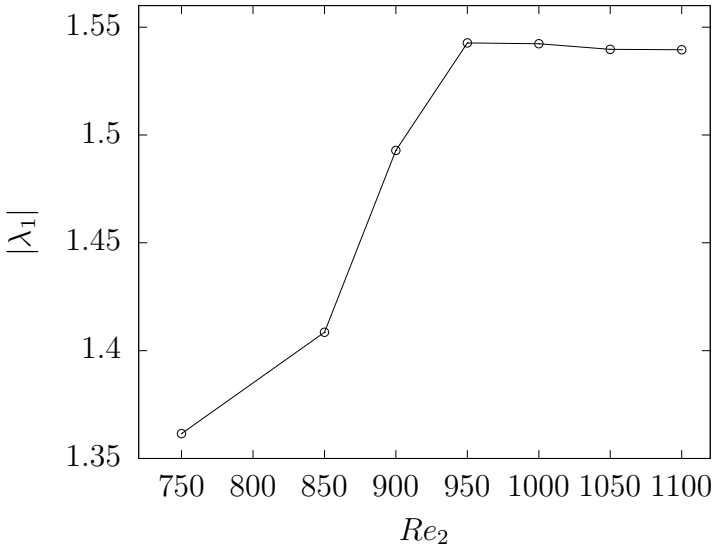

Figure 3.2 *Behaviour of the most unstable eigenvalue with respect to the position of the (artificial) outlet boundary.*

As stated in [5], for this kind of problems the convergence with respect to the longitudinal domain size is reached in practice when the disturbances have negligible amplitude at the outer face of the domain. The results for the influence of the domain size on the eigenvalues are shown in figure 3.2 while the fixed simulation parameters used are reported in table 3.1.
The variation of the eigenvalue became less than the one per cent when the domain extends up to $Re_2 = 1000$ allowing for a sufficient decay of the primary wave. Following the guidelines in [83] and [21], the vertical dimension of the domain has been chosen to be $25\delta_1$ where δ_1 is the displacement thickness at the inlet section. This relatively large vertical dimension is needed for the homogeneous conditions far from the wall to be accurate due to the slow decay of the TS waves in the wall-normal direction.

y_{MAX}/δ_1	$\lvert\lambda_1\rvert$	$\lvert\lambda_2\rvert$
15	1.612	1.531
20	1.562	1.502
25	1.542	1.490
30	1.532	1.484

Table 3.2 *Sensitivity analysis with respect to the vertical domain size.*

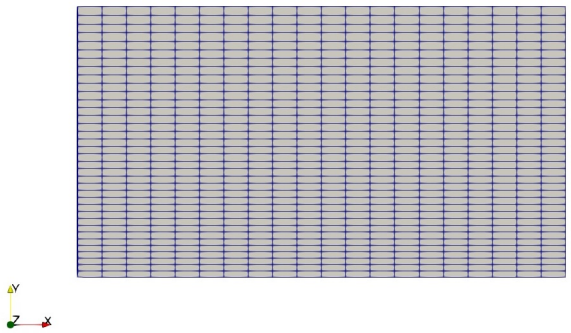

Figure 3.3 *Visualization of a part of the computational grid.*

A sensitivity analysis has also been performed on the vertical size of the domain and it shows, as can be seen in table 3.2, a rather weak dependency of the results on the vertical size when the latter is at least $15\delta_1$.
The computational grid is uniform in the x direction and a 1% linear stretching is imposed in the y direction. The grid convergence analysis, for the same set of physical parameters presented at the beginning of this section, is summarized in figure 3.4 which reports the relation between the most unstable eigenvalue and the total number of grid points used in the calculations.

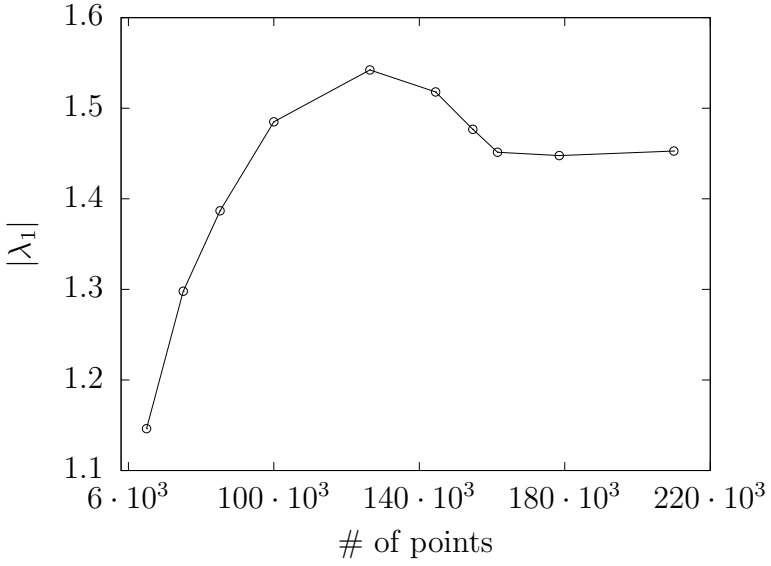

Figure 3.4 *Grid convergence analysis.*

Since the unstable region for the primary instability becomes wider increasing the Reynolds number, it is important to underline that the longitudinal domain dimension is not fixed for all the different physical cases that will be considered. Indeed, the sensitivity analysis with respect to the outlet position (see figure 3.2) has been repeated for each Reynolds number at the inlet following the exact procedure shown in this section only for the case $Re = 460$. Nevertheless, the cell dimensions $\Delta x = 7 \times 10^{-3}$ and $\Delta y_{wall} = 6.6 \times 10^{-4}$ that as obtained by means of the grid convergence analysis make the results almost independent from the spatial discretization, are still maintained for all the different calculations.
Finally, the influence of the time step on the results is studied. The size of the time step contributes the most to determine the total computational time and the memory requirements for a single calculation. Indeed, at each iteration of the Arnoldi method, the Navier-Stokes solver performs N time steps such that $T = N\Delta t$ and the base flow is retained in memory for N different time instants in order to evaluate the linearized terms in the equations (2.33). The results of the analysis are shown in figure 3.5 in terms of the integer number N into which the period T has been divided.

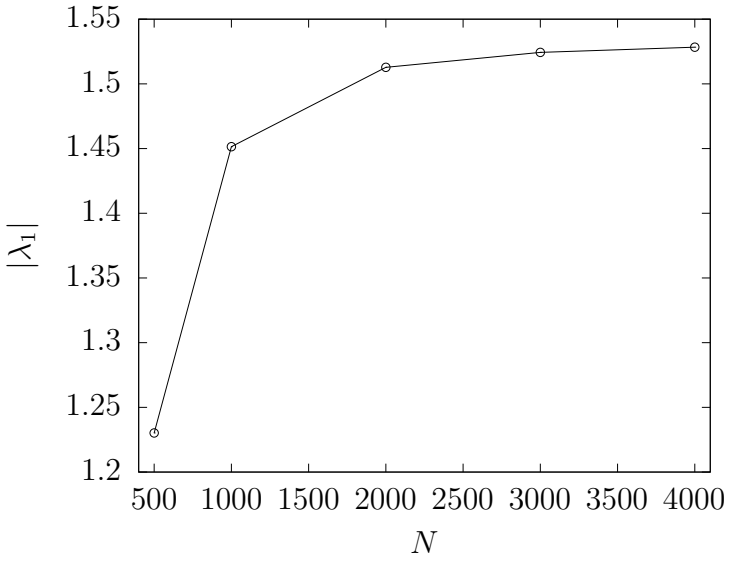

Figure 3.5 *Time step convergence analysis.*

The choice for the final simulations is $N = 2500$, which corresponds to a timestep $\Delta t \approx 10^{-3}$. Even if this value is quite large if compared to those typically used for Navier-Stokes simulations of boundary layer flows (see [83]), the norm of the Floquet multipliers exhibits variations of less than the 1% for

$N > 2000$. In addition, considering the computational constraints and also the fact that the eigenvalue problem must be solved in the three-dimensional parametric space of Re, β and A, the value $N = 2500$ appears reasonable providing qualitative results while maintaining a limited computational cost. Before listing the physical cases that have been investigated, it is worth giving some information about how the numerical parameters related to the Arnoldi method were chosen. Nowadays, the Krylov subspace iteration scheme is quite a common tool to study the stability of periodic flows. In the typical applications (see e.g. [19] or [56]), only a few eigenmodes that belong to the external part of the spectrum are computed but, concerning the secondary stability, this would lose important informations with respect to that obtained by means of the Herbert formulation. In the theory of Herbert the eigenvalue problem can be written specifically for the subharmonic, the fundamental or the detuned modes (see section 2.2) so that their growth rates can be compared at different amplitudes of the TS wave and also the range of frequencies in which the secondary modes are unstable can be analyzed. For these purposes, in this framework, it is chosen to compute a rather larger part of the spectrum composed by at least 40 eigenvalues that allows us to compare the growth rates of the modes in relation to their different detuning factor. The latter is defined by

$$\epsilon = \left| \frac{2\sigma_i}{\alpha c_r} \right|, \quad \epsilon \in [0, 1] \tag{3.84}$$

and, as can be easily seen, assumes the values 0 and 1 for the special case of the subharmonic and the fundamental modes, respectively.
As a consequence, also the dimension of the Krylov subspace is quite large since in order to retain together complex conjugate eigenvalues it must be at least $2n_{ev}+1$. Although this leads to an increase of the memory requirements, a large dimension of the Krylov subspace requires the matrix-vector product to be executed less times before the convergence on the eigenvalues is reached and thus typically reduces the computational time (see [40] for detailed information).

Re	A	β	n_{ev}	$\lvert\lambda_1\rvert$
460	0.75%	0.186	10	1.163
460	0.75%	0.186	40	1.172

Table 3.3 *Variation of $|\lambda_1|$ for two different numbers of total Floquet multipliers requested.*

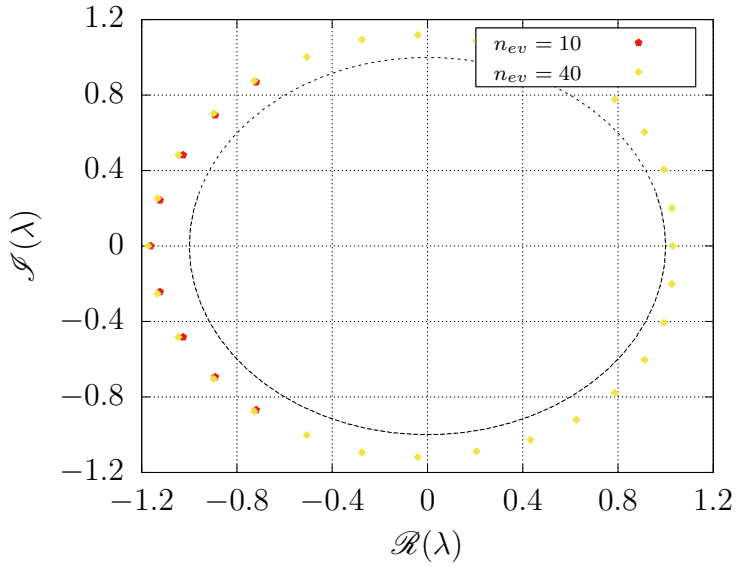

Figure 3.6 *Comparison of computed eigenvalue spectrum for $n_{ev} = 10$ and $n_{ev} = 40$. For the case $n_{ev} = 40$, only the unstable Floquet multipliers are represented in the figure.*

The variations of the results when an increasing number of Floquet multipliers is requested, have also been analyzed. The table 3.3 reports the growth rate of the most unstable mode for two values of n_{ev}, while maintaining the other parameters fixed. The variation of the norm of the Floquet multiplier when a quite large number of eigenvalues are requested, which is the case in this work, is found to be below the one per cent.
Another important aspect is the convergence speed of the Arnoldi method, which strongly depends on the spectrum. Looking at the problem in exam, a rather fast convergence rate has been observed for values of Re, β and A that lead to a strong instability of the boundary-layer flow. However, the convergence becomes slower or it is not achieved when the flow is either stable or slightly unstable providing an indication on the fact that the eigenvalues are clustered [40]. For these critical cases, this difficulty has been addressed by progressively increasing the dimension of the Krylov subspace and eventually reducing the number of eigenvalues to be computed.
The physical cases which have been studied are presented in the graph above directly on the Blasius neutral-stability curve.
The curve is represented on the Re-F plane where F is the adimensional frequency parameter defined by

$$F = 10^6 \frac{\alpha_r c_r}{Re}. \tag{3.85}$$

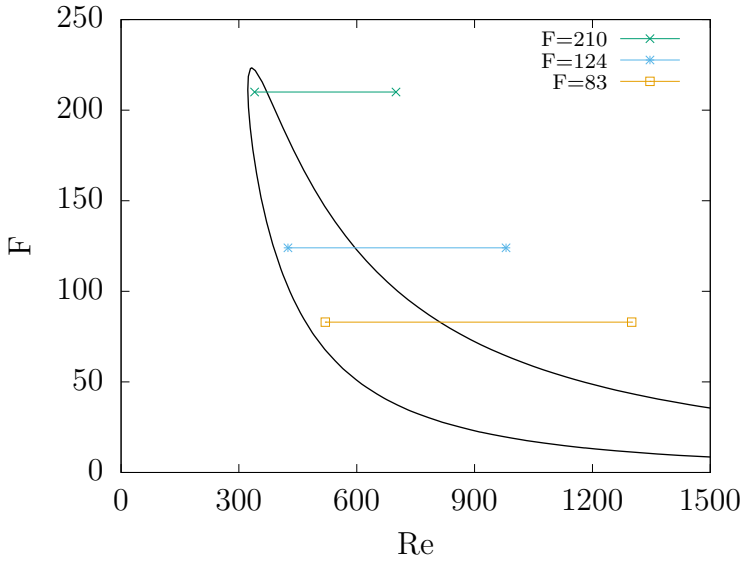

Figure 3.7 *Physical cases studied and corresponding length of the computational domain.*

This parameter, that identifies a disturbance with fixed dimensional frequency as it travels downstream, has been used historically in the literature to classify the experiments on the boundary layer transition and also by Herbert himself in the original paper of 1988 [31].
The blue and the brown lines in figure 3.7 match the experimental conditions of Kachanov & Levchenko 1984 [33] ($F = 124$) and of Saric & Thomas 1984 [61] ($F = 83$), respectively. For each of the Reynolds numbers that have been considered, the secondary stability problem has been studied for different amplitudes of the TS wave A and for a wide range of the three-dimensional disturbance wavenumber β. As already pointed out, due to the convergence behaviour of the Arnoldi method, the results that will be presented in the next chapter mainly refer to those cases for which the flow in unstable or at least near to criticality. Although also the sets of Re, A and β for which the flow is stable have been analyzed, the results do not add significant informations and the little part of the spectrum that can be computed successfully does not justify the required high computational time.

Chapter 4

Numerical results

This chapter presents the numerical results that have been obtained. It is organized as follows: at first the features of the eigenmodes are presented for the case $F = 124$ [33] together with the influence of the amplitude A on the spectrum and the behaviour of the eigenvalues as a function of the wavenumber β. The results will be also compared to those obtained by Herbert and to the available experimental data. At last, the role of the Reynolds number in the secondary stability mechanism will be clarified considering all the different cases mentioned in chapter 3. Instead, the last section of the chapter deals with some three-dimensional direct Navier-Stokes simulations that, starting from the obtained results about the secondary instability, investigate the late transitional stage and the importance of the non-linear effects.

4.1 Features of the Secondary eigenmodes

As it is well known from the literature, the subharmonic and the fundamental modes are held responsible for the two main scenarios of the natural transition, namely the H-type and the K-type transition [34]. As a matter of fact, a wide range of experiments investigating the secondary instability mainly focus on these classes of modes and especially on their interaction with the primary wave. Before actually showing the computed three-dimensional structures that develop through the secondary instability mechanism, the steady boundary layer flow $\boldsymbol{U_1}$ and the periodic base flow $\boldsymbol{U_2}$ at the initial time are presented for completeness. The pictures below refer to the case $F = 124$ and to an amplitude of the TS wave at the inlet of 1% for which, as will be better clarified in the following, the subharmonic and the fundamental modes both appear in the most unstable part of the spectrum.

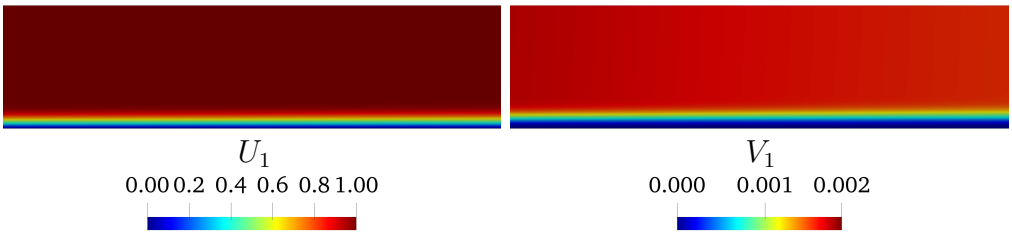

Figure 4.1 *Steady boundary-layer flow* $\boldsymbol{U_1}$.

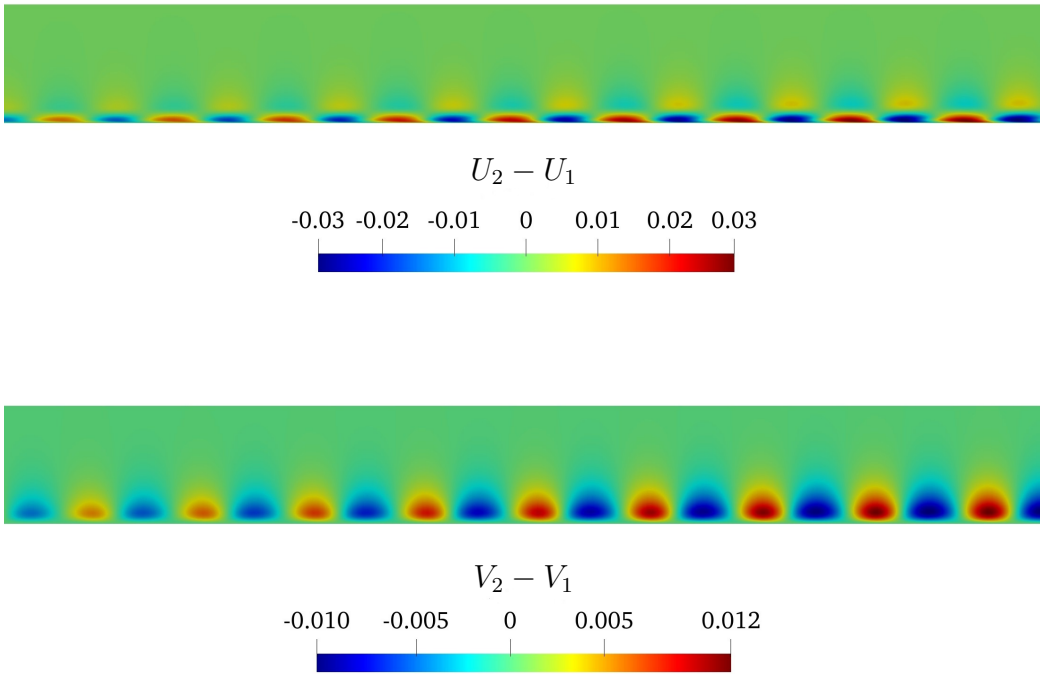

Figure 4.2 *Difference between the steady flow* $\boldsymbol{U_1}$ *and the base flow* $\boldsymbol{U_2}$ *for* $t = 0$. *This choice of representation is only for visual purposes since it clearly shows the effect of the TS wave forcing on the flow field near the wall. Moreover, the computational domain has been truncated in order to highlight the flow structures, the reader is referred to figure 4.3 for a wider view.*

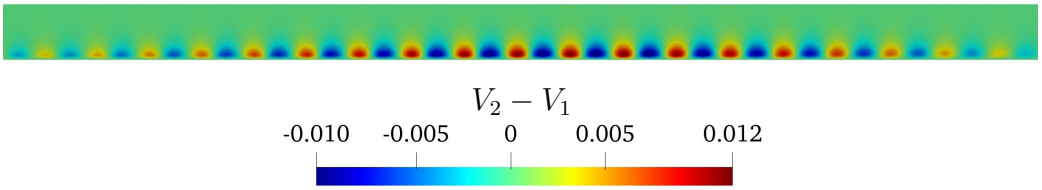

Figure 4.3 *Grow and decay of the TS wave as predicted by the linear stability theory. The v component is shown for a better visualization of the spatial development of the TS wave.*

The computed subharmonic and fundamental modes for the same base flow presented in figure 4.2 are shown below. For conciseness, only the results for the wavenumber $\beta = 0.186$ are shown that, however, are sufficient to highlight the three-dimensional flow-structures near the wall. Certainly, different values of β have influence on the grow rates of the modes but, for what concerns their qualitative features which are the focus here, they remain the same. Other aspects, such as the spatial development of the disturbances and their velocity profiles, will be treated separately in the next developments.

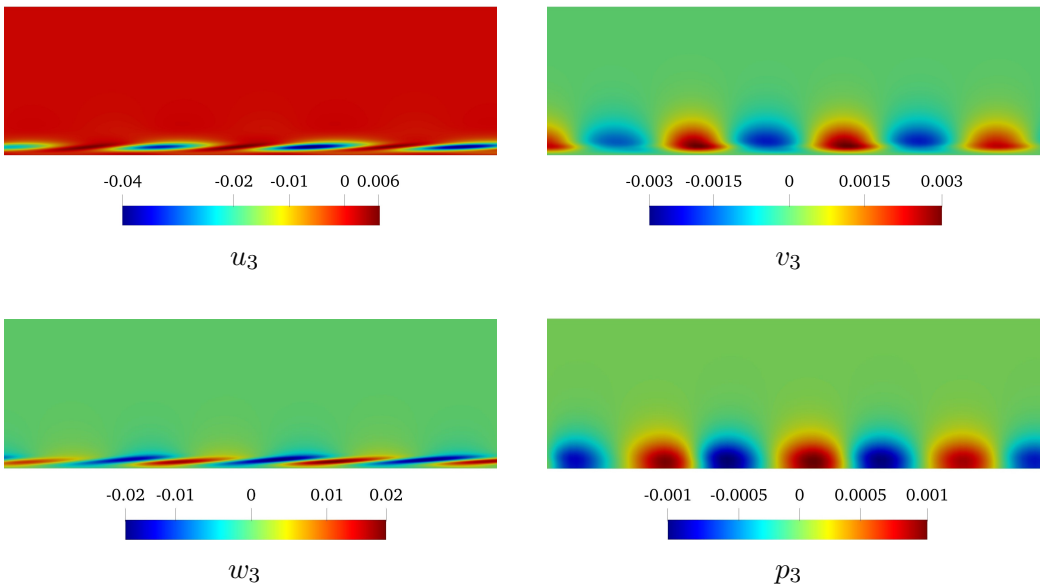

Figure 4.4 *Detail of the flow structures near the wall for the fundamental mode.*

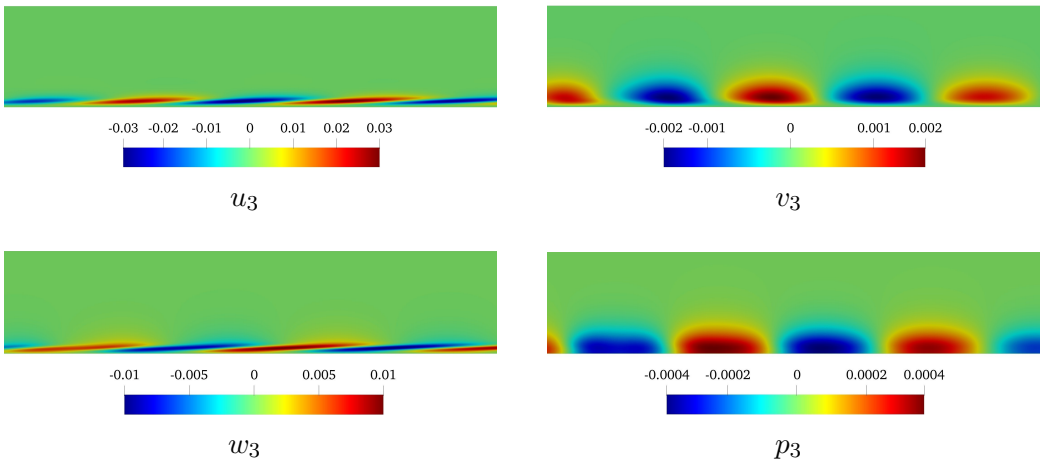

Figure 4.5 *Detail of the flow structures near the wall for the subharmonic mode.*

The three-dimensional structures shown above evolve spatially very similarly to what observed for the TS waves. In other words, they are found to be amplified in a certain region of the flow and to decay further downstream where the boundary-layer is basically undisturbed as it is shown in figure 4.6. It should be observed that the disturbances have negligible amplitude near the inlet face of the domain and also that the peak of the secondary modes is reached after that the TS wave has started to decay. The position of the peak shows a qualitative agreement with the results reported by Kachanov in [34]. However, it should be reminded that, in the experimental investigations on the secondary instability available in the literature, typically the secondary modes are excited at the inlet together with the TS wave and then their evolution is measured downstream. This set-up is quite different from the calculations performed here in which the disturbance is imposed to be null at the left boundary and therefore a slight discrepancy on the spatial evolution of the modes can be expected.
It is also interesting to observe the resultant velocity profiles of the modes and to compare them with those obtained by Herbert [31]. Indeed the classical theory of Herbert analyzes the stability of the flow from a local point of view and provides the secondary modes in term of local velocity profiles superimposed on those of the TS wave.

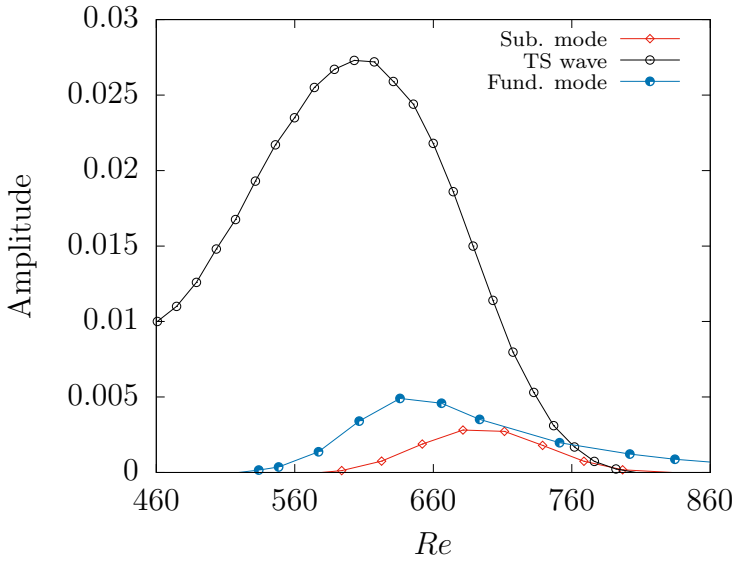

Figure 4.6 *Spatial development of both the fundamental and the subharmonic mode. The points represent the peaks of the flow structures (u velocity component) at fixed height $y = 1.5G(x_1)$. Concerning the eigenmodes, the amplitude in figure 4.6 is provided directly by ARPACK normalizing the eigenvectors and has the only purpose of showing their qualitative behaviour in the x direction.*

The figures below summarize the results for the fundamental and the subharmonic modes. The velocity profiles are taken at $Re \approx 700$ where the subharmonic mode has its maximum amplitude.

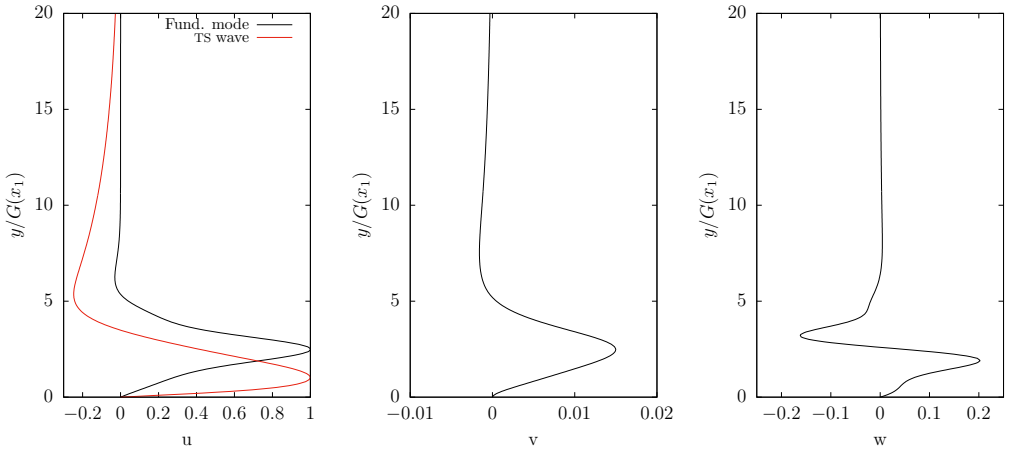

Figure 4.7 *Velocity profiles for the fundamental mode. The results are normalized such that the maximum of the u component is one and represent the centre region of the structures shown in figure 4.4.*

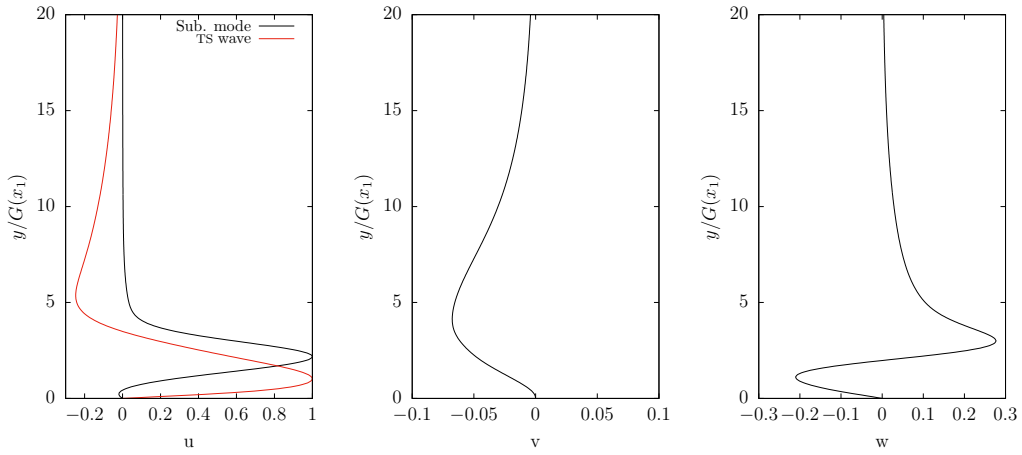

Figure 4.8 *Velocity profiles for the subharmonic mode.*

The velocity profile allows one to observe some features of the secondary modes that differ the TS waves. In general, the secondary modes exhibit their maximum activity slightly above the peak of the TS wave and show a rather rapid decay moving away from the wall, therefore they are more localized. Moreover, it should be noted that the u velocity profile of the fundamental mode presents the same structure of that of the primary wave assuming a null value at the wall, at an intermediate point and at infinity. In fact, it is well known from experiment and from former calculations [34] that the secondary modes are strictly connected to the three-dimensional modes of the Orr-Sommerfeld equation and those two tend to become more and more similar as the amplitude A of the TS wave decreases.
At last, it is important to remind that the numerical scheme based on the Krylov subspace iteration allows us to compute the eigenmodes only for a specific phase of the base flow which is considered at the initial time. The characteristics of the modes presented above have been shown for the initial time instant in which they have been computed but they, as the base flow itself, are actually a function of time. Their evolution in time has been computed separately from the eigenvalue calculation according to the governing equations (2.33). The reader should observe the periodicity properties (2.38) from the pictures below which represent, for both the fundamental and subharmonic mode, the three-dimensional flow structures at five different time instants within the period T.
It is important to underline that mathematically the fundamental and subharmonic modes correspond to a real Floquet multiplier.

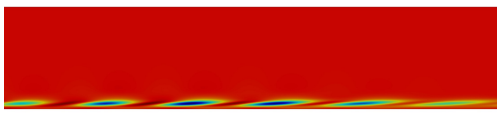

(a) $t = 0$

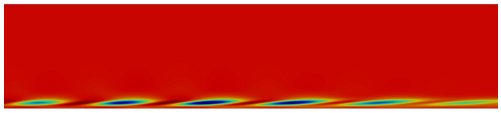

(b) $t = T/4$

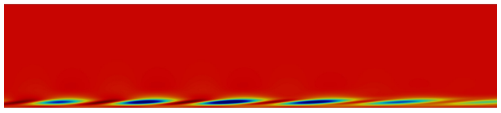

(c) $t = T/2$

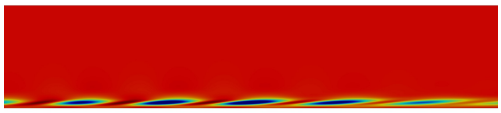

(d) $t = 3/4T$

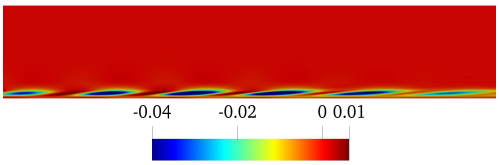

(e) $t = T$

u_3

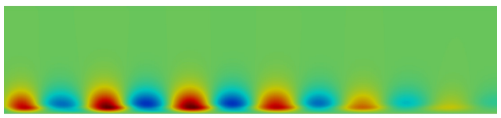

(a) $t = 0$

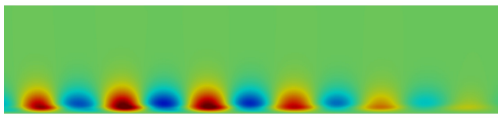

(b) $t = T/4$

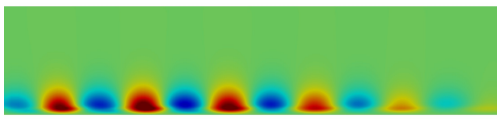

(c) $t = T/2$

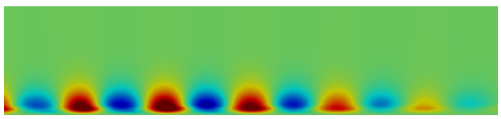

(d) $t = 3/4T$

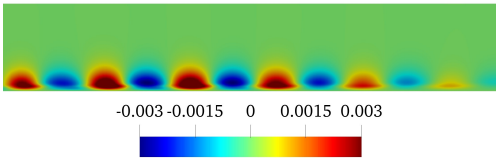

(e) $t = T$

v_3

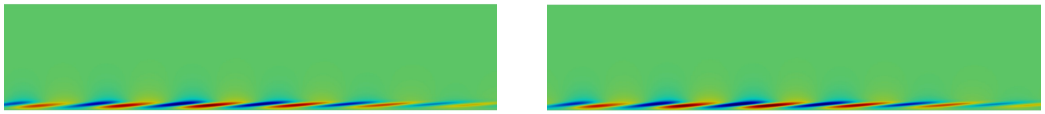

(a) $t = 0$ (b) $t = T/4$

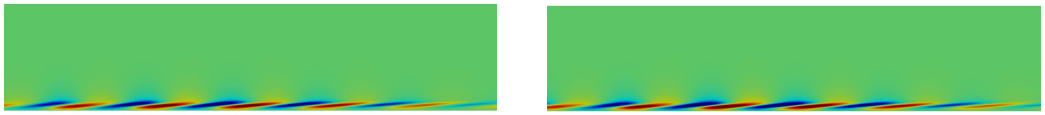

(c) $t = T/2$ (d) $t = 3/4T$

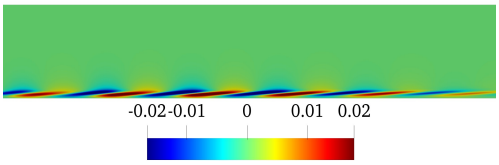

(e) $t = T$

w_3

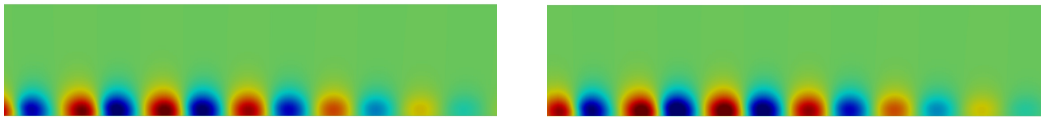

(a) $t = 0$ (b) $t = T/4$

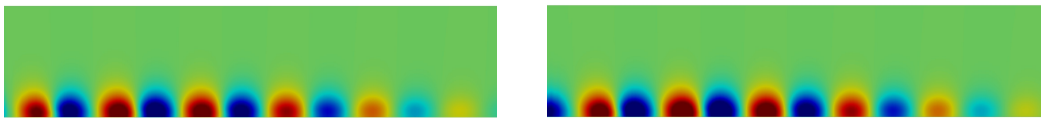

(c) $t = T/2$ (d) $t = 3/4T$

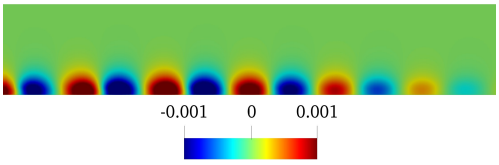

(e) $t = T$

p_3

Figure 4.9 *Fundamental mode evolution. Note that for $t = 0$ and $t = T$ the shape of the mode is unchanged, the flow-structures are only scaled by the norm of the correspondent Floquet multiplier.*

(a) $t = 0$

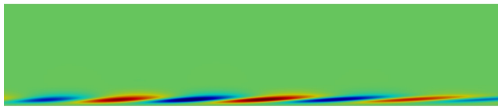

(b) $t = T/4$

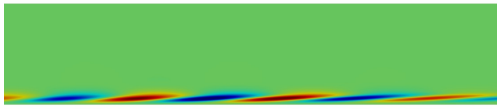

(c) $t = T/2$

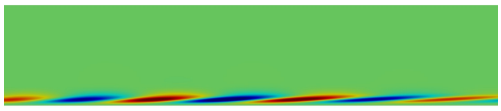

(d) $t = 3/4T$

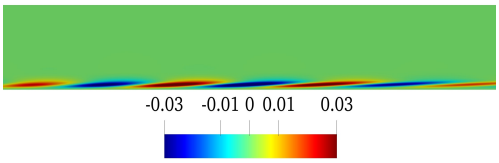

(e) $t = T$

u_3

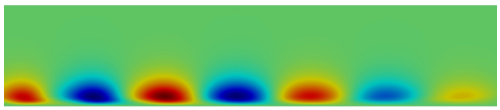

(a) $t = 0$

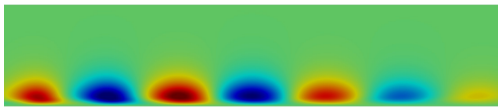

(b) $t = T/4$

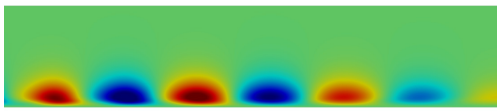

(c) $t = T/2$

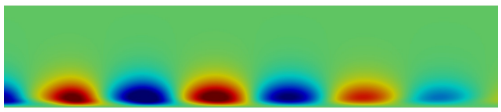

(d) $t = 3/4T$

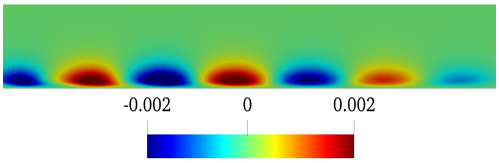

(e) $t = T$

v_3

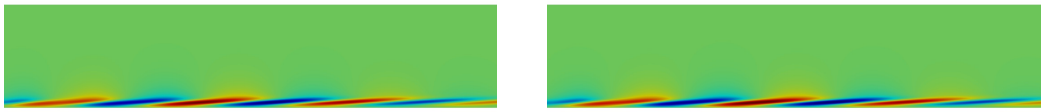

(a) $t = 0$ (b) $t = T/4$

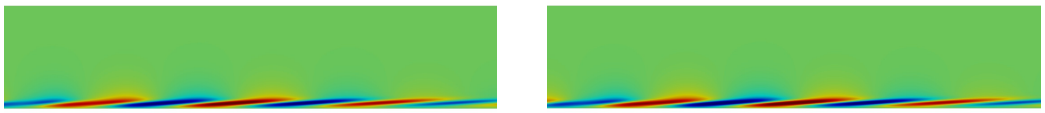

(c) $t = T/2$ (d) $t = 3/4T$

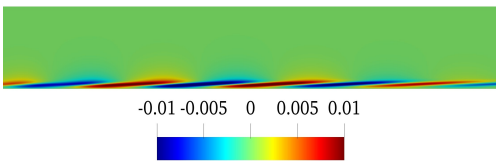

(e) $t = T$

w_3

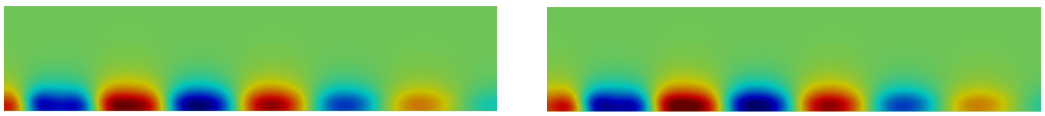

(a) $t = 0$ (b) $t = T/4$

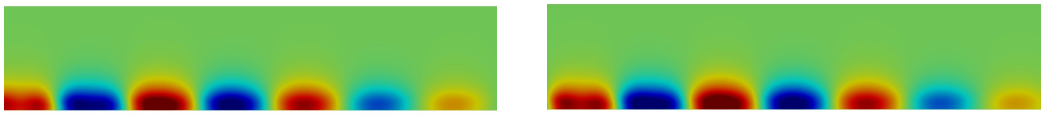

(c) $t = T/2$ (d) $t = 3/4T$

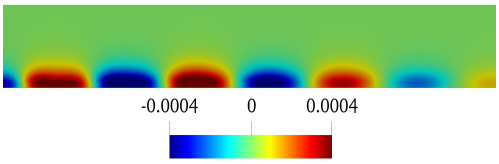

(e) $t = T$

p_3

Figure 4.10 *Subharmonic mode evolution. The reader should note that after each period T, the subharmonic mode experiences a 180° phase shift with respect to the TS wave.*

In particular, the fundamental mode is associated with a positive eigenvalue while the subharmonic mode is associated with a negative one. Physically, they represent disturbances that move synchronous with the primary wave and this fact, as also pointed out in [30], represent the optimal condition for the energy transfer from the TS wave to the secondary modes.
The whole class of detuned modes, which have not been considered until this point, are associated to complex eigenvalues and represent asynchronous travelling disturbances. In other words, they can be seen as disturbances with frequency $\omega + \Delta\omega$ where ω is the frequency of the primary wave while the shift $\Delta\omega$ depends on the detuning factor ϵ defined in 3.84. Even though the detuned modes have received limited experimental investigations since no evidence for their role in common transition's scenario has been found, they became important in all those situations when the boundary-layer flow is subjected to a random three-dimensional disturbance background.
Kachanov & Levchenko [33] found that in the H-type transition, which is dominated by the subharmonic modes, a peak of amplification appears in the spectrum for detuning modes around the subharmonic frequency, $\epsilon \approx 1$. Even in the K-type transition, dominated by the fundamental mode, the range of unstable modes can extend up to the subharmonic frequency and both modes can be present in real transitional flows. A complete understanding of the secondary instability mechanism and the analysis of the range of amplified frequency of the disturbances requires to considerer the detuned modes as well. However, so as not to weight down the discussion, a detailed description of the asynchronous modes as done for the special cases of $\epsilon = 0$ and $\epsilon = 1$ is not reported here and only a representation of the flow structures for $\epsilon = 0.6$ is proposed.

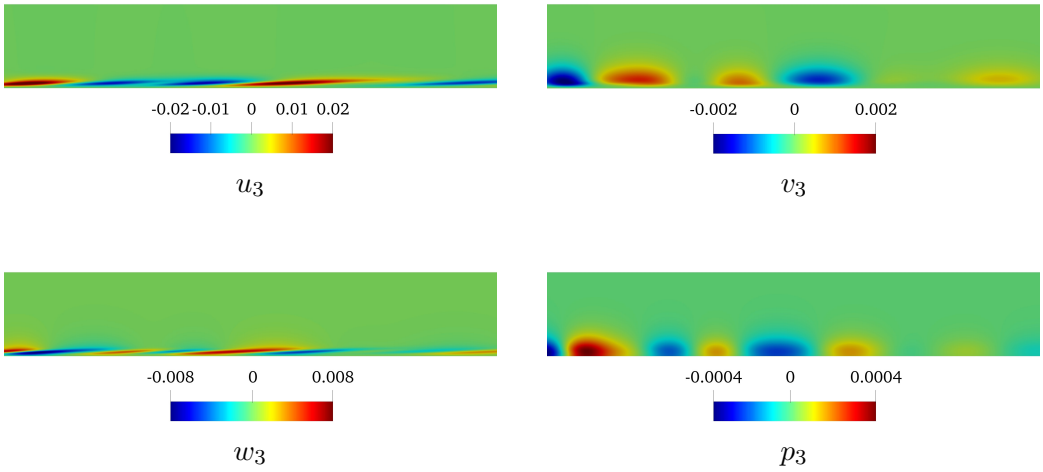

Figure 4.11 *Detail of the flow structures near the wall for the detuned mode with $\epsilon = 0.6$. The pictures represent the real part of the eigenvector.*

Nevertheless, the detuned modes will be mentioned in the next section in which the eigenvalue spectrum and the instability mechanism will be shown in detail.

4.2 Secondary Instability analysis

This section deals with the eigenvalue spectrum of the secondary instability. Particular emphasis is given to the behaviour of the eigenvalues in relation to the amplitude A, the wavenumber β and the Reynolds number. Other aspects, such as the role of the detuning factor ϵ and the limit of the theory with respect to the experimental investigations on secondary instability will be also briefly discussed here. As a first step, the eigenvalue spectrum computed for $F = 124$ and $\beta = 0.156$ is shown below for three different amplitudes A at the inlet, namely $A = 0.5\%$, $A = 0.75\%$ and $A = 1\%$. Although these amplitudes seem very close, what has been found to matter the most in terms of the behaviour of the eigenvalues is the maximum amplitude of the TS wave reached in the flow domain. For the values of A mentioned, the maximum amplitudes A_{max} obtained are 1.1%, 1.7% and 2.8%, respectively, that are separated enough to observe a qualitative difference in the spectrum.

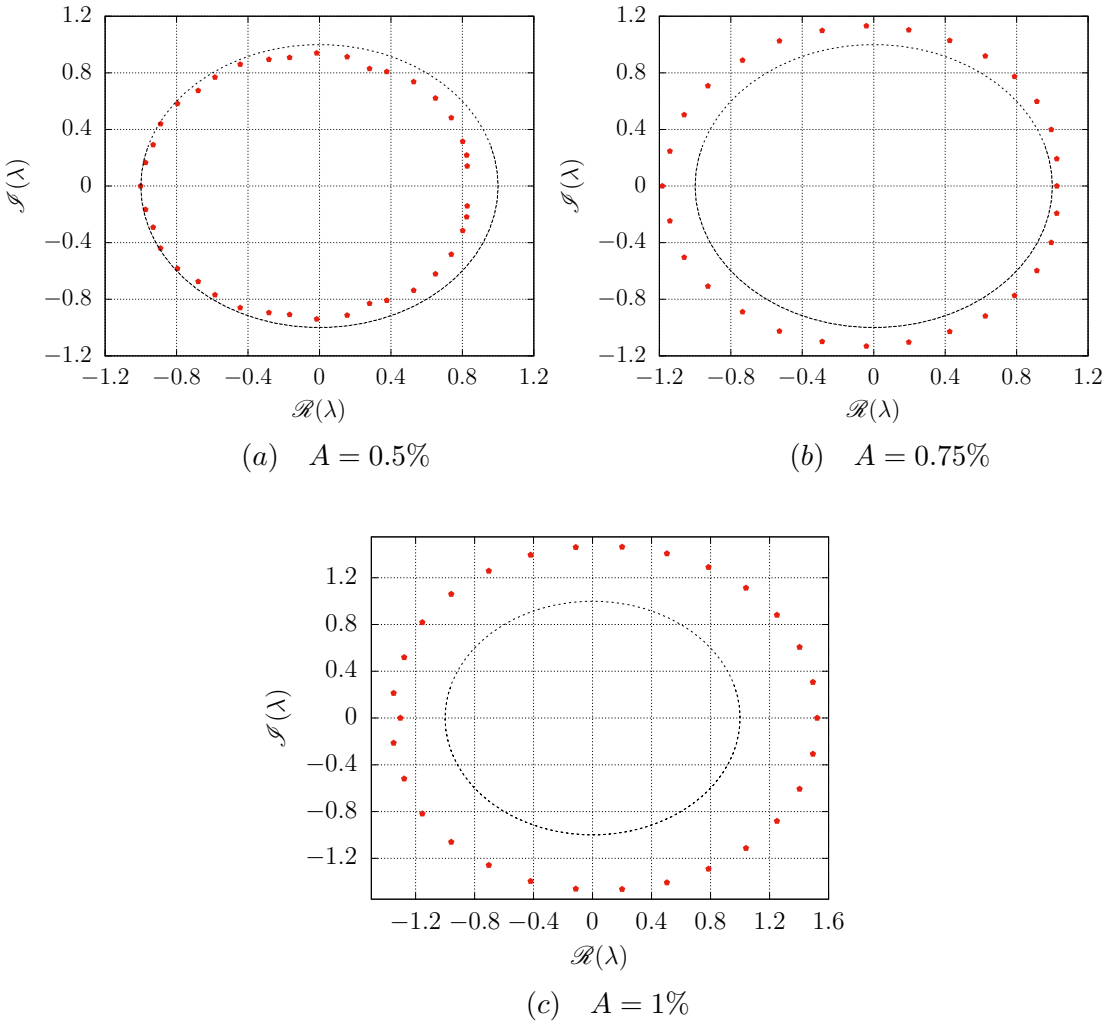

(a) $A = 0.5\%$ (b) $A = 0.75\%$

(c) $A = 1\%$

Figure 4.12 *Eigenvalue spectrum for varying amplitude A. The dashed circle in the figures delimits the stability region.*

As can be observed in figure 4.12 for $A = 0.5\%$, which in this case roughly corresponds to the stability limit of the boundary-layer flow, the subharmonic mode is the first to become unstable. As a matter of fact, for low and medium amplitudes of the TS wave, the subharmonic mode still remains the most unstable one of the spectrum. Then, as the amplitude A increases, the fundamental mode also becomes unstable and for rather high amplitudes its grow rate becomes comparable or even larger than that of the subharmonic mode. This qualitative behaviour is consistent with the features of the H-type and K-type transition presented in 1.1 and also with the results of the classical secondary stability theory of Herbert (see [31] or [43]).

However, a significant discrepancy is found for what concerns the growth rates of the modes and the threshold amplitude of the primary wave for which the instability occurs. In general, the grow rates of the eigenmodes are quite lower with respect to those obtained by Herbert and the same order of magnitude is reached only at rather high values of the amplitude A. Moreover, this fact has also been reported in the experimental investigations of Kachanov & Levchenko 1984 [33] and of Saric & Thomas 1984 [61] as an indication that the theory of Herbert, even if providing an explanation of the origin of the three-dimensional structures, overestimates the instability phenomenon that occurs in practical applications. Apparently, these discrepancies are connected with the idealized conditions under which the secondary stability theory is formulated. Indeed, due to the experimental facilities used to excite the TS wave and to modulate the secondary modes in the span-wise direction, some non-uniformities of the base flow in the z-direction are typically observed in the experiments while an ideal case of two-dimensional base flow and z-periodic secondary modes is considered in the theory. Even if these latter are the hypothesis used also in this work, it seems that the inclusion of the non-linear and non-parallel effects and especially the fact that the secondary instability is analyzed from a global point of view, brings the results closer to a more realistic situation and experiments.

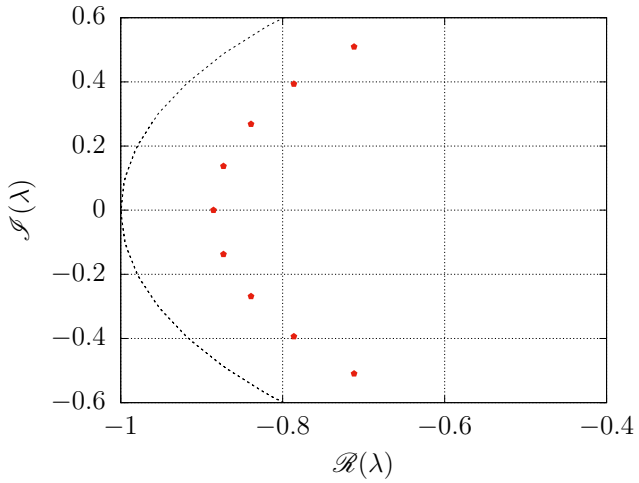

Figure 4.13 *Nine most unstable eigenvalues for $A = 0.3\%$ and $\beta = 0.156$. No instability is found but note that the subharmonic mode is still in the outher part of the spectrum.*

For what concerns the threshold value of A, the flow becomes unstable for the given set of parameters when $A_{max} \approx 1\%$, but it is anticipated here that this value is slightly dependent on the Reynolds number or alternatively on the value of the frequency parameter F. In order to give an idea of what predicted by the theory of Herbert, it is worth pointing out that, for the same conditions considered here, the subharmonic mode is found to be unstable even for $A = 0.2\%$. However, it is reminded that due the local point of view adopted by Herbert, typical of the parallel stability theory, a direct numerical comparison of the results can be misleading. On the other hand, the qualitative accordance between the two theories and especially the experimental confirmations can be taken as a good indicator of the accuracy of the results.
The behaviour of the modes for different wavenumbers β is analyzed in the next developments. The variation of the growth rates as function of β is shown in the figures below for both the subharminic and the fundamental modes, respectively.

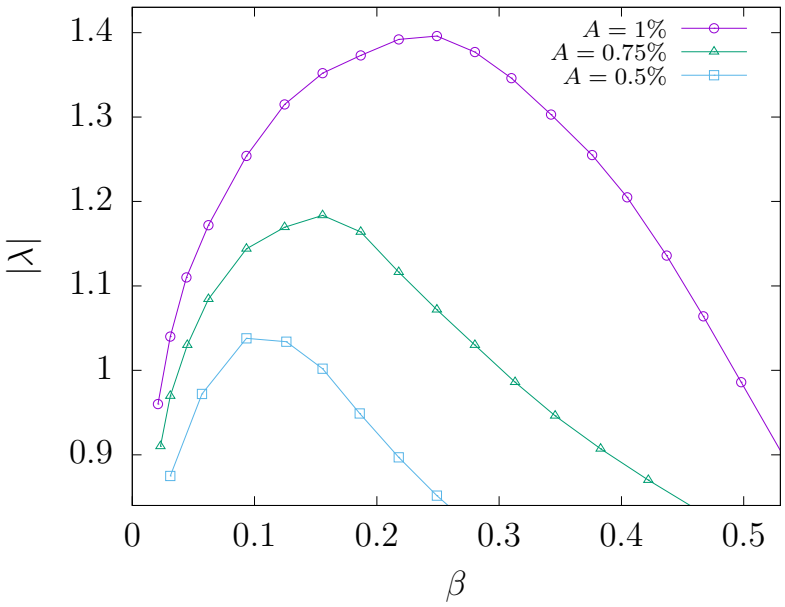

Figure 4.14 *Variation of the subharmonic growth rate as function of the wavenumber β. The reader should note the quite different behaviour of the curve for $A = 1\%$ indicating the influence of the non-linear effects.*

As a fist consideration, it should be noted that the range of wavenumbers for which an instability is found progressively enlarges for higher amplitudes of the primary wave. Moreover, it can be clearly seen that the peak of the curves moves toward larger values of β as the value of A increases. It is worth mentioning that the peak value for $A = 1\%$ which is very close to the intensity adopted in the experiment of Kachanov [33], corresponds to a propagation angle $\theta \approx 60°$ where the latter is defined by $\theta = \arctan(\beta/\alpha)$.
As a comparison, it is reported that the value observed by Kachanov is $\theta \approx 62°$ while the theory of Herbert states that the peak is at a fixed $\theta \approx 64°$ $(\beta/\alpha = 2)$ for all $A > 0.7\%$ [34].
In addition, it is interesting to observe that for low and medium amplitudes of the primary wave, the curves follow the same qualitative behaviour also found by Herbert [43]. That is, the subharmonic mode becomes unstable for a certain $\beta > 0$ and, after having reached the peak position, the growth rates show a quasi-linear decay with the wavenumber β. However, it can be noted how the curve for $A = 1\%$ is sensibly different probably due to the non-linear distortion of the base flow which starts to become relevant when the amplitude of the TS wave is high enough.

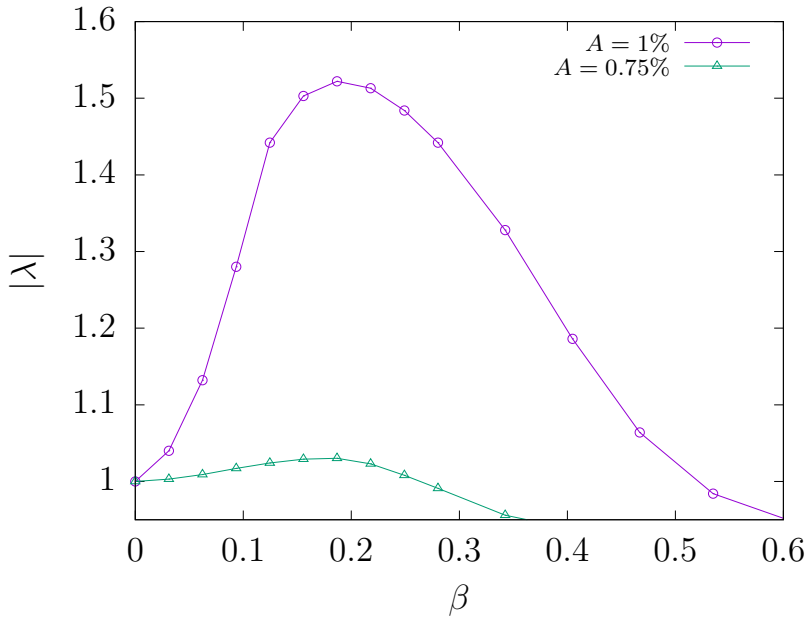

Figure 4.15 *Variation of the fundamental grow rate as function of the wavenumber β. The curve for $A = 0.5\%$ is not reported since the fundamental mode has not been found in the computed part of the spectrum for all the different wavenumbers.*

The same curves are reported also for the fundamental mode in figure 4.15. For $A = 0.5\%$, the fundamental mode has not been found in the computed part of the spectrum and for this reason the corresponding curve is not reported in the figure. In fact, as already pointed out, the fundamental mode remains stable for low amplitudes of the primary wave and thus the computation of its grow rates would have required an increase of the number of eigenvalues to be computed and consequently would have led to a huge increase of the computational time.
The reader is referred to [43] for a comparison with the results of the theory of Herbert. As can be expected, for the fundamental mode which requires a rather high amplitude of the TS wave to be observed, the curves in figure 4.15 are slightly different from those obtained by Herbert, however, good accordance is found for what concerns the position of the peak at $\beta \approx 0.2$ that, in an uncontrolled-disturbances scenario, is going to be most likely observed.
Before showing the effect of the Reynold number, the growth rates of the modes are presented in term of corresponding detuning factor.

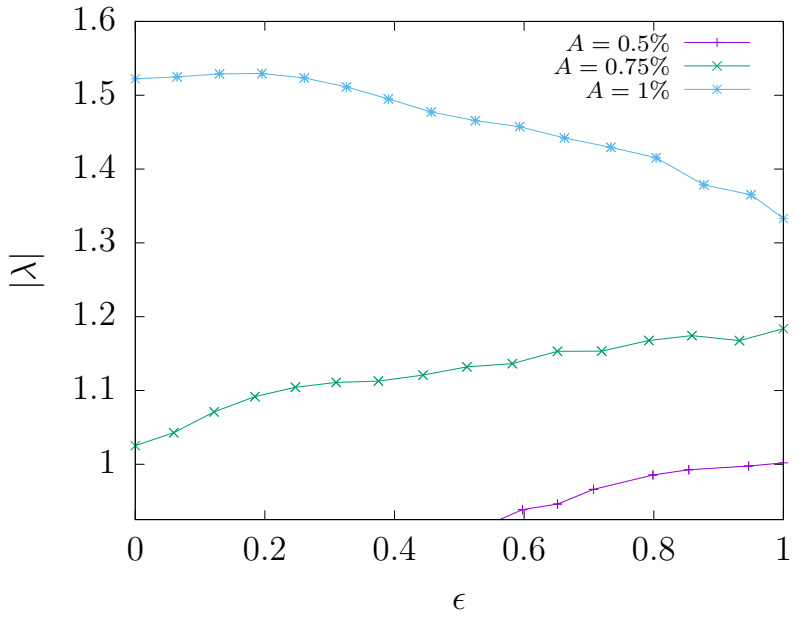

Figure 4.16 *Growth rate of the modes for different detuning factors. Figure 4.16 refers to the case $F = 124$ and $\beta = 0.18$. It is reminded that, due to the numerical scheme used in this work, not all different detuned modes are actually computed. A linear interpolation is used to join the discrete points provided by the software ARPACK.*

Although the detuning factor can be correlated to the phase angle of the complex Floquet multipliers, the figure 4.16 shows clearly the growth rates for all the detuned modes and, therefore, it is proposed to clearly underline a particular aspect of the secondary instability mechanism which is not evident in figure 4.12. For low amplitudes A, the amplification of the modes broadens in a range of near subharmonic frequencies with a tendency toward larger spanwise wave numbers as the amplitude increases. Then, for a high intensity of the primary wave, the secondary instability mechanism is capable of amplifying whatever the background provides, from the subharmonic to the fundamental frequency. The reader should note that in figure 4.16 the whole range of detuned modes becomes unstable even for $A = 0.75\%$. Moreover, it is important to notice that, for the set of parameters considered in figure 4.16, the most amplified mode for $A = 1\%$ is asynchronous with $\epsilon \approx 0.2$. This fact explains the observation of Kachanov [33] of a quite wide peak near (but not exactly at) the subharmonic frequency measured in the disturbance spectrum. Indeed, in the experiments the disturbance wavelength is typically imposed and therefore a situation similar to figure 4.16 can result where the asynchronous modes are the most amplified for that particular value of β. However, considering the realistic case in which all the wavenumbers β can be possible, the results obtained in this work, as well as those from Herbert [43], predict that the real modes will be most likely observed since they are associated with the higher growth rates.

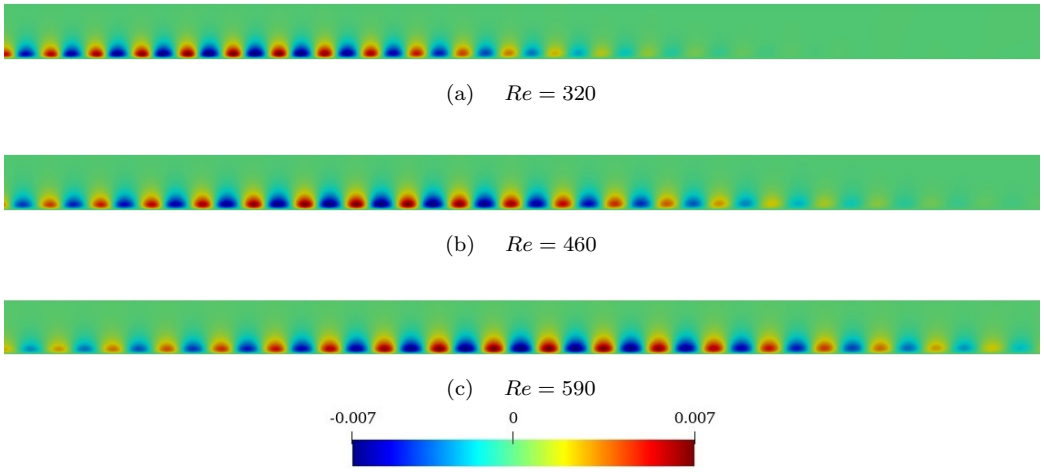

Figure 4.17 *The figure shows the difference $V_2 - V_1$ for different Reynolds numbers at $t = 0$. Note how the instability region progressively enlarges for increasing Re.*

At last, the role of the Reynolds number remains to be analyzed. It should be clear from the results reported in this section, that the primary wave has a catalytic role in the secondary instability mechanism. As shown, a higher amplitude of the primary wave leads to higher grow rates of the eigenmodes, a larger range of amplified wave lengths and so on. Therefore, it can be intuitively understood that since the low frequency TS waves are amplified in a wider region of the flow and with higher grow rates (the reader is referred to the neutral curve in figure 3.7 and to figure 4.17), these last are the most dangerous also in the secondary instability context. The results shown until this point, such as the fact that the secondary modes show their maximum activity slightly beyond the second branch of the neutral stability curve and at a slightly greater distance from the wall with respect to the TS wave, remain qualitatively unaltered and, therefore, are not shown here for the sake of brevity. Nevertheless, the computed spectrum for $F = 83$ and $\beta = 0.14$ it is proposed at two different amplitudes of the primary wave.

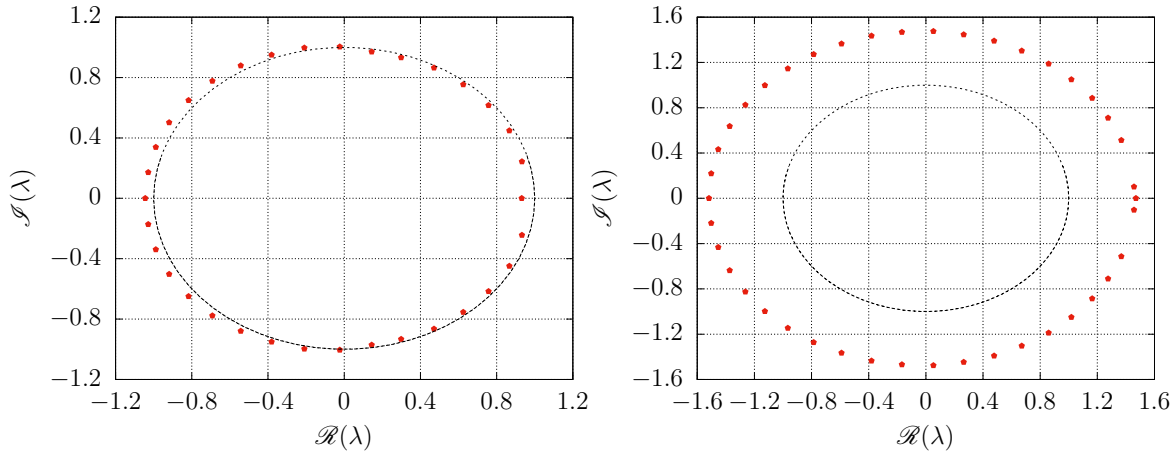

(a) $A = 0.25\%$ (b) $A = 0.5\%$

Figure 4.18 *Eigenvalue spectrum for $F = 83$ and $\beta = 0.14$. The subharmonic mode is still the most unstable while, as also for the case $F = 124$, the fundamental mode becomes unstable only for a high amplitude A_{max}.*

The shown amplitudes $A = 0.25\%$ and $A = 0.5\%$ lead to a maximum amplification in the boundary-layer flow of $A_{max} = 1.1\%$ and $A_{max} = 2.3\%$, respectively. The reader should note the same qualitative behaviour of the spectrum as for the case $F = 124$ and also the typical "circular" shape formed by the eigenvalues indicating again that the instability affects almost uniformly the whole frequency range from the subharmonic to the fundamental one. In addition, it can be observed that, even if the amplitude of the primary wave is lower with respect to the case $F = 124$, the modes exhibit larger grow rates. In fact, considering a lower frequency TS wave leads only to higher grow rates at equal maximum amplitude A_{max} but the instability features shown until here remain still valid. The calculations for $Re = 320$ also confirm this result. The spectrum for $A_{max} \approx 1.5\%$ and $\beta = 0.17$ is reported below and shows that even for this large amplitude of the primary wave the flow is still stable.

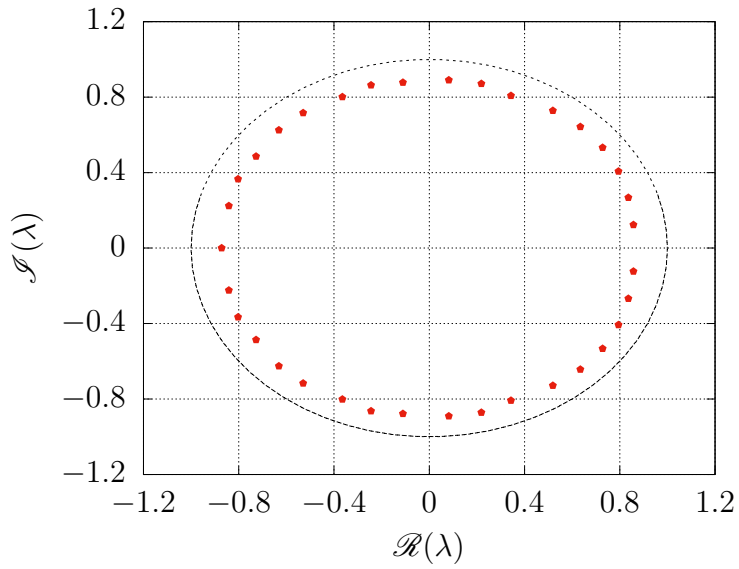

Figure 4.19 *Eigenvalue spectrum for $Re = 320$, $\beta = 0.17$ and $A_{max} \approx 1.5\%$. The boundary-layer flow is stable for this set of parameters, note that at $Re = 460$ for the same maximum amplitude A_{max} the flow was in a marked instability regime.*

Re	A_{max}	$\max_\beta \lvert\lambda_1\rvert$
320	1.2%	0.844
460	1.2%	1.012
590	1.2%	1.063

Table 4.1 *Behaviour of the most unstable Floquet multiplier for different Reynolds numbers. The reader should note how the variation of the growth rate tends to become smaller at high Re.*

In order to summarize the results, it can be stated that the increase of the Reynolds number produces a destabilizing effect, driving the instability to lower amplitudes of the TS wave but maintaining the same qualitative features. The results also provide an indication that this effect progressively reduces as the Reynolds number increases, as reported in table 4.1.

4.3 Non-linear 3D simulations

The role of the non-linear effects and the features of the late transitional stage are briefly examined in this section. Although the secondary instability mechanism has been shown in detail in section 4.2 and the results obtained are consistent with the theoretical and empirical studies, a relationship between the secondary eigenmodes (see figures 4.4 and 4.5) and the late transitional flow-structures (figure 1.1) still lacks. The approach followed in this work appears capable of explaining the three-dimensional nature of the secondary stage of the transition process but, for a complete understanding of the natural transition process, the limits of the adoption of a linear framework need to be overcome. For this reasons, taking the computed eigenmodes as a starting point, a series of DNS simulations has been performed. The choice of the computational setup, the procedure that was pursued and the obtained results are presented in the following two sections.

4.3.1 Computational setup and 3D secondary modes

The non-linear calculations are meant to simulate the situation where, in addition to the TS waves, also one secondary mode, either the subharmonic or the fundamental one, is excited inside the boundary-layer. Therefore, the computational domain is constructed by extruding the two-dimensional domain used for the stability calculations in the z direction. The grid is uniform in the spanwise direction, with $\Delta z \approx 3 \times 10^{-3}$, and extends for two wavelengths of the three-dimensional disturbance. Considering only two wavelenghts allows one to clearly observe the different arrangements of the Λ structures, as it is shown in the sequel, while limiting the total computational cost.

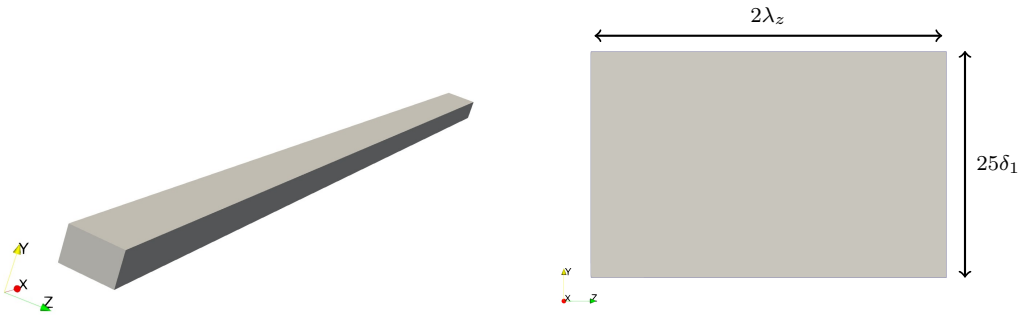

Figure 4.20 *Schematic of the three-dimensional domain. The reader should note the ratio between $y_{MAX} = 25\delta_1$ and $z_{MAX} = 2\lambda_z$. Indeed, the wavelenght λ_z of the unstable secondary modes is typically much greater than the boundary layer thickness.*

The base flow (see figure 4.2) is also simply extruded in the z direction, while for the secondary modes the definition (2.30) is applied in order to construct the corresponding three-dimensional velocity fields. The initial condition for the simulations corresponds to the three-dimensional secondary mode superimposed on the extruded base flow. The secondary modes are normalized such that the maximum amplitude of the u velocity component is a little less than the 0.1% of that of the external flow. A too high amplitude would have made it impossible to compare the disturbance evolution with the results of the stability calculations since the non-linear effects are immediately dominant. On the other hand, if the initial amplitude is too low, a longer period of time needs to be simulated before transition occurs and this results in a huge increase of the computational time.

The boundary conditions on the faces of the domain normal to the x and y directions are the same considered for the stability analysis calculations, while, for the spanwise direction, periodic boundary conditions are enforced. Before showing the results of the non-linear simulations, the three-dimensional features of the secondary modes are briefly presented below. Figure 4.21 and 4.22 show, for both the fundamental and the subharmonic modes, the u and w components of the velocity in a plane normal to the y direction at $y = 2G(x_1)$.

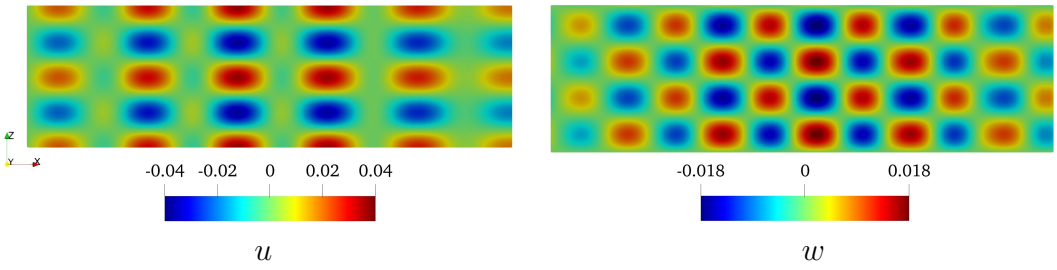

Figure 4.21 *u and w velocity components for the fundamental mode in the xz plane at $y = 2G(x_1)$. Note the alternating regions of enhanced and reduced longitudinal velocity.*

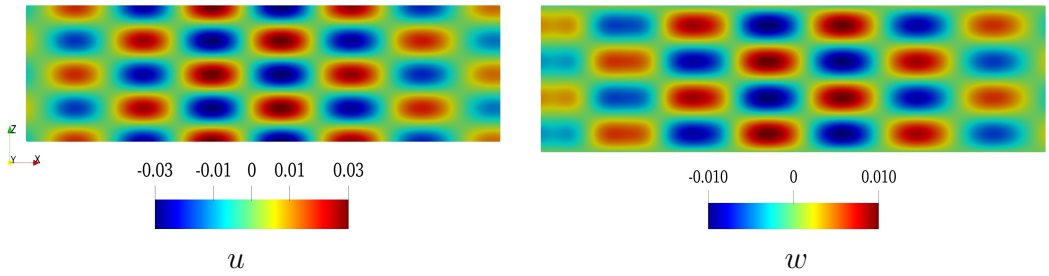

Figure 4.22 *u and w velocity components for the subharmonic mode in the xz plane at $y = 2G(x_1)$. It should be observed the different arrangement of the structures of the u component with respect to the fundamental mode.*

The three-dimensional structure of the modes is consistent with the "peak and valley splitting" [36] which is typically observed in the very first stage of the transition process, before the formation of the Λ vortices. As a matter of fact, the reader should interpret the computed secondary modes as the flow-structures observed in the natural transition at the onset of the three-dimensionality, but when still in the linear regime.
For completeness, the u component of the modes, on a plane normal to the x-direction and for different streamwise stations, is shown in figures 4.23 and 4.24. The view on the xy plane will not be shown here since it does not add significant information with respect to the visualizations provided in section 4.1.

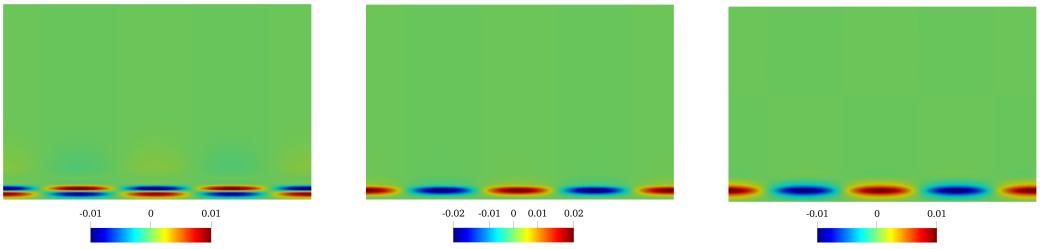

(a) $Re = 580$ (b) $Re = 640$ (c) $Re = 720$

Figure 4.23 *Longitudinal velocity component u of the fundamental mode in the yz plane at different streamwise positions. As the Reynolds number increases, and consequently also the boundary-layer thickness, the flow structures reach their peak further from the wall.*

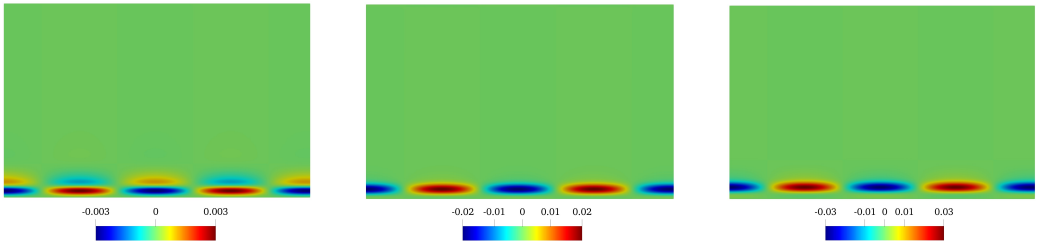

(a) $Re = 580$ (b) $Re = 640$ (c) $Re = 720$

Figure 4.24 *u velocity component of the subharmonic mode in the yz plane. Figure (c) corresponds approximately to the maximum activity of the eigenmode.*

4.3.2 K-type transition

This section illustrates the results of the K-type and H-type transition simulations. The physical cases which have been considered in the calculations are summarized in table 4.2. The parameter B indicates the initial amplitude of the secondary modes with respect to the external flow, exactly as the value A does for the TS wave.

Re	A	β	ϵ	B
460	1%	0.156	1	0.08%
460	1%	0.156	0	0.06%

Table 4.2 *Physical parameters for the 3D simulations. The reader is referred to figure 4.12 for the corresponding results from the secondary stability analysis.*

The reader is reminded that the eigenvalues spectrum, for the same set of parameters considered here, has already been shown in figure 4.12. The fundamental mode is found to be the most unstable with an associated Floquet multiplier of $\lambda = 1.503$.
In the following discussion, the results will be shown first for the K-type transition and subsequently for the H-type. The velocity field at the initial time is reported in figure 4.25, the fundamental mode can only be barely seen in the downstream region where the amplitude of the TS wave is low enough. For a quite large time interval the flow evolves very closely to what predicted by the linear stability calculations, that is, the shape of the secondary modes remains unaltered after every period T and its magnitude continues to grow following an exponential law.

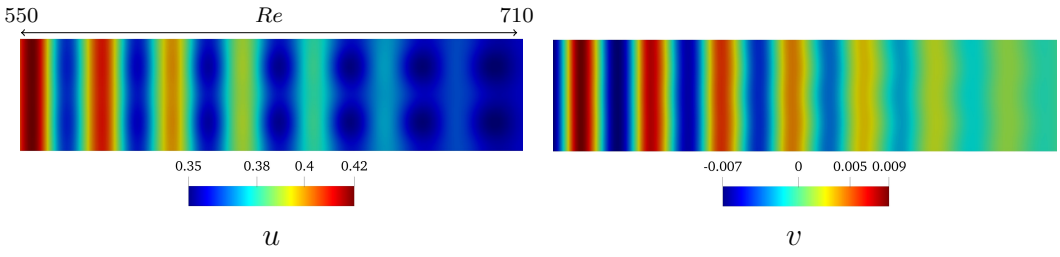

Figure 4.25 *u and v velocity components at $t = 0$ in the K-type transition simulation. The picture represents the top view on the $y = 2G(x_1)$ plane.*

The amplification factor of the mode has been estimated looking at the w velocity component which is only due to the introduction of the three-dimensional disturbance on the two-dimensional boundary-layer flow.
Table 4.3 reports the growth rates for the first time periods of the simulation during which a significant change in the mode shape has not been observed.

t	$\|\lambda\|$
T	1.515
$2T$	1.522
$3T$	1.533
$4T$	1.548

Table 4.3 *Growth rates of the fundamental mode from the 3D simulation. Each row of the table reports the amplification factor of the mode (right) calculated by comparing the amplitude at the time instant on the left and that at the previous time period.*

For the initial time periods, the computed growth rates agree well with the non-linear calculation showing a variation in the order of one per cent. Then, as the amplitude further increases, the amplification factor slightly departs from that predicted by the linear theory. However, it should be considered that, due to the high amplitude of the TS wave, the non-linear effects could play an important role from the very beginning of the simulation. In addition, differently from the assumptions on which the linear calculation was based, the secondary mode is free to interact with the periodic base flow and therefore the results should be compared only from a qualitative point of view.
It is important to point out that, according to the linear theory, the amplitude of the fundamental mode grows of about an order of magnitude within six cycles of the primary wave. Then, the disturbance evolution is dominated by the non-linear effects. Figure 4.26 shown the evolution of the longitudinal velocity component during the non-linear stage, while the evolution of the v and w components is reported in figure 4.27 and 4.28, respectively.

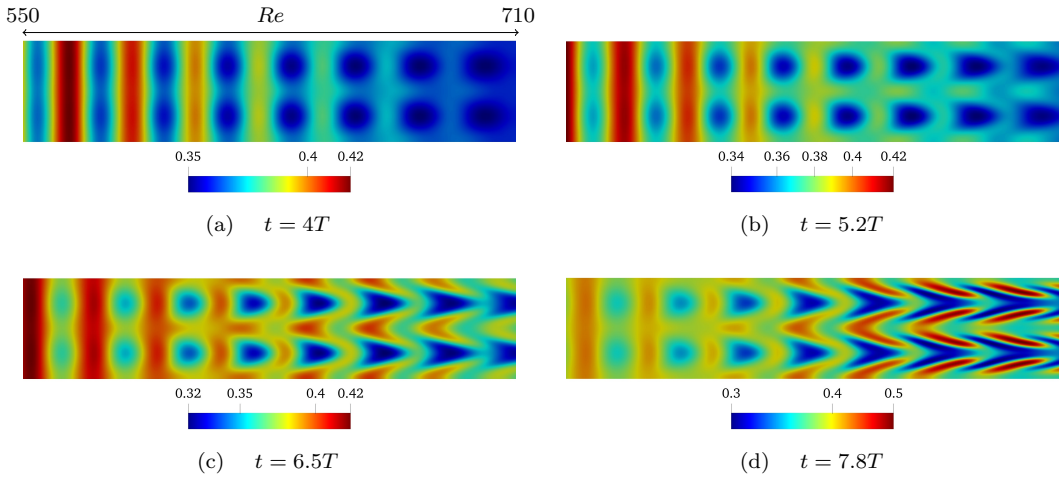

(a) $t = 4T$ (b) $t = 5.2T$

(c) $t = 6.5T$ (d) $t = 7.8T$

Figure 4.26 *Top view for the instantaneous longitudinal velocity component u on the $y = 2G(x_1)$ plane. Note the λ-shaped accumulations and the alignment of the flow structures.*

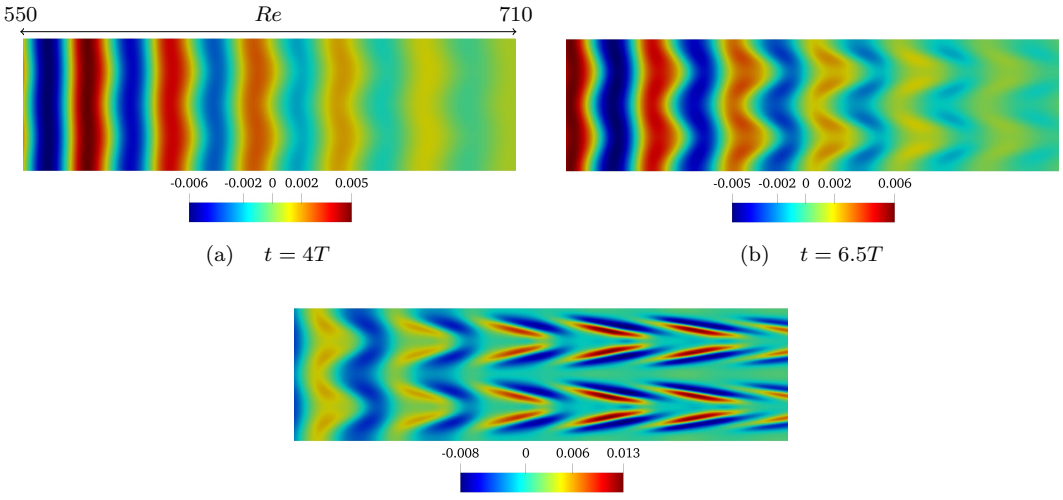

(a) $t = 4T$ (b) $t = 6.5T$

(c) $t = 7.8T$

Figure 4.27 *Top view for the instantaneous wall-normal velocity component v on the $y = 2G(x_1)$ plane.*

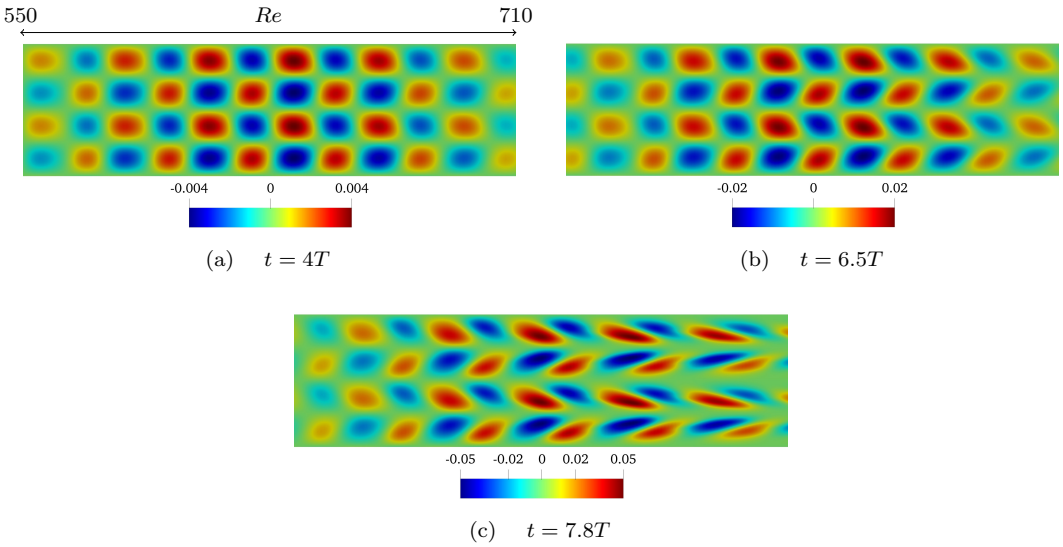

Figure 4.28 *Top view for the instantaneous spanwise velocity component w on the $y = 2G(x_1)$ plane.*

The non-linear stage lasts approximately five cycles of the primary wave. In the practical applications, the latter lasts much less than the linear phase when realistic initial amplitudes of the disturbances are considered. When the transition occurs, the flow presents λ-shaped accumulations which are aligned in rows as observed in the experiments (see e.g. [7] or [34]). The top view of the u component at the onset of turbulence is shown in figure 4.29 where the aligned arrangement in the longitudinal direction of the λ vortices can be clearly seen.

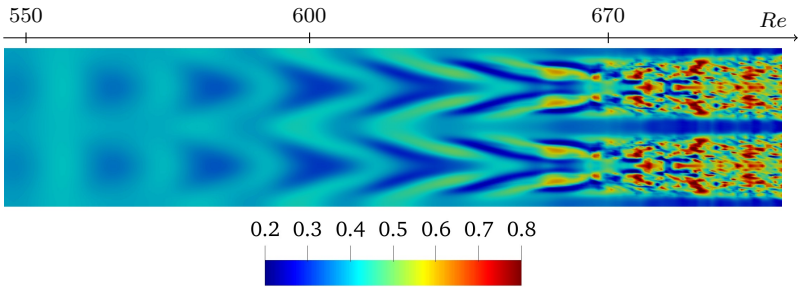

Figure 4.29 *Top view for the instantaneous u velocity component on the $y = 2G(x_1)$ plane at $t = 9.2T$. Note how the turbulent regions develop from the extremity of the λ vortices and then remain separated. Further downstream, the turbulent regions rejoin (not shown in the figure) and the turbulent boundary-layer cannot be traced back to the pattern of the initial instability (see [62]).*

The transition position corresponds roughly to $Re = 670$ ($Re_x = 4.5 \cdot 10^5$) which is well within the range provided in the literature (see [66]). Nowadays, the mechanism which drives the boundary-layer toward turbulence is well known and it has been widely analyzed in the literature (see [62]). The longitudinal vortex structures that develop in the non-linear stage lift up to form the λ vortices. Then, as their intensity grows, the λ structures deform and they originate Ω or ring-like vortices that are the last structures that can be observed before the final breakdown of the laminar flow. A three-dimensional visualization of this process is provided in figure 4.31

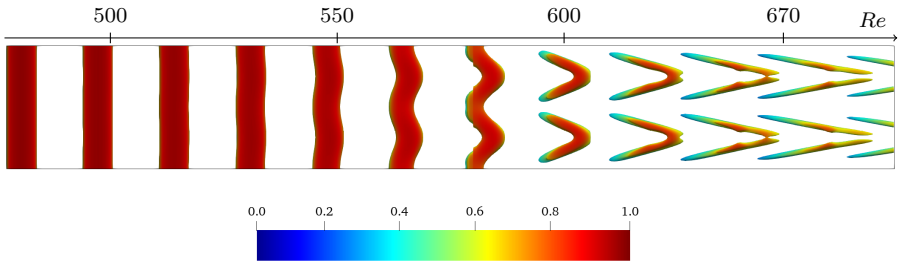

Figure 4.30 *Instantaneous isosurfaces of the second invariant of the velocity gradient tensor, Q, coloured by the streamwise velocity component u. The figure shows the longitudinal vortex system at $t = 7.8T$ before the transition occurs. The reader should note the aligned arrangement of the λ structures.*

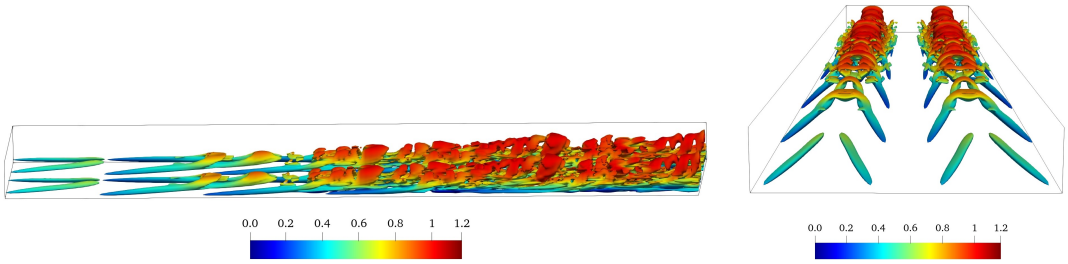

Figure 4.31 *Instantaneous isosurfaces of the second invariant of the velocity gradient tensor, Q, coloured by the streamwise velocity component u. The portion of the domain represented goes from $Re = 590$ to $Re = 750$. The figure shows the lift up of the λ vortices and the formation of ring-like vortical structures.*

A complete characterization of the late-transitional stage is far outside the scope of the present work. However, the non-linear simulation shows that when the boundary layer flow is excited with the three-dimensional fundamental mode, computed by means of the secondary stability theory, the transition process is in high qualitative agreement with the experiments available in the literature. As a matter of fact, it is well known that the origin of the λ structures is due to a three-dimensional vorticity perturbation near the wall. The secondary stability theory explains the origin of these perturbations and provides the corresponding three-dimensional velocity fields.

4.3.3 H-type transition

Finally, the results of the H-type transition simulation are reported. The same considerations made for the K-type transition, such as the initial quasi-linear evolution of the disturbances and their subsequent non-linear deformation, remain still valid and are not repeated here for conciseness. The results are presented in order to highlight the difference between the K-type and the H-type transition and to show the qualitative agreement with experiments. Figure 4.32 shows the evolution of the u component of the velocity in the non-linear stage. It should be noted that, even thought the initial amplitude of the subharmonic mode is greater with respect to that of the fundamental mode, the non-linear stage is observed after a larger time interval.

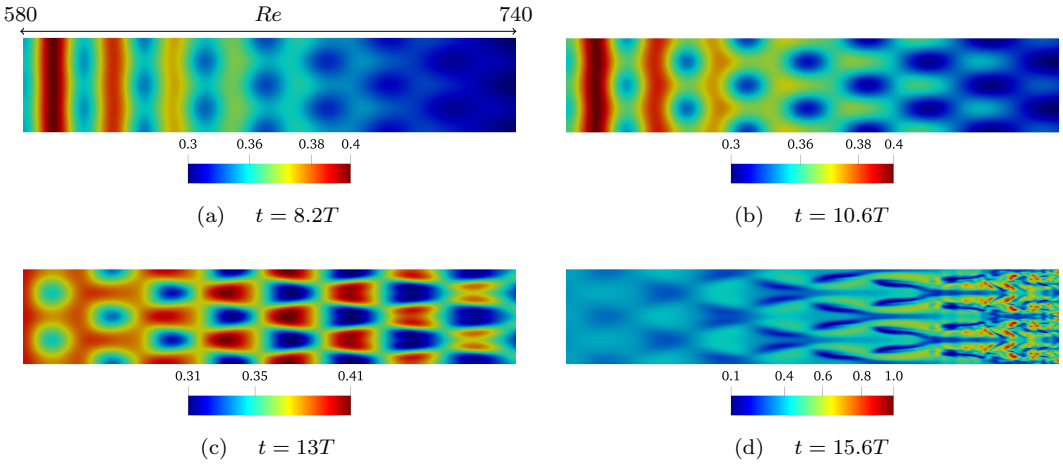

Figure 4.32 *Top view for the instantaneous longitudinal velocity component u on the $y = 2G(x_1)$ plane. Note the staggered arrangement of the flow structures.*

In fact, according to the stability calculations, the norm of the Floquet multiplier is $|\lambda| \approx 1.3$ and, therefore, the amplification of the disturbance is weaker than in the K-type transition. The transition point, similarly to what observed for the K-type transition, is located slightly further downstream than the maximum of the secondary mode (the reader is referred to figure 4.6), indicatively at $Re_x = 5 \cdot 10^5$. At the late transitional stage, the λ vortices appear but present a staggered arrangement as it is shown in figure 4.33.

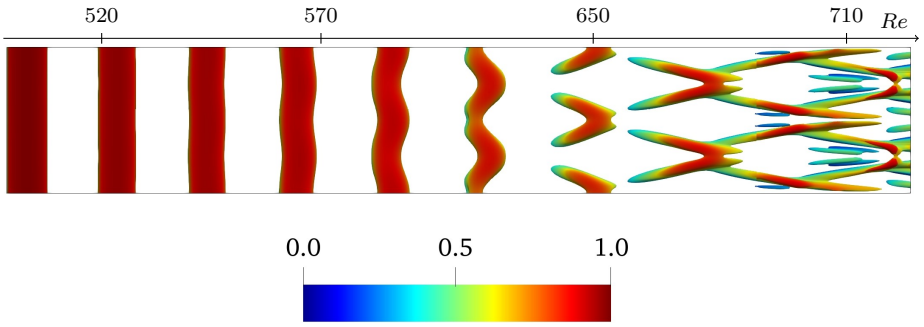

Figure 4.33 *Instantaneous isosurfaces of the second invariant of the velocity gradient tensor at $t = 13T$, coloured by the streamwise velocity component u. Note the staggered pattern of the flow structures.*

The spatial period of the flow structures in the streamwise direction is found to be two times that observed in the K-type transition, as also reported by Herbert [31]. Lastly, the breakdown of the laminar flow is driven by the formation of ring-like vortices.

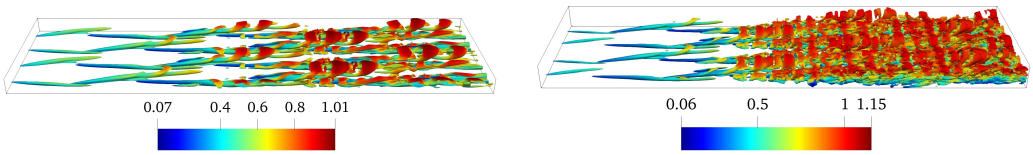

(a) $t = 13T$ (b) $t = 15.6T$

Figure 4.34 *Instantaneous isosurfaces of the second invariant of the velocity gradient tensor coloured by the velocity component u in the H-type transition. The region represented is across the turbulent transition, from $Re = 660$ to $Re = 760$.*

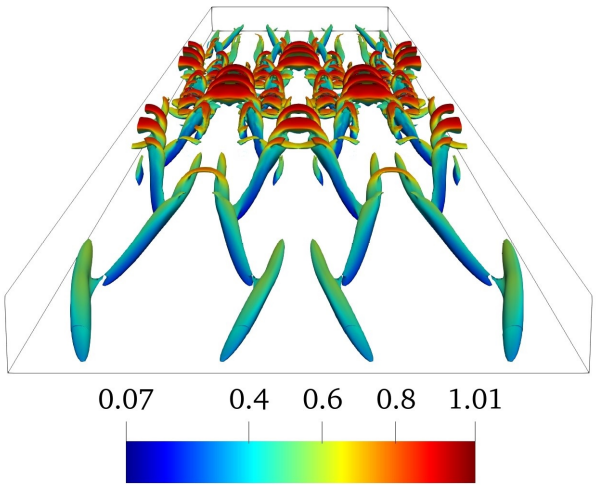

Figure 4.35 *Instantaneous isosurfaces of the second invariant of the velocity gradient tensor coloured by the streamwise velocity component u. The figure shows the spatial development of the ring vortex system.*

For completeness, the vortex system just before and at the transition to turbulence is reported in figure 4.34, while figure 4.35 highlights the formation of the hairpin vortices at the late transitional stage.

Chapter 5

Conclusions and outlook

The present work aimed to investigate the early three-dimensional stage of the natural transition. The secondary stability theory proposed by Herbert [31] has been reformulated to include the non-linear and non-parallel effects in the development of the Blasius boundary-layer forced by the T-S waves. The base flow, which represents the experimental situation in which the T-S waves are excited by a vibrating-ribbon [36], has been computed by means of the incremental pressure-correction scheme proposed in [12] which is based on the direction-splitting technique [27]. The Navier-Stokes equations are then linearized around the periodic base flow and, exploiting the normal-mode hypothesis, the secondary stability eigenvalue problem is derived. The computation of the secondary modes is achieved by the IRAM algorithm, implemented in the software package ARPACK [40]. The basis of the Krylov subspace is constructed by integrating the governing equations for the three-dimensional disturbances over a time period of the primary wave.
The stability problem is solved in the parameter space of F, A and β paying attention to the set of physical parameters for which an instability is found. The analysis shows that the synchronous modes are associated with the larger growth rates, as also found by Herbert [31]. The amplitude of the primary wave strongly influences the instability features, indeed, it is found that subharmonic modes dominates for low amplitudes A while the fundamental mode become unstable only for high amplitudes of the T-S wave. Moreover, as A increases the three-dimensional modes become unstable in a wider range of wavenumbers β. The results for $F = 124$ and $A = 1\%$ are compared with the experiment of Kachanov [33] that corresponds to this set of parameters. The propagation angle $\theta = \arctan(\beta/\alpha) = 62°$, associated with the subharmonic mode observed by Kachanov, almost matches that found in this work at the growth-rate peak in the wavenumbers interval. The dependency of the norm

of the Floquet multipliers on the detuning factor ϵ reveals that, also in the frequency range, the secondary stability mechanism is capable of amplifying all the detuned modes with $0 < \epsilon < 1$, when the amplitude A is high enough. The instability features found in the present work, are in accordance with the theory of Herbert except for the growth rates of the modes that, for equal amplitude A, are quite lower. This discrepancy can be due to the inclusion of the non-parallel effects which lead to analyze the stability of the boundary-layer from a global point of view, in sharp contrast with the local stability concept pursued by Herbert. Nevertheless, the growth rates of the modes and the threshold value of A for the instability to occur are in good qualitative agreement with the experimens of Kachanov & Levchenko [33] and Saric & Thomas [61]. The effect of the Reynolds number is investigated, and is found that low-frequency T-S waves produce a stronger instability, although retaining the same qualitative features already observed. The evolution of the secondary modes has been analyzed through a series of DNS simulations which permit the interaction between the periodic base flow and the three-dimensional disturbance. It is found that, when the latter has a sufficiently low amplitude, the observed growth rates are in an close agreement with those provided by the stability calculations. Then, for high amplitudes, a non-linear distortion of the flow structures is observed which leads to the formation of Λ-shaped vortices. The boundary layer flow is driven to transition through a process of lifting of the vortex lines, and the subsequent formation of ring-like vortices that travel downstream, as also observed by Sayadi *et al.* [62]. Two different arrangements of the Λ structures have been observed. When the fundamental mode is excited inside the boundary-layer, the Λ vortices are aligned in rows whereas, if the subharmonic mode is excited, the Λ vortices arrange themselves in a staggered pattern. These scenarios correspond to the K-type and H-type natural transition which, as reported by Herbert [31], are dominated by the fundamental mode and the subharmonic mode, respectively. These results lead to conclude that the computed secondary modes are capable of inducing the transition process and that the Λ vortices are due to their non-linear deformation in the late transitional stage.

5.1 Outlook on future work

The presented results provide an insight into the secondary instability of the boundary-layers, however, there are still numerous aspects which deserve further attention.
Firstly, the features of the secondary instability for higher Reynolds numbers need to be investigated. The variation of the growth rate of the most unstable mode as function of Re, reported in Table 4.1, provides an indication that the secondary instability phenomenon has an asymptotic behaviour. This is an aspect that should be better analyzed in future investigations and that can provide a better understanding of the three-dimensional transitional stage in general.
Regarding the instability mechanism, an important missing aspect is how the Floquet multipliers are affected by a base flow modification. Mathematically, this sensitivity analysis requires the adjoint eigenvalue problem of the secondary instability to be solved as well (see [23]). The solution of the perturbed eigenvalue problem can provide important information for the development of boundary-layer control (BCL) techniques aimed at containing, or even enhancing, the instability.
In section 2.1, it has been anticipated that the base flow can be defined including further effects. For instance, the same procedure followed in this work can be applied to the Falkner-Stan velocity profile in order to include the effect of an adverse pressure gradient. In addition, the influence of a small curvature of the solid wall can also be included provided that the differential problem (2.19) is opportunely redefined. These effect have been extensively analyzed in the primary-stability context [2], an investigation also in the secondary stability framework awaits its turn. Finally, there still remains some unanswered questions regarding the importance of non-linear effects in practical applications. Firstly, the presence of multiple primary waves with different frequencies should be investigated when defining the base flow. A single frequency T-S wave forcing is unlikely to happen in real engineering applications, typically characterized by an uncontrolled disturbance background. Secondly, the reason why the natural transition process is dominated by the synchronous modes is still unclear. The results obtained in this work confirmed that the fundamental and the subharmonic modes are associated to the largest growth rates. However, as shown in figure (4.16), the instability can affect a wide range of detuned modes that in the real cases are going to be excited. The non-linear interaction mechanism between the different secondary modes, and the subsequent predominance of the real ones that leads to the H-type or K-type scenario, needs to be clarified and requires mathematical tools far beyond the power of a linear stability theory.

Appendix A

Estratto in italiano

La transizione dal regime laminare a quello turbolento è stata oggetto di molti studi negli ultimi due secoli. Al giorno d'oggi, una più profonda conoscenza dei meccanismi fisici che provocano la transizione è molto richiesta in ambito industriale e in particolar modo in quello aeronautico poiché, quest'ultima, influenza fortemente le caratteristiche aerodinamiche dei corpi immersi. In particolare, le applicazioni tipiche in ambito aeronautico sono caratterizzate da una bassa intensità dei disturbi di fondo che fanno sì che la transizione si presenti come una sequenza di eventi riproducibili prendendo il nome di "transizione naturale" [34]. La nostra conoscenza del regime transizionale ci arriva principalmente da una vasta gamma di esperimenti su lamine piane o, con lo sviluppo dei moderni strumenti di calcolo, da simulazioni dirette delle equazioni di Navier-Stokes (DNS) (vedi [71], [62]). A causa del costo computazionale elevato che le simulazioni DNS possono avere, specialmente a numeri di Reynolds elevati, il loro utilizzo resta però tecnicamente impossibile nelle applicazioni pratiche ingegneristiche. La teoria della stabilità secondaria, proposta da Herbert nel 1984 [31], rappresenta una conveniente alternativa alla DNS e per questo viene talvolta utilizzata come strumento per predire la transizione. Questo lavoro di tesi si pone l'obbiettivo di indagare, sempre nell'ambito della stabilità secondaria, l'importanza degli effetti non lineari e di non parallelismo nel flusso base che sono stati trascurati nella formulazione originaria di Herbert. La transizione naturale può essere suddivisa in tre fasi fondamentali: la ricettività [48], cioè il meccanismo mediante il quale i disturbi esterni entrano nello strato limite, la fase lineare e, per ultima, la fase dominata dagli effetti non lineari che provocano il passaggio finale del flusso al regime turbolento. La fase lineare è stata storicamente oggetto di numerose teorie matematiche a partire dai lavori fondamentali di Tollmien e Schlichting ([75], [65]) in cui, per la prima volta, si sono calcolate le autosoluzioni instabili

dello strato limite di Blasius, ovvero le onde di Tollmien-Schlichting o onde TS. La teoria della stabilità secondaria si occupa sempre della fase lineare ma analizza la stabilità dei disturbi tridimensionali dopo che le onde TS si sono già stabilite all'interno dello strato limite e hanno raggiunto un'ampiezza finita. Matematicamente, questa condizione corrisponde alla soluzione del seguente problema differenziale

$$\begin{cases} \frac{\partial \boldsymbol{u}}{\partial t} + (\boldsymbol{u}\cdot\nabla)\boldsymbol{u} - \frac{1}{Re}\nabla^2\boldsymbol{u} + \nabla p = 0, \\ \nabla\cdot\boldsymbol{u} = 0, \\ \boldsymbol{u}(x,y,0) = \boldsymbol{U_1}(x,y), \\ \boldsymbol{u}(x_1,y,t) = \boldsymbol{U_1}(x_1,y) + \bar{A}\boldsymbol{u_{TS}}(x_1,y,t), \\ \boldsymbol{u}(x,0,t) = (0,0), \\ u(x,\infty,t) = 1, \quad \frac{\partial v}{\partial y}\big|_{(x,\infty,t)} = 0, \\ \big(\frac{\partial \boldsymbol{u}}{\partial t} + \bar{\boldsymbol{C}}\cdot\nabla\boldsymbol{u}\big)\big|_{(x_2,y,t)} = 0, \end{cases} \tag{A.1}$$

in cui lo strato limite stazionario $\boldsymbol{U_1}$ viene forzato dall'onda TS ($\boldsymbol{u_{TS}}$) all'ingresso del dominio. Il campo di velocità normalizzato $\boldsymbol{u_{TS}}$, calcolato tramite la risoluzione delle equazioni di Orr-Sommerfeld [66], è una funzione periodica del tempo. Di conseguenza, la soluzione $\boldsymbol{U_2}$ del problema A.1, se è stabile, sarà anch'essa periodica con lo stesso periodo dell'onda di TS. Il problema agli autovalori associato alla stabilità secondaria, riportato nel seguito, si ricava a partire dalle equazioni di Navier-Stokes linearizzate attorno a $\boldsymbol{U_2}$, espandendo in serie di Fourier la soluzione $\boldsymbol{u}$ nella direzione omogenea z e nel tempo.

$$\begin{cases} \frac{\partial \hat{u}}{\partial t} + U_2\frac{\partial \hat{u}}{\partial x} + \hat{v}\frac{\partial U_2}{\partial y} + \frac{\partial \hat{p}}{\partial x} - \frac{1}{Re}(\hat{\nabla}^2\hat{u} - \beta^2\hat{u}) + \big[\hat{u}\frac{\partial U_2}{\partial x} + V_2\frac{\partial \hat{u}}{\partial y}\big] = 0, \\ \frac{\partial \hat{v}}{\partial t} + U_2\frac{\partial \hat{v}}{\partial x} + \frac{\partial \hat{p}}{\partial y} - \frac{1}{Re}(\hat{\nabla}^2\hat{v} - \beta^2\hat{v}) + \big[\hat{u}\frac{\partial V_2}{\partial x} + V_2\frac{\partial \hat{v}}{\partial y} + \hat{v}\frac{\partial V_2}{\partial y}\big] = 0, \\ \frac{\partial \hat{w}}{\partial t} + U_2\frac{\partial \hat{w}}{\partial x} + \beta\hat{p} - \frac{1}{Re}(\hat{\nabla}^2\hat{w} - \beta^2\hat{w}) + \big[V_2\frac{\partial \hat{w}}{\partial y}\big] = 0, \\ \frac{\partial \hat{u}}{\partial x} + \frac{\partial \hat{v}}{\partial y} - \beta\hat{w} = 0, \\ \hat{\boldsymbol{u}}(x_1,y,z,t) = (0,0,0), \\ \hat{\boldsymbol{u}}(x,0,z,t) = (0,0,0), \\ \hat{\boldsymbol{u}}(x,\infty,z,t) = (0,0,0), \\ \big(\frac{\partial \hat{\boldsymbol{u}}}{\partial t} + \bar{\boldsymbol{C}}\cdot\nabla\hat{\boldsymbol{u}}\big)\big|_{(x_2,y,z,t)} = 0. \end{cases} \tag{A.2}$$

Le equazioni A.2 rappresentano un sistema di equazioni differenziali alle derivate parziali i cui coefficienti, le componenti o le derivate del flusso base $\boldsymbol{U_2}$, sono periodici nel tempo. La teoria di Fluquet [58] può essere quindi applicata al sistema A.2 e stabilisce che le sue autosoluzioni, in generale complesse, saranno anch'esse periodiche e con lo stesso periodo dell'onda di TS. Inoltre, queste ultime corrispondono alle autofunzioni dell'operatore di monodromia associato al sistema A.2 e, i corrispondenti autovalori chiamati moltiplicatori di Floquet, rappresentano il tasso di amplificazione dei disturbi ad ogni periodo temporale. La soluzione numerica del problema della stabilità secondaria può essere ottenuta tramite il metodo di Arnoldi [3]. Esso richiede di calcolare ad ogni iterazione l'azione dell'operatore di monodromia su un vettore generico, cioè di integrare le equazioni A.2 nel tempo per un periodo temporale dell'onda primaria. Lo schema numerico scelto in questo lavoro per integrare le equazioni di Navier-Stokes è lo stesso proposto in [12], la corrispondente formulazione discreta delle equazioni di Navier-Stokes è riportata nel sistema A.3.

$$\begin{cases} \frac{\boldsymbol{u}^{n+1}-\boldsymbol{u}^{n}}{\Delta t} - \frac{1}{2Re}\nabla^2\left(\boldsymbol{u}^{n+1}+\boldsymbol{u}^{n}\right) = \boldsymbol{f}^{n+1/2} - \nabla p^{*,n+1/2} - \boldsymbol{nl}(\boldsymbol{u}^{*,n+1/2}), \\ A\phi^{n+1/2} = -\frac{1}{\Delta t}\nabla\cdot\boldsymbol{u}^{n+1}, \\ p^{n+1/2} = p^{n-1/2} + \phi^{n+1/2} - \frac{\chi}{2Re}\nabla\cdot\left(\boldsymbol{u}^{n+1}+\boldsymbol{u}^{n}\right). \end{cases} \tag{A.3}$$

Lo schema numerico A.3 permette di disaccoppiare, ad ogni passo temporale, il calcolo del campo di velocità da quello di pressione (vedi [12]). Inoltre, grazie alla scelta dell'operatore differenziale A, definito

$$A := \left(1-\frac{\partial^2}{\partial x^2}\right)\left(1-\frac{\partial^2}{\partial y^2}\right)\left(1-\frac{\partial^2}{\partial z^2}\right), \tag{A.4}$$

l'integrazione delle equazioni nel tempo richiede solamente la soluzione di sistemi lineari tridiagonali (vedi [27] o [25] per maggiori informazioni).
L'analisi del meccanismo della stabilità secondaria, implica la risuluzione del problema agli autovalori A.2 nello spazio parametrico tridimensionale Re, β e $\bar{A}$. Nel seguito, si riporta lo spettro degli autovalori per il set di parametri $Re = 460$ e $\beta = 0.156$ al variare dell'ampiezza dell'onda primaria. Come si può osservare dalla figura A.1, all'aumentale di A il flusso di strato limite presenta un'instabilità sempre più marcata. Inoltre, è importante osservare come i modi più instabili siano reali, sincroni rispetto all'onda di T-S.

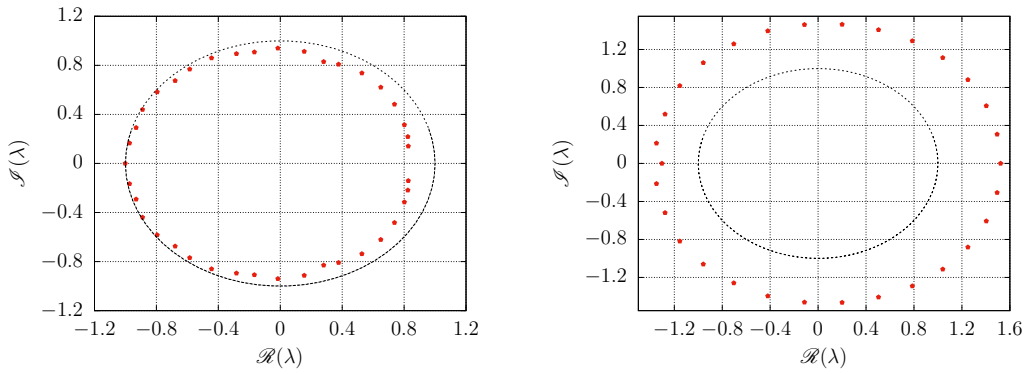

(a) $A = 0.5\%$ (b) $A = 1\%$

Figure A.1 *Spettro degli autovalori per $\beta = 0.156$ e $Re = 460$ al variare dell'ampiezza dell'onda primaria. La circonferenza tratteggiata delimità la regione di stabilità*

Il modo subarmonico, reale negativo, è il primo a diventare instabile e rimane nella parte più esterna dello spettro per valori bassi e medi di A (vedi A.1a). Per alte ampiezze, figura A.1b, è invece il modo fondamentale, reale positivo, ad essere il più instabile. Il comportamento qualitativo dello spettro esposto brevemente in questo contesto, è in perfetto accordo con la teoria di Herbert [31] e rispecchia le evidenze dei dati sperimentali [36]. La forma, simil circolare, tracciata dai moltiplicatori di Floquet è peculiare del fenomeno della stabilità secondaria. Poichè la fase dei moltiplicatori di Floquet è legata alla fequenza temporale dei disturbi, la forma dello spettro indica che l'instabilità coinvolge, per alte intesità A, il completo intervallo di frequenze da quella subarmonica a quella fondamentale con tassi di crescita dei modi tridimensionali comparabili tra loro. Le componenti di velocità u e v associate al modo subarmonico sono mostrate nella figura A.2.

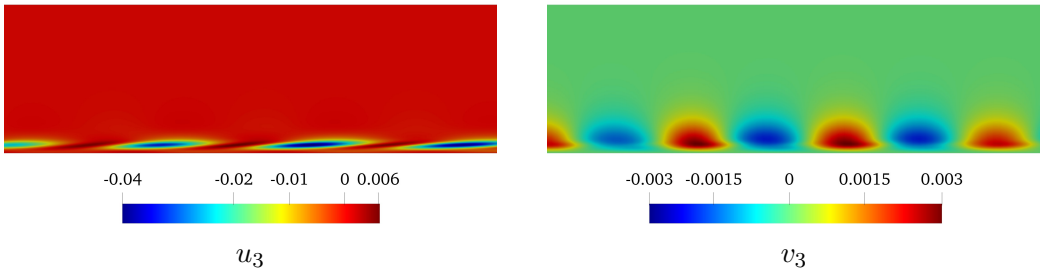

Figure A.2 *Componenti di velocità u e v associate al modo fondamentale.*

Per verificare se le strutture vicino alla parete, originate dal meccanismo di instabilità secondaria, portino effettivamente alla transizione, sono state eseguite delle simulazioni DNS tridimensionali. Il campo di velocità iniziale è costituito da un modo secondario sincrono sovrapposto al flusso base periodico. Il disturbo secondario è stato normalizzato opportunamente in modo che la sua ampiezza sia all'incirca lo 0.1% del flusso esterno. Le simulazioni non lineari mostrano che i disturbi introdotti nello strato limite sono in grado di provocare la transizione. Le strutture vorticose che si osservano appena prima della transizione, rispettivamente per il caso in cui è introdotto il modo fondamentale e quello subarmonico, sono riportate nelle figure A.3 e A.4.

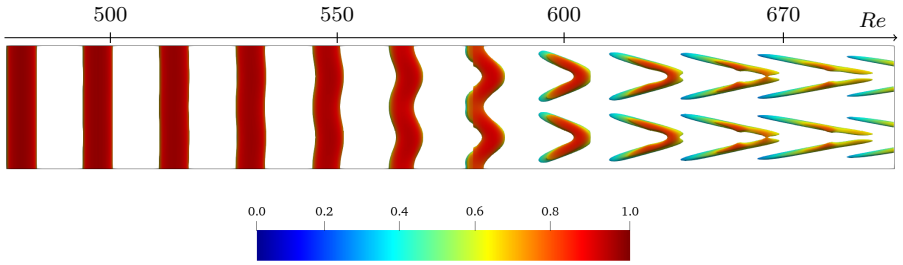

Figure A.3 *Isosuperfici per $t = 7.8T$ del secondo invariante del tensore gradiente di velocità, Q, colorate secondo la componente longitudinale della velocità. Notare la disposizione allineata dei vortici Λ.*

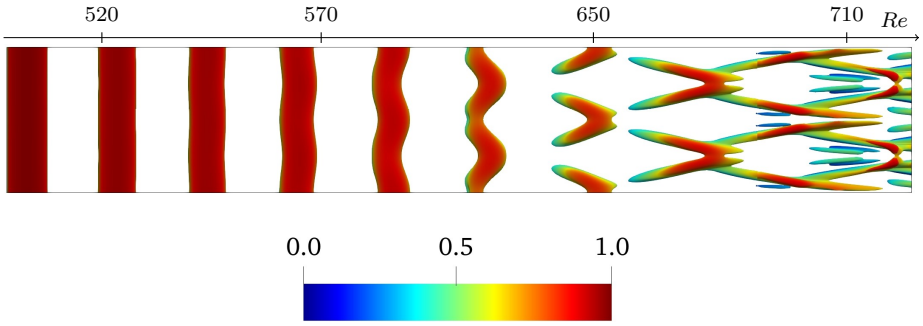

Figure A.4 *Isosuperfici per $t = 13T$ del secondo invariante del tensore gradiente di velocità, Q, colorate secondo la componente longitudinale della velocità.*

La tipica configurazione Λ dei vortici e la loro disposizione in file allineate oppure sfalsate, corrispondono alla transizione di tipo K (figura A.3) e H (figura A.4), due scenari ampiamente descritti nella letteratura [34]. Quindi, la

teoria della stabilità secondaria riesce a spiegare matematicamente lo sviluppo tridimensionale dello strato limite e fornisce la distribuzione di vorticità vicino alla parete che attiva il processo di transizione.

Bibliography

[1] E. Anderson, Z. Bai, C. Bischof, S. Blackford, J. D. J. Dongarra, J. D. Croz, A. Greenbaum, S. Hammarling, A. McKenney, and D. Sorensen. *LAPACK Users' Guide*. SIAM, 1999.

[2] G. R. G. Andrey V. Boiko, Alexander V. Dovgal. *Physics of Transitional Shear Flows*. Springer, 2012.

[3] W. E. Arnoldi. The principle of minimized iterations in the solution of the matrix eigenvalue problem. *Quarterly of Applied Mathematics*, 9(1):17–29, 1951.

[4] F. Auteri and L. Quartapelle. Galerkin-Laguerre Spectral Solution of Self-Similar Boundary Layer Problems. *Communications in Computational Physics*, 12:1329–1358, 2012.

[5] D. Barkley, H. M. Blackburn, and S. J. Sherwin. Direct optimal growth analysis for timesteppers. *International Journal for Numerical Methods in Fluids*, 57(9):1435–1458, 2008.

[6] B. J. Bayly, S. A. Orszag, and T. Herbert. Instability Mechanisms in Shear-Flow Transition. *Annual Review of Fluid Mechanics*, 20(1):359–391, 1988.

[7] S. Berlin, M. Wiegel, and D. S. Henningson. Numerical and experimental investigations of oblique boundary layer transition. *Journal of Fluid Mechanics*, 393:23–57, 1999.

[8] H. Blasius. *Grenzschichten in Flussigkeiten mit kleiner Reibung*. Druck von B.G. Teubner, 1908.

[9] D. Boffi, F. Brezzi, and M. Fortin. *Mixed Finite Element Methods and Applications*. Springer, 2013.

[10] M. Braack and P. Mucha. Directional Do-Nothing Condition for the Navier-Stokes Equations. *Journal of Computational Mathematics*, 32:507–521, 2014.

[11] L. Brevdo. *Instabile Wellenpakete in der Blasius'schen Grenzschichtstromung*. PhD thesis, Braunschweig Inst. für Strömungsmechanik, 1993.

[12] A. Chiarini, M. Quadrio, and F. Auteri. A direction-splitting Navier–Stokes solver on co-located grids. *Journal of Computational Physics*, 2020.

[13] A. J. Chorin. Numerical Solution of the Navier-Stokes Equations. *Mathematics of Computation*, 22:745–762, 1968.

[14] V. Citro, F. Giannetti, P. Luchini, and F. Auteri. Global stability and sensitivity analysis of boundary-layer flows past a hemispherical roughness element. *Physics of Fluids*, 27:084110, 2015.

[15] A. D. D. Craik. Non-linear resonant instability in boundary layers. *Journal of Fluid Mechanics*, 50:393–413, 1971.

[16] B. N. Datta. *Numerical Linear Algebra and Applications, Second Edition*. Society for Industrial and Applied Mathematics, 2010.

[17] M. O. Deville, P. F. Fischer, and E. H. Mund. *High-Order Methods for Incompressible Fluid Flow*. Cambridge University Press, 2002.

[18] J. Douglas. Alternating direction methods for three space variables. *Numerische Mathematik*, 4:41–63, 1962.

[19] J. R. Elston, J. Sheridan, and H. Blackburn. Two-dimensional Floquet stability analysis of the flow produced by an oscillating circular cylinder in quiescent fluid. *European Journal of Mechanics - B/Fluids*, 23(1):99–106, 2004.

[20] K. C. F. and R. P. J. A combined visual and hot-wire anemometer investigation of boundary-layer transition. *AIAA Journal*, 6(1):29–36, 1968.

[21] H. Fasel and U. Konzelmann. Non-parallel stability of a flat-plate boundary layer using the complete Navier-Stokes equations. *Journal of Fluid Mechanics*, 221:311–347, 1990.

[22] M. Gaster. On the effects of boundary-layer growth on flow stability. *Journal of Fluid Mechanics*, 66(3):465–480, 1974.

[23] F. Giannetti and P. Lucchini. Structural sensitivity of the first instability of the cylinder wake. *Journal of Fluid Mechanics*, 581:167–197, 2007.

[24] P. M. Gresho. Incompressible Fluid Dynamics: Some Fundamental Formulation Issues. *Annual Review of Fluid Mechanics*, 23:413–453, 1991.

[25] J. Guermond and P. Minev. A new class of massively parallel direction splitting for the incompressible Navier–Stokes equations. *Computer Methods in Applied Mechanics and Engineering*, 200(23):2083–2093, 2011.

[26] J. Guermond, P. Minev, and J. Shen. An overview of projection methods for incompressible flows. *Computer Methods in Applied Mechanics and Engineering*, 195(44):6011–6045, 2006.

[27] J.-L. Guermond and P. D. Minev. A new class of fractional step techniques for the incompressible Navier–Stokes equations using direction splitting, 2010.

[28] J.-L. Guermond and J. Shen. Velocity-Correction Projection Methods for Incompressible Flows. *SIAM J. Numerical Analysis*, 41:112–134, 2003.

[29] B.-Y. Guo and J. Shen. Laguerre-Galerkin method for nonlinear partial differential on a semi-infinite interval. *Numerische Mathematik*, pages 635–654, 2000.

[30] T. Herbert. Analysis of the subharmonic route to transition in boundary layers. In *22nd Aerospace Sciences Meeting*, 1984.

[31] T. Herbert. Secondary instability of boundary layers. *Annual Review of Fluid Mechanics*, 20:487–526, 1988.

[32] K. V. . L. V. Kachanov, Y.S. Nonlinear development of a wave in a boundary layer. *Fluid Dyn*, 12:383–390, 1977.

[33] Y. Kachanov and V. Y. Levchenko. The resonant interaction of disturbances at laminar-turbulent transition in a boundary layer. *Journal of Fluid Mechanics*, 138:209–247, 1984.

[34] Y. S. Kachanov. Physical Mechanisms of Laminar-Boundary-Layer Transition. *Annu. Rev. Fluid Mech.*, 26:411–482, 2003.

[35] C. T. Kelley. *Solving Nonlinear Equations with Newton's Method*. Society for Industrial and Applied Mathematics, 2003.

[36] P. S. Klebanoff, K. D. Tidstrom, and L. M. Sargent. The three-dimensional nature of boundary-layer instability. *Journal of Fluid Mechanics*, 12:1–34, 1962.

[37] M. Kloker, H. Fasel, and U. Konzelmann. Outflow boundary conditions for spatial Navier-Stokes simulations of transition boundary layers. *AIAA Journal*, 31:620–628, 1993.

[38] S. Kocak and H. Akay. Parallel Schur complement method for large-scale systems on distributed memory computers. *Applied Mathematical Modelling*, 25(10):873 – 886, 2001.

[39] R. B. Lehoucq and D. C. Sorensen. Deflation Techniques for an Implicitly Restarted Arnoldi Iteration. *SIAM Journal on Matrix Analysis and Applications*, 17(4):789–821, 1996.

[40] R. B. Lehoucq, D. C. Sorensen, and C. Yang. ARPACK Users Guide: Solution of Large Scale Eigenvalue Problems by Implicitly Restarted Arnoldi Methods., 1997.

[41] Y. Li, J.-I. Choi, Y. Choic, and J. Kim. A simple and efficient outflow boundary condition for the incompressible Navier–Stokes equations. *Engineering Applications of Computational Fluid Mechanics*, 11(1):69–85, 2017.

[42] J. Liu. Open and traction boundary conditions for the incompressible Navier–Stokes equations. *Journal of Computational Physics*, 228(19):7250–7267, 2009.

[43] Y. Liu, T. A. Zaki, and P. A. Durbin. Floquet analysis of secondary instability of boundary layers distorted by Klebanoff streaks and Tollmien–Schlichting waves. *Physics of Fluids*, 20(12), 2008.

[44] W. Z.-q. Liu Fu-jun, Li Hui-yuan. Spectral methods using generalized Laguerre functions for second and fourth order problems. *Numerical Algorithms*, 75:1005–1040, 2017.

[45] L. M. Mack. A numerical study of the temporal eigenvalue spectrum of the Blasius boundary layer. *Journal of Fluid Mechanics*, 73(3):497–520, 1976.

[46] E. R. Mark V. Morkovin. Dialogue on progress and issues in stability and transition research. In *Laminar-Turbulent Transition*, pages 3–29, 1990.

[47] L. Maseev. Occurrence of three-dimensional perturbations in a boundary layer. *Fluid Dyn* , 3:23–24, 1968.

[48] M. V. Morkovin. On the many faces of transition. In *Viscous Drag Reduction*, pages 1–31, 1969.

[49] A. Nayfeh and J. Masad. Recent advances in secondary instabilities in boundary layers. *Computing Systems in Engineering*, 1(2):401–414, 1990.

[50] I. Orlanski. A simple boundary condition for unbounded hyperbolic flows. *Journal of Computational Physics*, 21(3):251–269, 1976.

[51] W. Orr. The Stability or Instability of the Steady Motions of a Perfect Liquid and of a Viscous Liquid. Part II: A Viscous Liquid. *Proceedings of the Royal Irish Academy. Section A: Mathematical and Physical Sciences*, 27:69–138, 1907.

[52] I. Panardo. Stability of periodic systems and Floquet Theory, 2014.

[53] K. Parand, M. Shahini, and M. Dehghan. Solution of a laminar boundary layer flow via a numerical method. *Communications in Nonlinear Science and Numerical Simulation*, 15(2):360–367, 2010.

[54] K. Parand and A. Taghavi. Rational scaled generalized Laguerre function collocation method for solving the Blasius equation. *Journal of Computational and Applied Mathematics*, 233(4):980–989, 2009.

[55] D. S. H. Peter J. Schmid. *Stability and Transition in Shear Flows*. Springer, 2012.

[56] Ren, Jie and Fu, Song. Floquet analysis of fundamental, subharmonic and detuned secondary instabilities of Görtler vortices. *Science China: Physics, Mechanics and Astronomy*, 57:555–561, 03 2014.

[57] O. Reynolds. On the dynamic theory of incompressible viscous fluids and the determination of the criterion. *Philosophical Transactions of the Royal Society of London*, 186:123–164, 1894.

[58] J. Richards. *Analysis of Periodically Time-varying Systems*. Springer, 1983.

[59] U. Rist, M. Kai, and S. Wagner. Visualisation of late-stage transitional structures in numerical data using vortex identification and feature extraction. 1999.

[60] J. A. Ross, F. H. Barnes, J. G. Burns, and M. A. S. Ross. The flat plate boundary layer. Part 3. Comparison of theory with experiment. *Journal of Fluid Mechanics*, 43(4):819–832, 1970.

[61] W. S. Saric and A. S. W. Thomas. Experiments on the subharmonic route to turbulence in boundary layers. In *Turbulence and Chaotic Phenomena in Fluids*, pages 117–122, 1984.

[62] T. Sayadi, C. Hamman, and P. Moin. Direct numerical simulation of complete H-type and K-type transitions with implications for the dynamics of turbulent boundary layers. *Journal of Fluid Mechanics*, 724:480–509, 2013.

[63] M. Schäfer. *Computational Engineering — Introduction to Numerical Methods*. Springer, 2006.

[64] H. Schlichting. *Zur Entstehung der Turbulenz bei der Plattenstromung*. Weidmann, 1933.

[65] H. Schlichting. *Amplitudenverteilung und Energiebilanz der kleinen Storungen bei der Plattenstromung*. Weidmann, 1935.

[66] H. Schlichting and K. Gersten. *Boundary-Layer Theory*. Springer, 2000.

[67] G. B. Schubauer and H. K. Skramstad. Laminar Boundary-Layer Oscillations and Stability of Laminar Flow. *Journal of the Aeronautical Sciences* , 14:2:69–79, 1947.

[68] J. Shen. Stable and Efficient Spectral Methods in Unbounded Domains Using Laguerre Functions. *SIAM Journal on Numerical Analysis*, 38(4):1113–1133, 2000.

[69] J. Shen and L.-L. Wang. Some Recent Advances on Spectral Methods for Unbounded Domains. *Communications in Computational Physics*, 5:195–241, 2009.

[70] A. Sommerfeld. *Ein Beitrag zur hydrodynamischen Erklarung der turbulenten Flussigkeitsbewegungen*. Accademia dei Lincei, 1908.

[71] P. R. Spalart and K.-S. Yang. Numerical study of ribbon-induced transition in Blasius flow. *Journal of Fluid Mechanics*, 178:345–365, 1987.

[72] R. Témam. Sur l'approximation de la solution des équations de Navier-Stokes par la méthode des pas fractionnaires (I). *Archive for Rational Mechanics and Analysis*, 32(2):135–153, 1969.

[73] S. W. S. Thomas, A. S. W. Harmonic and subharmonic waves during boundary-layer transition. *Bull. Am. Phys. Soc.* , 26:12–52, 1981.

[74] L. J. P. Timmermans, P. D. Minev, and F. N. Van De Vosse. An approximate projection scheme for incompressible flow using spectral elements. *International Journal for Numerical Methods in Fluids*, 22(7):673–688, 1996.

[75] W. Tollmien. Uber die Entstehung der Turbulenz. *Nachrichten von der Gesellschaft der Wissenschaften zu Gottingen*, 1929:21–44, 1931.

[76] L. N. Trefethen and D. Bau. *Numerical Linear Algebra*. SIAM, 1997.

[77] R. D. J. W. O. Criminale, T. L. Jackson. *Theory and computation of hydrodynamic stability*. Cambridge University Press, 2003.

[78] Z. G. Wang Dongyao. On secondary instability with respect to three dimensional subharmonics disturbances in boundary layers. *Acta Mechanica Sinica*, 8(3):231–236, 1992.

[79] Z. Yang. Lattice Boltzmann outflow treatments: Convective conditions and others. *Computers & Mathematics with Applications*, 65(2):160 – 171, 2013.

[80] T. A. Zang. On the rotation and skew-symmetric forms for incompressible flow simulations. *Applied Numerical Mathematics*, 7:27 – 40, 1991.

[81] Y. Zang, R. L. Street, and J. R. Koseff. A Non-Staggered Grid, Fractional Step Method for Time-Dependent Incompressible Navier-Stokes Equations in Curvilinear Coordinates. *J. Comput. Phys.*, 114(1):18–33, 1994.

[82] F. Zhang. *The Schur Complement and its Applications*. Springer, 2005.

[83] Y. Zhao, C. Lei, and J. C. Patterson. The K-type and H-type transitions of natural convection boundary layers. *Journal of Fluid Mechanics*, 824:352–387, 2017.